

広島大学学位請求論文

First measurement of ω and ϕ mesons
via di-electron decay channels

in proton+proton collisions at $\sqrt{s} = 200$ GeV

(重心系衝突エネルギー 200GeV の陽子 + 陽子衝突における
電子・陽電子崩壊過程を用いた ω 、 ϕ 中間子の最初の測定)

2012年1月

広島大学大学院理学研究科
物理学専攻

来島 孝太郎

目次

1. 主論文

First measurement of ω and ϕ mesons via di-electron decay channels
in proton+proton collisions at $\sqrt{s} = 200$ GeV
(重心系衝突エネルギー 200GeV の陽子 + 陽子衝突における電子・陽電子崩壊
過程を用いた ω 、 ϕ 中間子の最初の測定)
来島 孝太郎

2. 公表論文

- (1) Measurement of neutral mesons in $p+p$ collisions at $\sqrt{s} = 200$ GeV and
scaling properties of hadron production
A.Adare, K.M.Kijima *et al.*, (別紙、共著者リスト 1 参照)
Physical Review C83, 052004 (2011).

3. 参考論文

- (1) Nuclear modification factors of ϕ mesons in $d+Au$, $Cu+Cu$ and
 $Au+Au$ collisions at $\sqrt{s_{NN}} = 200$ GeV
A.Adare, K.M.Kijima *et al.*, (別紙、共著者リスト 2 参照)
Physical Review C83, 024909 (2011).
- (2) Identified charged hadron production in $p+p$ collisions at $\sqrt{s} = 200$
and 62.4GeV
A.Adare, K.M.Kijima *et al.*, (別紙、共著者リスト 3 参照)
Physical Review C83, 064903 (2011).

共著者リスト 1

A.Adare, S.Afanasyev, C.Aidala, N.N.Ajitanand, Y.Akiba, H.Al-Bataineh, J.Alexander, K.Aoki, L.Aphecetche, R.Armendariz, S.H.Aronson, J.Asai, E.T.Atomssa, R.Averbeck, T.C.Awes, B.Azmoun, V.Babintsev, M.Bai, G.Baksay, L.Baksay, A.Baldisseri, K.N.Barish, P.D.Barnes, B.Bassalleck, A.T.Basye, S.Bathe, S.Batsouli, V.Baublis, C.Baumann, A.Bazilevsky, S.Belikov, R.Bennett, A.Berdnikov, Y.Berdnikov, A.A.Bickley, J.G.Boissevain, H.Borel, K.Boyle, M.L.Brooks, H.Buesching, V.Bumazhnov, G.Bunce, S.Buttsyk, C.M.Camacho, S.Campbell, B.S.Chang, W.C.Chang, J.-L.Charvet, S.Chernichenko, J.Chiba, C.Y.Chi, M.Chiu, I.J.Choi, R.K.Choudhury, T.Chujo, P.Chung, A.Churn, V.Cianciolo, Z.Citron, C.R.Cleven, B.A.Cole, M.P.Comets, P.Constantin, M.Csanad, T.Csorgo, T.Dahms, S.Dairaku, K.Das, G.David, M.B.Deaton, K.Dehmelt, H.Delagrange, A.Denisov, D.d'Enterria, A.Deshpande, E.J.Desmond, O.Dietzsch, A.Dion, M.Donadelli, O.Drapier, A.Drees, K.A.Drees, A.K.Dubey, A.Durum, D.Dutta, V.Dzhordzhadze, Y.V.Efremenko, J.Egdemir, F.Ellinghaus, W.S.Emam, T.Engelmore, A.Enokizono, H.En'yo, S.Esumi, K.O.Eyser, B.Fadem, D.E.Fields, M.Finger, Jr., M.Finger, F.Fleuret, S.L.Fokin, Z.Fraenkel, J.E.Frantz, A.Franz, A.D.Frawley, K.Fujiwara, Y.Fukao, T.Fusayasu, S.Gadrat, I.Garishvili, A.Glenn, H.Gong, M.Gonin, J.Gosset, Y.Goto, R.Granie.d.Cassagnac, N.Grau, S.V.Greene, M.Gross.Perdekamp, T.Gunji, H.-A.Gustafsson, T.Hachiya, A.Had.Henni, C.Haegemann, J.S.Haggerty, H.Hamagaki, R.Han, H.Harada, E.P.Hartouni, K.Haruna, E.Haslum, R.Hayano, M.Heffner, T.K.Hemmick, T.Hester, X.He, H.Hiejima, J.C.Hill, R.Hobbs, M.Hohlmann, W.Holzmann, K.Homma, B.Hong, T.Horaguchi, D.Hornback, S.Huang, T.Ichihara, R.Ichimiya, H.Iinuma, Y.Ikeda, K.Imai, J.Imrek, M.Inaba, Y.Inoue, D.Isenhower, L.Isenhower, M.Ishihara, T.Isobe, M.Issah, A.Isupov, D.Ivanishev, B.V.Jacak, J.Jia, J.Jin, O.Jinnouchi, B.M.Johnson, K.S.Joo, D.Jouan, F.Kajihara, S.Kametani, N.Kamihara, J.Kamin, M.Kaneta, J.H.Kang, H.Kanou, J.Kapustinsky, D.Kawall, A.V.Kazantsev, T.Kempel, A.Khanzadeev, K.M.Kijima, J.Kikuchi, B.I.Kim, D.H.Kim, D.J.Kim, E.Kim, S.H.Kim, E.Kinney, K.Kiriluk, A.Kiss, E.Kistenev, A.Kiyomichi, J.Klay, C.Klein-Boesing, L.Kochenda, V.Kochetkov, B.Komkov, M.Konno, J.Koster, D.Kotchetkov, A.Kozlov, A.Kral, A.Kravitz, J.Kubart, G.J.Kunde, N.Kurihara, K.Kurita, M.Kurosawa, M.J.Kweon, Y.Kwon, G.S.Kyle, R.Lacey, Y.S.Lai, J.G.Lajoie, D.Layton, A.Lebedev, D.M.Lee, K.B.Lee, M.K.Lee, T.Lee, M.J.Leitch, M.A.L.Leite, B.Lenzi, P.Liebing, T.Liska, A.Litvinenko, H.Liu, M.X.Liu, X.Li, B.Love, D.Lynch, C.F.Maguire, Y.I.Makdisi, A.Malakhov, M.D.Malik, V.I.Manko, E.Mannel, Y.Mao, L.Masek, H.Masui, F.Matathias, M.McCumber, P.L.McGaughey, N.Means, B.Meredith, Y.Miake, P.Mikes, K.Miki, T.E.Miller, A.Milov, S.Mioduszewski, M.Mishra, J.T.Mitchell, M.Mitrovski, A.K.Mohanty, Y.Morino, A.Morreale, D.P.Morrison, T.V.Moukhanova, D.Mukhopadhyay, J.Murata, S.Nagamiya, Y.Nagata, J.L.Nagle, M.Naglis, M.I.Nagy, I.Nakagawa, Y.Nakamiya, T.Nakamura, K.Nakano, J.Newby, M.Nguyen, T.Niita, B.E.Norman, R.Nouicer, A.S.Nyanin, E.O'Brien, S.X.Oda, C.A.Ogilvie, H.Ohnishi, K.Okada, M.Oka, O.O.Omiwade, Y.Onuki, A.Oskarsson, M.Ouchida, K.Ozawa, R.Pak, D.Pal, A.P.T.Palounek, V.Pantuev, V.Papavassiliou, J.Park, W.J.Park, S.F.Pate, H.Pei, J.-C.Peng, H.Pereira, V.Peresedov, D.Yu.Peressouko, C.Pinkenburg, M.L.Purschke, A.K.Purwar, H.Qu, J.Rak, A.Rakotozafindrabe, I.Ravinovich, K.F.Read, S.Rembeczki, M.Reuter, K.Reygers, V.Riabov, Y.Riabov, D.Roach, G.Roche, S.D.Rolnick, A.Romana, M.Rosati, S.S.E.Rosendahl, P.Rosnet, P.Rukoyatkin, P.Ruzicka, V.L.Rykov, B.Sahlmuller, N.Saito, T.Sakaguchi, S.Sakai, K.Sakashita, H.Sakata, V.Samsonov, S.Sato, T.Sato, S.Sawada, K.Sedgwick, J.Seele, R.Seidl, A.Yu.Semenov, V.Semenov, R.Seto, D.Sharma, I.Shein, A.Shevel, T.-A.Shibata, K.Shigaki, M.Shimomura, K.Shoji, P.Shukla, A.Sickles, C.L.Silva, D.Silvermyr, C.Silvestre, K.S.Sim, B.K.Singh, C.P.Singh, V.Singh, S.Skutnik, M.Slunecka, A.Soldatov, R.A.Soltz, W.E.Sondheim, S.P.Sorensen, I.V.Sourikova, F.Staley, P.W.Stankus, E.Stenlund, M.Stepanov, A.Ster, S.P.Stoll, T.Sugitate, C.Suire, A.Sukhanov, J.Sziklai, T.Tabaru, S.Takagi, E.M.Takagui, A.Taketani, R.Tanabe, Y.Tanaka, K.Tanida, M.J.Tannenbaum, A.Taranenko, P.Tarjan, H.Themann, T.L.Thomas, M.Togawa, A.Toia, J.Tojo, L.Tomasek, Y.Tomita, H.Torii, R.S.Towell, V.-N.Tram, I.Tserruya, Y.Tsuchimoto, C.Vale, H.Valle, H.W.va.Hecke, A.Veicht, J.Velkovska, R.Vertesi, A.A.Vinogradov, M.Virius, V.Vrba, E.Vznuzdaev, M.Wagner, D.Walker, X.R.Wang, Y.Watanabe, F.Wei, J.Wessels, S.N.White, D.Winter, C.L.Woody, M.Wysocki, W.Xie, Y.L.Yamaguchi, K.Yamaura, R.Yang, A.Yanovich, Z.Yasin, J.Ying, S.Yokkaichi, G.R.Young, I.Younus, I.E.Yushmanov, W.A.Zajc, O.Zaudtke, C.Zhang, S.Zhou, J.Zimanyi, L.Zolin

共著者リスト 2

A.Adare, S.Afanasiev, C.Aidala, N.N.Ajitanand, Y.Akiba, H.Al-Bataineh, J.Alexander, A.Al-Jamel, A.Angerami, K.Aoki, N.Apadula, L.Aphecetche, Y.Aramaki, R.Armendariz, S.H.Aronson, J.Asai, E.T.Atomssa, R.Averbeck, T.C.Awes, B.Azmoun, V.Babintsev, M.Bai, G.Baksay, L.Baksay, A.Baldisseri, K.N.Barish, P.D.Barnes, B.Bassalleck, A.T.Basye, S.Bathe, S.Batsouli, V.Baublis, F.Bauer, C.Baumann, A.Bazilevsky, S.Belikov, R.Belmont, R.Bennett, A.Berdnikov, Y.Berdnikov, J.H.Bhom, A.A.Bickley, M.T.Bjorndal, D.S.Blau, J.G.Boissevain, J.S.Bok, H.Borel, N.Borggren, K.Boyle, M.L.Brooks, D.S.Brown, D.Bucher, H.Buesching, V.Bumazhnov, G.Bunce, J.M.Burward-Hoy, S.Buttsyk, S.Campbell, A.Caringi, J.-S.Chai, B.S.Chang, J.L.Charvet, C.H.Chen, S.Chernichenko, J.Chiba, C.Y.Chi, M.Chiu, I.J.Choi, J.B.Choi, R.K.Choudhury, P.Christiansen, T.Chujo, P.Chung, A.Churn, O.Chvala, V.Cianciolo, Z.Citron, C.R.Cleven, Y.Cobigo, B.A.Cole, M.P.Comets, Z.Cones.de.Valle, M.Connors, P.Constantin, M.Csanad, T.Csorgo, T.Dahms, S.Dairaku, I.Danchev, K.Das, A.Datta, G.David, M.K.Dayananda, M.B.Deaton, K.Dehmelt, H.Delagrange, A.Denisov, D.d'Enterria, A.Deshpande, E.J.Desmond, K.V.Dharmawardane, O.Dietzsch, A.Dion, M.Donadelli, L.D'Orazio, J.L.Drachenberg, O.Drapier, A.Drees, K.A.Drees, A.K.Dubey, J.M.Durham, A.Durum, D.Dutta, V.Dzhordzhadze, S.Edwards, Y.V.Efremenko, J.Egdemir, F.Ellinghaus, W.S.Emam, T.Engelmore, A.Enokizono, H.En'yo, B.Espagnon, S.Esumi, K.O.Eyser, B.Fadem, D.E.Fields, M.Finge.Jr., M.Finger, F.Fleuret, S.L.Fokin, B.Forestier, Z.Fraenkel, J.E.Frantz, A.Franz, A.D.Frawley, K.Fujiwara, Y.Fukao, S.Y.Fung, T.Fusayasu, S.Gadrat, I.Garishvili, F.Gastineau, M.Germain, A.Glenn, H.Gong, M.Gonin, J.Gosset, Y.Goto, R.Granier.de.Cassagnac, N.Grau, S.V.Greene, G.Grim, M.Gross.Perdekamp, T.Gunji, H.-A.Gustafsson, T.Hachiya, A.Had.Henni, C.Haegemann, J.S.Haggerty, M.N.Hagiwara, K.I.Hahn, H.Hamagaki, J.Hamblen, J.Hanks, R.Han, H.Harada, E.P.Hartouni, K.Haruna, M.Harvey, E.Haslum, K.Hasuko, R.Hayano, M.Heffner, T.K.Hemmick, T.Hester, J.M.Heuser, X.He, H.Hiejima, J.C.Hill, R.Hobbs, M.Hohlmann, M.Holmes, W.Holzmann, K.Homma, B.Hong, T.Horaguchi, D.Hornback, S.Huang, M.G.Hur, T.Ichihara, R.Ichimiya, H.Iinuma, Y.Ikeda, K.Imai, M.Inaba, Y.Inoue, D.Isenhower, L.Isenhower, M.Ishihara, T.Isobe, M.Issah, A.Isupov, D.Ivanischev, Y.Iwanaga, B.V.Jacak, J.Jia, X.Jiang, J.Jin, O.Jinnouchi, B.M.Johnson, T.Jones, K.S.Joo, D.Jouan, D.S.Jumper, F.Kajihara, S.Kametani, N.Kamihara, J.Kamin, M.Kaneta, J.H.Kang, H.Kanou, J.Kapustinsky, K.Karatsu, M.Kasai, T.Kawagishi, D.Kawall, M.Kawashima, A.V.Kazantsev, S.Kelly, T.Kempel, A.Khanzadeev, K.M.Kijima, J.Kikuchi, A.Kim, B.I.Kim, D.H.Kim, D.J.Kim, E.J.Kim, E.Kim, Y.-J.Kim, Y.-S.Kim, E.Kinney, A.Kiss, E.Kistenev, A.Kiyomichi, J.Klay, C.Klein-Boesing, L.Kochenda, V.Kochetkov, B.Komkov, M.Konno, J.Koster, D.Kotchetkov, D.Kotov, A.Kozlov, A.Kral, A.Kravitz, P.J.Kroon, J.Kubart, G.J.Kunde, N.Kurihara, K.Kurita, M.Kurosawa, M.J.Kweon, Y.Kwon, G.S.Kyle, R.Lacey, Y.S.Lai, J.G.Lajoie, A.Lebedev, Y.L.Bornec, S.Leckey, D.M.Lee, J.Lee, K.B.Lee, K.S.Lee, M.K.Lee, T.Lee, M.J.Leitch, M.A.L.Leite, B.Lenzi, P.Lichtenwalner, P.Liebing, H.Lim, L.A.Linde.Levy, T.Liska, A.Litvinenko, H.Liu, M.X.Liu, X.Li, X.H.Li, B.Love, D.Lynch, C.F.Maguire, Y.I.Makdisi, A.Malakhov, M.D.Malik, V.I.Manko, E.Mannel, Y.Mao, L.Masek, H.Masui, F.Matathias, M.C.McCain, M.McCumber, P.L.McGaughey, N.Means, B.Meredith, Y.Miake, T.Mibe, A.C.Mignerey, P.Mikes, K.Miki, T.E.Miller, A.Milov, S.Mioduszewski, G.C.Mishra, M.Mishra, J.T.Mitchell, M.Mitrovski, A.K.Mohanty, H.J.Moon, Y.Morino, A.Morreale, D.P.Morrison, J.M.Moss, T.V.Moukhanova, D.Mukhopadhyay, T.Murakami, J.Murata, S.Nagamiya, Y.Nagata, J.L.Nagle, M.Naglis, M.I.Nagy, I.Nakagawa, Y.Nakamiya, K.R.Nakamura, T.Nakamura, K.Nakano, S.Nam, J.Newby, M.Nguyen, M.Nihashi, B.E.Norman, R.Nouicer, A.S.Nyanin, J.Nystrand, C.Oakley, E.O'Brien, S.X.Oda, C.A.Ogilvie, H.Ohnishi, I.D.Ojha, K.Okada, M.Oka, O.O.Omiwade, Y.Onuki, A.Oskarsson, I.Otterlund, M.Ouchida, K.Ozawa, R.Pak, D.Pal, A.P.T.Palounek, V.Pantuev, V.Papavassiliou, I.H.Park, J.Park, S.K.Park, W.J.Park, S.F.Pate, H.Pei, J.-C.Peng, H.Pereira, V.Peresedov, D.Yu.Peressouko, R.Petti, C.Pinkenburg, R.P.Pisani, M.Proissl, M.L.Purschke, A.K.Purwar, H.Qu, J.Rak, A.Rakotozafindrabe, I.Ravinovich, K.F.Read, S.Rembeczki, M.Reuter, K.Reygers, V.Riabov, Y.Riabov, E.Richardson, D.Roach, G.Roche, S.D.Rolnick, A.Romana, M.Rosati, C.A.Rosen, S.S.E.Rosendahl, P.Rosnet, P.Rukoyatkin, P.Ruzicka, V.L.Rykov, S.S.Ryu, B.Sahmueller, N.Saito, T.Sakaguchi, S.Sakai, K.Sakashita, H.Sakata, V.Samsonov, S.Sano, H.D.Sato, S.Sato, T.Sato, S.Sawada, K.Sedgwick, J.Seele, R.Seidl, V.Semenov, R.Seto, D.Sharma, T.K.Shea, I.Shein, A.Shevel, T.-A.Shibata, K.Shigaki, M.Shimomura, T.Shohjoh, K.Shoji, P.Shukla,

A.Sickles, C.L.Silva, D.Silvermyr, C.Silvestre, K.S.Sim, B.K.Singh, C.P.Singh, V.Singh, S.Skutnik, M.Slunecka, W.C.Smith, A.Soldatov, R.A.Soltz, W.E.Sondheim, S.P.Sorensen, I.V.Sourikova, F.Staley, P.W.Stankus, E.Stenlund, M.Stepanov, A.Ster, S.P.Stoll, T.Sugitate, C.Suire, A.Sukhanov, J.P.Sullivan, J.Sziklai, T.Tabaru, S.Takagi, E.M.Takagui, A.Taketani, R.Tanabe, K.H.Tanaka, Y.Tanaka, S.Taneja, K.Tanida, M.J.Tannenbaum, S.Tarafdar, A.Taranenko, P.Tarjan, H.Themann, D.Thomas, T.L.Thomas, M.Togawa, A.Toia, J.Tojo, L.Tomasek, H.Torii, R.S.Towell, V.-N.Tram, I.Tserruya, Y.Tsuchimoto, S.K.Tuli, H.Tydesjo, N.Tyurin, C.Vale, H.Valle, H.W.va.Hecke, E.Vazquez-Zambrano, A.Veicht, J.Velkovska, R.Vertesi, A.A.Vinogradov, M.Virus, V.Vrba, E.Vznuzdaev, M.Wagner, D.Walker, X.R.Wang, D.Watanabe, K.Watanabe, Y.Watanabe, F.Weil, J.Wessels, S.N.White, N.Willis, D.Winter, C.L.Woody, R.M.Wright, M.Wysocki, W.Xie, Y.L.Yamaguchi, K.Yamaura, R.Yang, A.Yanovich, Z.Yasin, J.Ying, S.Yokkaichi, G.R.Young, I.Younus, Z.You, I.E.Yushmanov, W.A.Zajc, O.Zaudtke, C.Zhang, S.Zhou, J.Zimanyi, L.Zolin

共著者リスト 3

A.Adare, S.Afanasyev, C.Aidala, N.N.Ajitanand, Y.Akiba, H.Al-Bataineh, J.Alexander, K.Aoki, L.Aphecetche, R.Armendariz, S.H.Aronson, J.Asai, E.T.Atomssa, R.Averbeck, T.C.Awes, B.Azmoun, V.Babintsev, M.Bai, G.Baksay, L.Baksay, A.Baldisseri, K.N.Barish, P.D.Barnes, B.Bassalleck, A.T. Basye, S.Bathe, S.Batsouli, V.Baublis, C.Baumann, A.Bazilevsky, S.Belikov, R.Bennett, A.Berdnikov, Y.Berdnikov, A.A.Bickley, J.G.Boissevain, H.Borel, K.Boyle, M.L.Brooks, H.Buesching, V.Bumazhnov, G.Bunce, S.Buttsyk, C.M.Camacho, S.Campbell, B.S.Chang, W.C.Chang, J.-L.Charvet, S.Chernichenko, J.Chiba, C.Y.Chi, M.Chiu, I.J.Choi, R.K.Choudhury, T.Chujo, P.Chung, A.Churn, V.Cianciolo, Z.Citron, C.R.Cleven, B.A.Cole, M.P.Comets, P.Constantin, M.Csanad, T.Csorgo, T.Dahms, S.Dairaku, K.Das, G.David, M.B.Deaton, K.Dehmelt, H.Delagrange, A.Denisov, D.d'Enterria, A.Deshpande, E.J.Desmond, O.Dietzsch, A.Dion, M.Donadelli, O.Drapier, A.Drees, K.A.Drees, A.K.Dubey, A.Durum, D.Dutta, V.Dzhordzhadze, Y.V.Efremenko, J.Egdemir, F.Ellinghaus, W.S.Emam, T.Engelmore, A.Enokizono, H.En'yo, S.Esumi, K.O.Eyser, B.Fadem, D.E.Fields, M.Finge.Jr., M.Finger, F.Fleuret, S.L.Fokin, Z.Fraenkel, J.E.Frantz, A.Franz, A.D.Frawley, K.Fujiwara, Y.Fukao, T.Fusayasu, S.Gadrat, I.Garishvili, A.Glenn, H.Gong, M.Gonin, J.Gosset, Y.Goto, R.Granie.d.Cassagnac, N.Grau, S.V.Greene, M.Gross.Perdekamp, T.Gunji, H.-A.Gustafsson, T.Hachiya, A.Had.Henni, C.Haegemann, J.S.Haggerty, H.Hamagaki, R.Han, H.Harada, E.P. Hartouni, K.Haruna, E.Haslum, R.Hayano, M.Heffner, T.K.Hemmick, T.Hester, X.He, H.Hiejima, J.C. Hill, R.Hobbs, M.Hohlmann, W.Holzmann, K.Homma, B.Hong, T.Horaguchi, D.Hornback, S.Huang, T.Ichihara, R.Ichimiya, H.Iinuma, Y.Ikeda, K.Imai, J.Imrek, M.Inaba, Y.Inoue, D.Isenhowe, L.Isenhowe, M.Ishihara, T.Isobe, M.Issah, A.Isupov, D.Ivanishev, B.V.Jacak, J.Jia, J.Jin, O. Jinnouchi, B.M.Johnson, K.S.Joo, D.Jouan, F.Kajihara, S.Kametani, N.Kamihara, J.Kamin, M.Kaneta, J.H.Kang, H.Kanou, J.Kapustinsky, D.Kawall, A.V.Kazantsev, T.Kempel, A.Khanzadeev, K.M.Kijima, J.Kikuchi, B.I.Kim, D.H.Kim, D.J.Kim, E.Kim, S.H.Kim, E.Kinney, K.Kiriluk, A.Kiss, E.Kistenev, A.Kiyomichi, J.Klay, C.Klein-Boesing, L.Kochenda, V.Kochetkov, B.Komkov, M.Konno, J.Koster, D.Kotchetkov, A.Kozlov, A.Kral, A.Kravitz, J.Kubart, G.J.Kunde, N.Kurihara, K.Kurita, M.Kurosawa, M.J.Kweon, Y.Kwon, G.S.Kyle, R.Lacey, Y.S.Lai, J.G.Lajoie, D.Layton, A.Lebedev, D.M.Lee, K.B.Lee, M.K.Lee, T.Lee, M.J.Leitch, M.A.L.Leite, B.Lenzi, P.Liebing, T.Liska, A.Litvinenko, H.Liu, M.X.Liu, X.Li, B.Love, D.Lynch, C.F.Maguire, Y.I.Makdisi, A.Malakhov, M.D.Malik, V.I.Manko, E.Mannel, Y.Mao, L.Masek, H.Masui, F.Matathias, M.McCumber, P.L. McGaughey, N.Means, B.Meredith, Y.Miake, P.Mikes, K.Miki, T.E.Miller, A.Milov, S.Mioduszewski, M.Mishra, J.T.Mitchell, M.Mitrovski, A.K.Mohanty, Y.Morino, A.Morreale, D.P.Morrison, T.V.Moukhanova, D.Mukhopadhyay, J.Murata, S.Nagamiya, Y.Nagata, J.L.Nagle, M.Naglis, M.I.Nagy, I.Nakagawa, Y.Nakamiya, T.Nakamura, K.Nakano, J.Newby, M.Nguyen, T.Niita, B.E.Norman, R.Nouicer, A.S. Nyanin, E.O'Brien, S.X.Oda, C.A.Ogilvie, H.Ohnishi, K.Okada, M.Oka, O.O.Omiwade, Y.Onuki, A.Oskarsson, M.Ouchida, K.Ozawa, R.Pak, D.Pal, A.P.T.Palounek, V.Pantuev, V.Papavassiliou, J.Park, W.J.Park, S.F.Pate, H.Pei, J.-C.Peng, H.Pereira, V.Peresedov, D.Yu.Peressouko, C.Pinkenburg, M.L. Purschke, A.K.Purwar, H.Qu, J.Rak, A.Rakotozafindrabe, I.Ravinovich, K.F.Read, S.Rembeczki, M.Reuter, K.Reygers, V.Riabov, Y.Riabov, D.Roach, G.Roche, S.D.Rolnick, A.Romana, M.Rosat, S.S. E.Rosendahl, P.Rosnet, P.Rukoyatkin, P.Ruzicka, V.L.Rykov, B.Sahmueller, N.Saito, T.Sakaguchi, S.Sakai, K.Sakashita, H.Sakata, V.Samsonov, S.Sato, T.Sato, S.Sawada, K.Sedgwick, J.Seele, R.Seidl, A.Yu.Semenov, V.Semenov, R.Seto, D.Sharma, I.Shein, A.Shevel, T.-A.Shibata, K.Shigaki, M.Shimomura, K.Shoji, P.Shukla, A.Sickles, C.L.Silva, D.Silvermyr, C.Silvestre, K.S.Sim, B.K. Singh, C.P.Singh, V.Singh, S.Skutnik, M.Slunicka, A.Soldatov, R.A.Soltz, W.E.Sondheim, S.P.Sorensen, I.V.Sourikova, F.Staley, P.W.Stankus, E.Stenlund, M.Stepanov, A.Ster, S.P.Stoll, T.Sugitate, C.Suire, A.Sukhanov, J.Sziklai, T.Tabaru, S.Takagi, E.M.Takagui, A.Taketani, R.Tanabe, Y.Tanaka, K.Tanida, M.J.Tannenbaum, A.Taranenko, P.Tarjan, H.Themann, T.L.Thomas, M.Togawa, A.Toia, J.Tojo, L.Tomasek, Y.Tomita, H.Torii, R.S.Towell, V-N.Tram, I.Tserruya, Y.Tsuchimoto, C.Vale, H.Valle, H.W.va.Hecke, A.Veicht, J.Velkovska, R.Vertesi, A.A.Vinogradov, M.Virius, V.Vrba, E. Vznuzdaev, M.Wagner, D.Walker, X.R.Wang, Y.Watanabe, F.Wei, J.Wessels, S.N.White, D.Winter, C.L.Woody, M.Wysocki, W.Xie, Y.L.Yamaguchi, K.Yamaura, R.Yang, A.Yanovich, Z.Yasin, J.Ying, S.Yokkaichi, G.R.Young, I.Younus, I.E.Yushmanov, W.A.Zajc, O.Zaudtke, C.Zhang, S.Zhou, J.Zimanyi, L.Zolin

主論文

First measurement of ω and ϕ mesons
via di-electron decay channels
in proton+proton collisions at $\sqrt{s} = 200$ GeV

Kotaro M. Kijima

Department of Physical Science, Graduate School of Science
Hiroshima University
Kagamiyama 1-3-1, Higashi-Hiroshima, 739-8526, Japan

January 2012

Abstract

The work in this thesis is to study ω and ϕ meson production in $p+p$ collisions at $\sqrt{s} = 200$ GeV measured via di-electron decay channels using the PHENIX detector at RHIC in Year 2004/2005.

We have measured spectra of differential cross sections of ω and ϕ mesons as a function of transverse momentum in the range of $0 < p_T < 4$ GeV/ c . The ω and ϕ were identified from invariant mass spectra reconstructed by electron and positron pairs extracted from large background of hadrons. The yield of ω and ϕ were statistically subtracted from large amount of background which comes from combinatorial pairs mainly due to π^0 Dalitz decay, photon conversion and other hadron decays. After applying corrections for the PHENIX detector acceptance, electron identification efficiency, trigger efficiency obtained by simulation studies based on GEANT, the cross sections of ω and ϕ meson were obtained.

First measurements of ω and ϕ meson obtained by di-electron decay channel in $p + p$ collisions at $\sqrt{s} = 200$ GeV extend the p_T coverage to zero and allows direct calculation of the total cross sections $d\sigma^\omega/dy = 4.19 \pm 0.33^{stat.} \pm 0.33^{sys.}$ mb and $d\sigma^\phi/dy = 0.431 \pm 0.031^{stat.} \pm 0.028^{sys.}$ mb in the mid-rapidity. The spectra of differential cross sections of ω and ϕ mesons consists an exponential function at low p_T and a power function at high p_T . The Tsallis distribution including both of exponential and power law described the spectra over the wide p_T range obtained by both of di-electron decay channel and hadronic decay channels. The measured spectra of ω and ϕ mesons were in a good agreement with result of an event generator PYTHIA based on perturbative Quantum ChromoDynamics(pQCD) calculation. The various meson spectra $(\pi^+ + \pi^-)/2$, π^0 , $(K^+ + K^-)/2$, K_s^0 , η , ω , ϕ and J/ψ in $p+p$ collisions at $\sqrt{s} = 200$ GeV measured by PHENIX described by Tsallis distribution. The global picture of m_T scaling worked also for these various mesons even quite wide m_T ranges in $p+p$ collisions at $\sqrt{s} = 200$ GeV as well as at previous experiment in $p+p$ and $p+\bar{p}$. Thesis scaling results suggested a similar production mechanism of mesons in $p+p$ collisions at $\sqrt{s} = 200$ GeV.

Due to the chiral symmetry restoration in the hot matter created by the

high energy heavy ions collisions at RHIC, the observation of mass modification of ω and ϕ mesons are expected. On the other hand, the mass modification is not expected in case of $p+p$ collisions, since the matter created by $p+p$ collisions should be much smaller than the life time of these mesons. It is essentially needed to quantitatively evaluate the mass spectra of ω and ϕ mesons in $p+p$ collisions as solid the baseline since attempting observation of mass modification in heavy ion collisions is challenging due to the huge background. By using the model of this analysis for evaluating mass modification in $p+p$ collisions, two parameters corresponding to the ratio of mass shift Δ and the fraction of modified meson yield R were estimated, and the best value were $\Delta = -3.3^{+2.4}_{-3.8}$ %, $R = 7.5^{+4.9}_{-4.9}$ % for ω meson and $\Delta = -1.2^{+0.9}_{-0.8}$ %, $R = 9.7^{+8.0}_{-8.0}$ % for ϕ meson. The results for ω and ϕ mesons are consistent with assumption that no mass shift was observed in $p+p$ collisions within 1.4σ , respectively.

Our results for ω and ϕ meson production in $p+p$ collisions provided a crucial data as a solid baseline to understand physics of heavy ion interactions.

Contents

1	Introduction	15
1.1	Quantum ChromoDynamics	15
1.2	pQCD in Hadron Collision	18
1.3	QCD phase transition	22
1.3.1	Quark Gluon Plasma	22
1.3.2	Chiral Symmetry breaking and restoration	25
1.3.3	Low mass vector meson	27
1.4	Motivation and scopes of this thesis	29
2	Experimental Setup	31
2.1	Relativistic Heavy Ion Collider (RHIC)	31
2.2	the PHENIX Detector	34
2.2.1	Beam Beam Counters (BBC)	34
2.2.2	Zero Degree Counters (ZDC)	37
2.2.3	PHENIX tracking system	37
2.2.4	Ring Image Cherenkov Counters (RICH)	44
2.2.5	Electro Magnetic Calorimeter (EMC)	44
2.3	Data Acquisition system (DAQ)	47
2.4	Event trigger	49
3	Analysis	53
3.1	Outline of Analysis	53
3.2	Run and Trigger Selection	53
3.3	Track Selection and electron identification (eID)	56
3.3.1	Number of Hit PMT (n0)	56
3.3.2	RHIC match	56
3.3.3	EMC match	57
3.3.4	deposition energy over momentum ratio (dep)	58
3.4	Fiducial cut	59
3.5	Pair reconstruction	62
3.6	Background subtraction	62

3.6.1	Fake electron pairs	63
3.6.2	Photon conversion	64
3.6.3	Combinatorial background	66
3.6.4	continuum contribution	69
3.7	Signal Extraction	71
3.7.1	Spectral Shape of Resonances	71
3.7.2	Signal extraction	73
3.8	Monte Carlo simulation	77
3.8.1	Reconstruction efficiency	77
3.8.2	ERT trigger efficiency	82
3.9	Invariant differential cross section	84
3.10	Systematic Uncertainty	87
3.10.1	Total systematic error	87
4	Results and Discussions	89
4.1	Spectra of the invariant cross sections	89
4.2	Integrated cross sections	91
4.3	particle ratio of ω and ϕ to π	98
4.4	Scaling properties	98
4.5	Mass line shape analysis	105
5	Summary and Conclusions	111

List of Figures

1.1	Summary of the value of α_s as a function of the respective energy scale Q [48].	17
1.2	Parton Distribution Function as a function of x at $Q = 5\text{GeV}$ [3].	20
1.3	The fragmentation function for all charged particles as a function of x for different \sqrt{s} in e^+e^- collisions [48].	21
1.4	The phase diagram of QCD in Temperature T and baryon-chemical potential μ_B plane [34].	22
1.5	Nuclear modification factor R_{AA} for π^0 as a function of p_T for minimum bias and five centrality classes in Au + Au collisions in $\sqrt{s_{NN}} = 200$ GeV [36]. Error bars are statistical and p_T uncorrelated errors, boxes around the points indicate p_T correlated errors. Single box around $R_{AA} = 1$ on the left is the error due to N_{coll} , whereas the single box on the right is the overall normalization error of the $p + p$ reference spectrum. . .	24
1.6	Potential of a) QCD vacuum in $T > T_c$. b) QCD vacuum in $T < T_c$	26
1.7	Temperature and density dependence of quark condensate $\langle \bar{q}q \rangle$ [52]	27
2.1	Overview of Brookhaven National Laboratory accelerator complex, consisting of LINAC, booster, AGS and RHIC [70] . . .	32
2.2	The PHENIX Detector configuration [88] The upper panel shows the beam view. Two central arms and central magnet can be seen. The bottom panel shows side view. Two muon arms and muon magnet can be seen.	35
2.3	the PHENIX global coordinate system.	36
2.4	Left) BBC arrays consisting 64 elements. Right) One of the BBC elements consisting quartz Cherenkov radiator and mesh-dynode type PMT.	36
2.5	schematic view of the ZDC location including deflection of protons and charged fragments [74]	38

2.6	Left) overview of the PHENIX Magnets. The line shows the contour of the magnetic. Right) total magnetic field strength as a function of R at the $\theta=0$ symmetry plane of the Central Magnet for +(outer), ++(Outer+Inner), and +-(Outer-Inner) configuration	39
2.7	The layout of wire position of DC. The X1 and X2 wire cells runs in parallel to the beam to perform precise track measurements in $r-\phi$. U1, V1, U2, V2 wires have stereo angle of about 6° relative to the X wires and measure the z coordination of track [78].	40
2.8	the pad and pixel geometry(left), A cell defined by three pixels is at the center of the right picture [78].	41
2.9	Illustration of the track reconstruction in the PHENIX up to PC1 on $x-y$ plane and $r-z$ plane.	42
2.10	A cut through view of RICH detector	45
2.11	Interior view of a lead-scintillator calorimeter module	46
2.12	Exploded view of a lead-glass detector supermodule	46
2.13	block diagram of DAQ [88]	48
2.14	Integrated luminosity as a function of date for 200GeV $p+p$ collisions collected by PHENIX in year2004/2005.	50
2.15	schematic view of EMCAL RICH level1 Trigger: Both the super-Module of EMCAL and RICH are fired for e^+,e^- . Only the EMCAL is fired for photon, while only the RICH is fired for high p_T pion. We are able to effectively collect the events including e^+e^- pair.	51
3.1	Collision vertex distribution. The events in yellow band range are selected for this analysis.	54
3.2	number of electrons per events as a function of collision vertex.	54
3.3	Number of electron in $0.3 < p_T < 4.0\text{GeV}/c$ per sampled Minimum Bias triggered event as a function of run number.	55
3.4	Number of electron detected in EAST (top) and WEST (bottom) arms per sampled Minimum Bias triggered event.	55
3.5	$N_{ERT\&\&MB}^{ERT} / N_{ERT\&\&MB}^{MB}$ as a function of run number. This ratio should be unity when there is no file segment lost at data reconstruction.	56
3.6	Schematic description of the definitions of variable which characterized the RICH ring. The five fit PMTs are shown as an example.	57
3.7	Track quality distribution.	58
3.8	(distribution of n_0 (left) and <i>RICH matching</i> (right).	58

3.9	distribution of <i>EMCal matching</i> for σ_ϕ (left) and σ_z (right) . .	59
3.10	(left) E/p distribution in minimum bias event for all charged tracks, for electron candidates and for randomly associated hadrons .(right) dep distribution applying $n0 > 0$	59
3.11	Alpha vs board distribution for both sides of the DC East and West after applying the fiducial cuts	60
3.12	Occupancy of <i>EMCal</i> sectors after applying the fiducial cuts .	61
3.13	$\Delta\phi$ and Δz distribution for pairs of the tracks in DC. The box represents the cut for removed fake pairs in DC.	63
3.14	The distribution for <i>PFOA</i> and $\Delta RICH$. The detail is in the sentence. The box represents the cut for removed fake pairs for ring sharing tracks.	64
3.15	Φ_V distribution in the mass range $30 < m_{ee} < 90 MeV/c^2$. blue line show the Φ_V distribution reconstructed in event mixing which normalized arbitrary range. Vertical red line on $0.035\pi[rad]$ indicates cut value in this mass region	65
3.16	Schematic view of conversion pair. The electrons produced at $R > 0$ are reconstructed with incorrect momentum.	65
3.17	Invariant mass distribution for all e^+e^- pairs. The filled yellow histogram shows the ghost pairs. The filled blue histogram shows the pairs removed by the ϕ_V angle cut.	66
3.18	like-sign pairs distribution as a function of mass and pair p_T after subtraction of mixed event background. The background is normalized in the normalization area A shown as the dashed area.	68
3.19	invariant e^+e^- mass spectrum. The blue line indicate combinatorial background evaluated by the event mixing method. .	69
3.20	Invariant mass spectra divided by p_T bins. The blue line indicate combinatorial background evaluated by the event mixing method.	70
3.21	Diagrams for final state radiation [90]. The decay into $e^+e^-\gamma$ is described by (a). The infrared divergence in the decay is canceled by interference with the diagrams in (b).	72
3.22	e^+e^- mass spectrum in the radiative decay $\phi \rightarrow e^+e^-\gamma$ for $E_{min} = 10 MeV$ (orange) smeared with $10 MeV$ (red).	73
3.23	Invariant mass spectra divided by p_T bins after background subtraction. The black line are the fitting result, which is sum of the known decays, ω (left magenta line), ϕ (right magenta line), ρ (light blue line), radiative decay of ω and ϕ (orange line) and BG(blue line).	75

3.24	Raw counts in counting range for ω (left) and ϕ (right) mesons as a function of p_T . The black lines show all contributions, the magenta points show ω (left) and ϕ (right) mesons including statistical errors, green line lines show combinatorial background, the light blue lines show ρ mesons, and blue lines show exponential+polynomial as contribution of other hadron continuum.	76
3.25	The PHENIX central arm detectors represented in GEANT simulation	77
3.26	Left panel) RICH n0. Right panel) RICH displacement. . . .	78
3.27	Left panel) EMC match for ϕ direction. Middle panel) EMC match for z direction. Right panel) Energy over momentum ratio normalized that width : dep direction.	78
3.28	Comparison of Drift Chamber hit distribution for ϕ direction in the real data(red) and simulation data(blue). The p_T range of the electron is $0.3 < p_T < 4.0 \text{ GeV}/c$ for both real and simulation data.	79
3.29	Comparison of PC1 hit distribution for z direction in the real data(red) and simulation data(blue). The p_T range of the electron is $0.3 < p_T < 4.0 \text{ GeV}/c$ for both real and simulation data.	80
3.30	Left panel) The invariant mass spectra for ω meson reconstructed e^+e^- in simulation for the $1.0 \leq p_T < 1.25 \text{ GeV}/c$. The solid line shows Gaussian convoluted relativistic Breit-Winger function. Right panel) p_T dependent detector mass resolution.	81
3.31	Left panel) The invariant mass spectra for ϕ meson reconstructed e^+e^- in simulation for the $1.0 \leq p_T < 1.25 \text{ GeV}/c$. The solid line shows Gaussian convoluted relativistic Breit-Winger function. Right panel) p_T dependent detector mass resolution.	81
3.32	Reconstruction efficiency for ω and ϕ mesons ϵ_{pair}^{reco} as a function of p_T	82
3.33	(left) The p_T distribution for single electron in MB(black) and fired ERT(red). (right) Trigger efficiency for single electrons ϵ_{single}^{ERT} as a function of p_T	83
3.34	Trigger efficiency for ω (blue) and ϕ (red) mesons ϵ_{pair}^{ERT} as a function of p_T	84
3.35	Bin shift correction for ω . Blue point and line shows before correction, and red point shows after correction.	86

3.36	Bin shift correction for ϕ . Blue point and line shows before correction, and red point shows after correction.	86
4.1	Invariant cross section of ω and ϕ production in $p + p$ collision at $\sqrt{s}= 200\text{GeV}$ measured in $\omega \rightarrow e^+e^-$ and $\phi \rightarrow e^+e^-$ decay channels as a function of p_T . Bars and boxes represent statistical and systematic errors, respectively.	90
4.2	(Top)The invariant cross section of ω production in $p + p$ collision at $\sqrt{s}= 200\text{GeV}$ measured in $\omega \rightarrow e^+e^-$, $\pi^0\pi^+\pi^-$ and $\pi^0\gamma$ decay channels. The curves show Levy(red), modified Power-law(Green) and Exponential(black) fit to the data measured in both dilepton and hadronic decay modes. (Bottom)Ratio of the data and Levy fit.	92
4.3	Invariant cross section of ϕ production in $p + p$ collision at $\sqrt{s}= 200\text{GeV}$ measured in $\phi \rightarrow e^+e^-$, K^+K^- decay channels. The curves show Levy(red), modified Power-law(Green) and Exponential(black) fit to the data measured in both dilepton and hadronic decay modes. (Bottom)Ratio of the data and Levy fit.	93
4.4	The invariant cross section of ω production in $p + p$ collision at $\sqrt{s}= 200\text{GeV}$ compared with PYTHIA version 6.421 with Tune A.	94
4.5	Invariant cross section of ϕ production in $p+p$ collision at $\sqrt{s}= 200\text{GeV}$ compare with PYTHIA version 6.421 with Tune A.	95
4.6	Ratio of cross section, σ_ω/σ_π (square) and σ_ϕ/σ_π (circle), measured for $p + p$ data as a function of center-of-mass energy.	96
4.7	Measured ω/π^0 as a function of p_T in p+p collisions at $\sqrt{s} = 200\text{GeV}$. Straight lines show fits to a constant for $2 < p_T < 3\text{GeV}/c$	100
4.8	Measured ϕ/π^0 as a function of p_T in p+p collisions at $\sqrt{s} = 200\text{GeV}$. Straight lines show fits to a constant for $3 < p_T < 7\text{GeV}/c$	100
4.9	Spectra of invariant differential cross section as a function of p_T for $(\pi^+ + \pi^-)/2$, π^0 , $(K^+ + K^-)/2$, K_s^0 , η , ω , ϕ and J/ψ in $p + p$ collision at $\sqrt{s}= 200\text{GeV}$ at mid-rapidity.	101
4.10	Scaled spectra of invariant differential cross section as a function of p_T for $(\pi^+ + \pi^-)/2$, π^0 , $(K^+ + K^-)/2$, K_s^0 , η , ω , ϕ and J/ψ in $p+p$ collision at $\sqrt{s}= 200\text{GeV}$ at mid-rapidity. Solid line expressed pure power law function fitted in $5.0 < p_T < 20\text{GeV}/c$.	102

- 4.11 (top) m_T spectra for $(\pi^+ + \pi^-)/2$, π^0 , $(K^+ + K^-)/2$, K_s^0 , η , ω , ϕ and J/ψ in $p + p$ collision at $\sqrt{s} = 200\text{GeV}$ at mid-rapidity. (Bottom) The ratio of the spectra to Levy fit to π . Bars show uncertainties combined with statistical and systematic errors. 103
- 4.12 Scaled m_T spectra for $(\pi^+ + \pi^-)/2$, π^0 , $(K^+ + K^-)/2$, K_s^0 , η , ω , ϕ and J/ψ in $p + p$ collision at $\sqrt{s} = 200\text{GeV}$ at mid-rapidity. 104
- 4.13 Schematic representation of the model to evaluate mass spectra with mass shift. The shapes of $f(m_{ee})$ and $f'(m_{ee})$ represent the measured spectra of vector meson decaying outside and inside medium, respectively. 106
- 4.14 Invariant mass distribution with fitting results for ω mesons for three p_T bins corresponding to the weighted average of $\langle\beta\gamma\rangle = 1.01, 2.04, 4.85$. Blue line shows $F(m_{ee})$, magenta and light blue line correspond to f and f' , respectively. The dash line shows the fit result with $\Delta = 0$ and $R = 0$. The green line shows ρ meson contribution. 107
- 4.15 a) and b) show χ^2 distribution as a function of $(1+\Delta)$ and R for ω meson, respectively. The red points are best fit value. . . 108
- 4.16 χ^2 distribution in 2-dimensional space for $(1 + \Delta)$ and R for ω meson. The red point is best fit value and the bars are statistical errors corresponding to $\Delta\chi^2 = +1$ 108
- 4.17 Invariant mass distribution with fitting results for ω mesons for three p_T bins corresponding to weighted average of $\langle\beta\gamma\rangle = 0.74, 1.82, 3.68$. Blue line shows $F(m_{ee})$, magenta and light blue line correspond to f and f' , respectively. The dash line shows the fit result with $\Delta = 0$ and $R = 0$. The green line shows ρ meson contribution. 109
- 4.18 a) and b) show χ^2 distribution as a function of $(1 + \Delta)$ and R for ϕ meson, respectively. The red points are best fit value. 110
- 4.19 χ^2 distribution in 2-dimensional space for $(1 + \Delta)$ and R for ϕ meson. The red point is best fit value and the bars are statistical errors corresponding to $\Delta\chi^2 = +1$ 110

List of Tables

1.1	Summary of up, down, strange quarks. [48]	16
1.2	Summary of charm, bottom, top [48]	16
1.3	Summary of gauge bosons [48]	16
1.4	Suggested qq quark-model assignment for some of the observed light mesons. [48]	18
2.1	summary of the RHIC operation. The integrated luminosity is recorded in PHENIX.	33
2.2	Summary of the track quality	44
2.3	Summary of parameters of two type of PHENIX EMCAL	45
3.1	Electron ID cuts used in this analysis.	60
3.2	The pole masses and natural decay widths of the vector mesons taken from the PDG [48]	71
3.3	Total systematic error for ω meson	88
3.4	Total systematic error for ϕ meson	88
4.1	Summary of fitting parameters	97

Chapter 1

Introduction

1.1 Quantum ChromoDynamics

Quantum Chromodynamics (QCD) is the gauge field theory which describes the strong interaction of colored quarks and gluons. A quark has a specific flavor as shown in Table.1.1 and Table.1.2 and one color of three, red, green and blue. The gluon has a color of the eight. The hadrons are color-singlet combinations of quarks and anti-quarks, and gluons. The classical QCD Lagrangian describing the interaction of quarks and gluons is

$$L_{QCD} = -\frac{1}{4}F_{\mu\nu}^a F_a^{\mu\nu} + \bar{q}(i\gamma^\mu D_\mu - \mathbf{M})q \quad (1.1)$$

The D_μ is a covariant derivative defined as

$$D_\mu \equiv \partial_\mu + ig_s t^a A_\mu^a \quad (1.2)$$

The $F_{\mu\nu}^a$ is the field tensors of the gluon given by

$$F_{\mu\nu}^a = \partial_\mu A_\nu^a - \partial_\nu A_\mu^a - g_s f_{abc} A_\mu^b A_\nu^c \quad (1.3)$$

where Ψ_q corresponds to the field of each quark of colors and flavors, the A_μ^a corresponds to the gluon gauge field, g_s is the QCD coupling constant, γ^μ are Dirac matrices defined as, $\gamma^\mu \gamma^\nu + \gamma^\nu \gamma^\mu = 2g^{\mu\nu}$, and f_{abc} is the structure constant of the SU(3). The \mathbf{M} represents the diagonal matrix of “current quark masses” as shown in Table.1.1.

Asymptotic freedom and confinement

The QCD successfully describes the strong interaction, which is characterized by two specific features. One is asymptotic freedom and the other is confinement.

	u	d	s
Q -electric charge	$+\frac{2}{3}$	$-\frac{1}{3}$	$-\frac{1}{3}$
J -spin	$\frac{1}{2}$	$\frac{1}{2}$	$\frac{1}{2}$
I_z -isospin	$+\frac{1}{2}$	$-\frac{1}{2}$	0
S -strangeness	0	0	-1
C -charm	0	0	0
B -bottomness	0	0	0
T -topness	0	0	0
mass [MeV/ c^2]	1.5-3.0	3.0-7.0	95 ± 25

Table 1.1: Summary of up, down, strange quarks. [48]

	c	b	t
Q -electric charge	$+\frac{2}{3}$	$-\frac{1}{3}$	$+\frac{2}{3}$
J -spin	$\frac{1}{2}$	$\frac{1}{2}$	$\frac{1}{2}$
I_z -isospin	0	0	0
S -strangeness	0	0	0
C -charm	+1	0	0
B -bottomness	0	-1	0
T -topness	0	0	+1
mass [GeV/ c^2]	1.25 ± 0.09	4.20 ± 0.07	174.2 ± 3.3

Table 1.2: Summary of charm, bottom, top [48]

	γ	W^+	W^-	Z	g
Q -electric charge	0	+1	-1	0	0
J -spin	1	1	1	1	1
mass [GeV/ c^2]	0	80.39	80.29	91.18	0
relative strength	10^{-2}	10^{-13}			1

Table 1.3: Summary of gauge bosons [48]

The running coupling constant $g(\mu)$ is defined as an effective coupling strength among quarks and gluons at the energy scale μ . The effective cou-

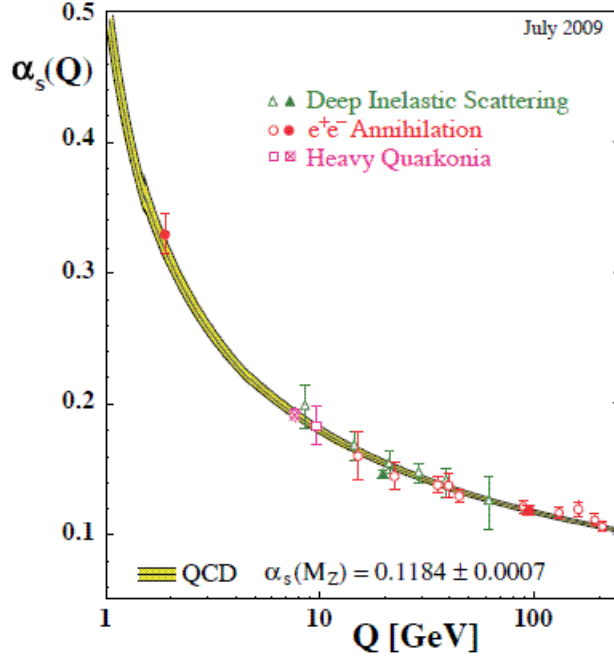


Figure 1.1: Summary of the value of α_s as a function of the respective energy scale Q [48].

pling constant $\alpha_s(\mu)$ is expressed as follows

$$\alpha_s(\mu) \equiv \frac{g(\mu)^2}{4\pi} \quad (1.4)$$

$$\simeq \frac{1}{4\pi\beta_0 \ln(\mu/\Lambda_{QCD}^2)} \left(1 - \frac{\beta_1}{\beta_0^2} \frac{\ln[\ln(\mu^2/\Lambda_{QCD}^2)]}{\ln(\mu^2/\Lambda_{QCD}^2)} \right) \quad (1.5)$$

where $\beta_0 = (11 - \frac{2}{3}N_f)/(4\pi)^2$, $\beta_1 = (102 - \frac{38}{3}N_f)/(4\pi)^4$, N_f is the number of flavors, and Λ_{QCD} is called the QCD scale parameter. The running coupling constant α_s determined by data from several experiments is shown in Fig.1.1.

Fig.1.1 and Eq.1.5 tell us that the running coupling constant α_s decreases logarithmically as μ increase. This means that for short distance the strength of strong interaction is relatively weak unlike Quantum Electrodynamics(QED). This property of the interaction at short distance is called "asymptotic freedom". Due to the small α_s at large mu , perturbative Quantum ChromoDynamics(pQCD) calculation are possible and it can describe the hadron-hadron interaction as shown Section 1.2.

On the other hand, Fig.1.1 and Eq.1.5 indicate that the running coupling constant increase and become strong at low energy, $\mu \sim \Lambda_{QCD} \sim 200\text{MeV}$. This is the typical energy scale as confinement of quarks and gluons and the dynamical symmetry breaking as shown in Section 1.3.2. Then, the perturbative approach is not applicable. As a consequence of confinement, isolated color has never been observed experimentally, which indicates that the quarks and gluons are always bound together to form color-white as hadrons. For example, the suggested $q\bar{q}$ quark-model assignments for some of the observed light mesons are shown in Table.1.4. If the orbital angular momentum of the $q\bar{q}$ state is l , then the parity P is $(-1)^{l+1}$. The meson spin J is given by the relation $|l - s| < J < |l + s|$ where s is 0 or 1 corresponding to antiparallel quark spin or parallel quark spin, respectively. The charge conjugation C is $(-1)^{l+s}$.

J^{PC}	I=1 $u\bar{d}, \bar{u}d, \frac{1}{\sqrt{2}}(d\bar{d} - u\bar{u})$	I=1/2 $u\bar{s}, d\bar{s}; \bar{d}s, -\bar{u}s$	I=0 f'	I=0 f
0^{-+}	π	K	η	$\eta'(958)$
1^{--}	$\rho(770)$	$K^*(892)$	$\phi(1020)$	$\omega(782)$
0^{++}	$a_0(1450)$	$K_0^*(1430)$	$f_0(1710)$	$f_0(1370)$
1^{++}	$a_1(1260)$	K_{1A}^*	$f_1(1420)$	$f_1(1285)$

Table 1.4: Suggested qq quark-model assignment for some of the observed light mesons. [48]

1.2 pQCD in Hadron Collision

Many experimental data of hadron production in $p+p$ and $p+\bar{p}$ collisions are existing [4–15]. In the parton model, the hard scattering process of the two hadrons at high energy is represented as the interaction of the quarks and gluons which are the constituents of initial hadrons. For example, the cross section of the hadron production for a hard scattering process in $p+p$ collision can be expressed as follows,

$$\begin{aligned} \sigma^{pp \rightarrow hX} &= \sum_{f_1, f_2, f} \int dx_1 dx_2 dz \cdot f_1^p(x_1, \mu^2) \cdot f_2^p(x_2, \mu^2) \\ &\times \sigma^{f_1 f_2 \rightarrow fX}(x_1 p_1, x_2 p_2, p_h, \mu) \times D_f^h(z, \mu^2) \end{aligned} \quad (1.6)$$

where μ is the factorization scale, f_1, f_2, f represent parton, $f_1^p(x_1, \mu)$ is parton distribution function(PDF) of parton in incoming 1st proton, $f_2^p(x_2, \mu)$ is parton distribution function(PDF) of parton in incoming 2nd proton, $D_f^h(z_h, \mu^2)$ is fragmentation function (FF) from parton f to final state hadron h , p_1 and p_2 are the momentum of initial protons, x is the momentum fraction of the initial parton in initial proton, z is the momentum fraction of the final state hadron in the final parton.

The picture of the parton model as shown in Eq.1.6 is represented by the convolution of the tree parts; one is a parton distribution function f_i^p which represents probability for finding a type of parton in the proton, another is a parton-parton scattering cross section $\sigma^{f_1 f_2 \rightarrow f X}$, the other is a fragmentation function D_f^h which represents the hadronization mechanism. It is difficult to calculate the parton distribution function and the fragmentation function by the first principles in QCD at present. On the other hand, the parton-parton scattering cross section $\sigma^{f_1 f_2 \rightarrow f X}$ can be calculated by pQCD.

The cross section is required to satisfy in the following condition,

$$\mu \frac{d\sigma^{pp \rightarrow hX}}{d\mu} = 0 \quad (1.7)$$

because the cross section must be independent of the arbitrary scale μ . Although the optimization of the scale is discussed in several theoretical groups [56].

Parton Distribution Function(PDF)

The parton distribution function is the probability density for finding a type of parton in the proton. The proton structure function $F_2(x, Q^2)$ is measured by lepton deep inelastic scattering (DIS) in many experiments: using electron-proton scattering at DESY, SLAC, and muon-proton scattering at FNAL. The ratio of \bar{d}/\bar{u} is extract from the ratio of lepton pair Drell-Yan production in $p + p$ and $p + d$ collisions measured by NA51 [53] and E866 [54]. The ratio of d/u is extracted from the asymmetry between $W \rightarrow l^\pm \nu$ measured by CDF. The gluon density is given by the inclusive jet production and direct photon production.

The parton distribution function is tried to extract from experimental data by several theoretical groups. An example of the global analysis based on the next-to-leading-order(NLO) pQCD calculation is shown in Fig.1.2.

Fragmentation Function(FF)

The fragmentation function, $D_h^k(z, Q^2)$, is the probability density for finding a hadron h with the fraction of momentum z in the final parton k . The

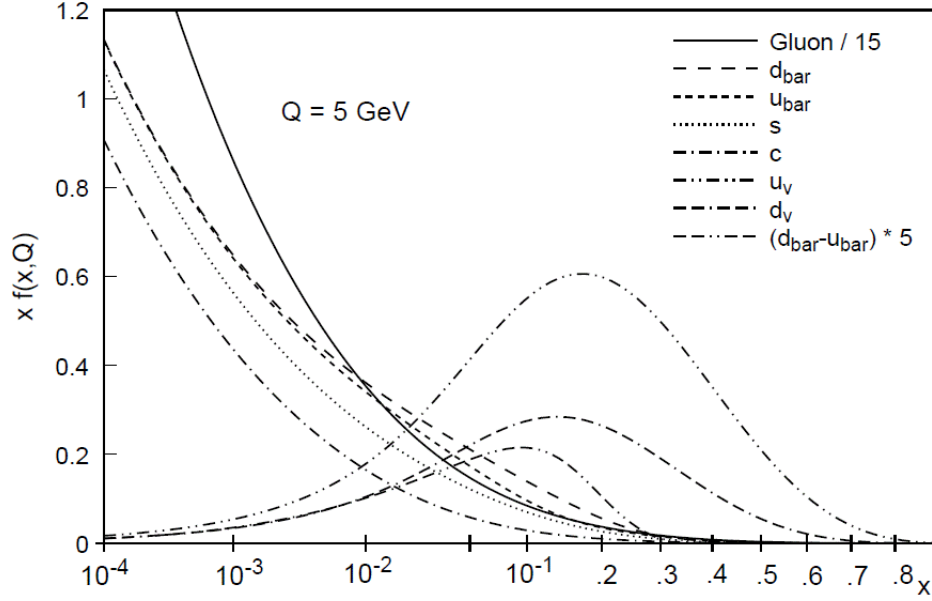


Figure 1.2: Parton Distribution Function as a function of x at $Q = 5\text{ GeV}$ [3].

fragmentation function satisfies the sum rule as follows:

$$\sum_h \int z D_k^h(z, Q^2) dz = 1 \quad (1.8)$$

The fragmentation function is measured by ALEPH [17, 18], OPAL [19–22], DELPHI [23] and L3 [24] at CERN, HRS [25], MARKII [26, 27] and TPC [28] at SLAC, TASSO [29, 30] at DESY, AMY [31] at KEK in $e^+ + e^-$ collisions using the $e^+ + e^- \rightarrow \gamma$ or $Z \rightarrow h + X$. The fragmentation function for all charged particles in e^+e^- collisions is shown in Fig.1.3 [48].

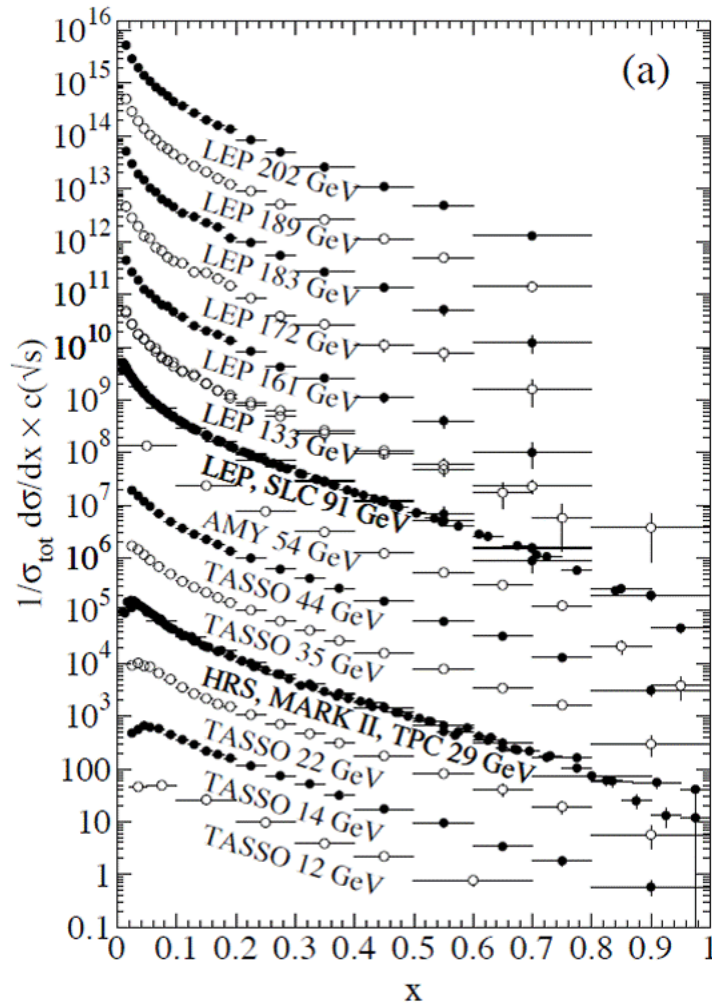


Figure 1.3: The fragmentation function for all charged particles as a function of x for different \sqrt{s} in e^+e^- collisions [48].

1.3 QCD phase transition

1.3.1 Quark Gluon Plasma

The ordinary matter consists of proton and neutrons in which quarks and gluons are confined. In the extreme condition as high temperature and/or dense density, QCD suggests taht the quarks and gluons does not any more confined normal hadrons. The state of matter consisting of many-body system of deconfined quarks and gluons is called as "Quark Gluon Plasma"(QGP) [32]. The lattice QCD calculation based on the first principle QCD is most powerful tool to predict the transition temperature from hadronic matter to QGP. Fig.1.4 shows the QCD phase diagram for two massless quarks as a function of temperature T and baryon chemical potential μ_B [34]. The normal nuclear matter at zero temperature indicates 1 GeV since the μ_B corresponds to the energy of the system per baryon number. The model calculation suggest that for finite baryon chemical potential $\mu_B > 0$ and small value of temperature the transition hadronic matter to QGP is a first order phase transition. On the other hand, lattice calculation at vanishing μ_B suggest that for the transition to the high temperature phase of QCD is crossover. The critical temperature at $\mu_B = 0$ from lattice calculations is 172 ± 11 MeV [35]

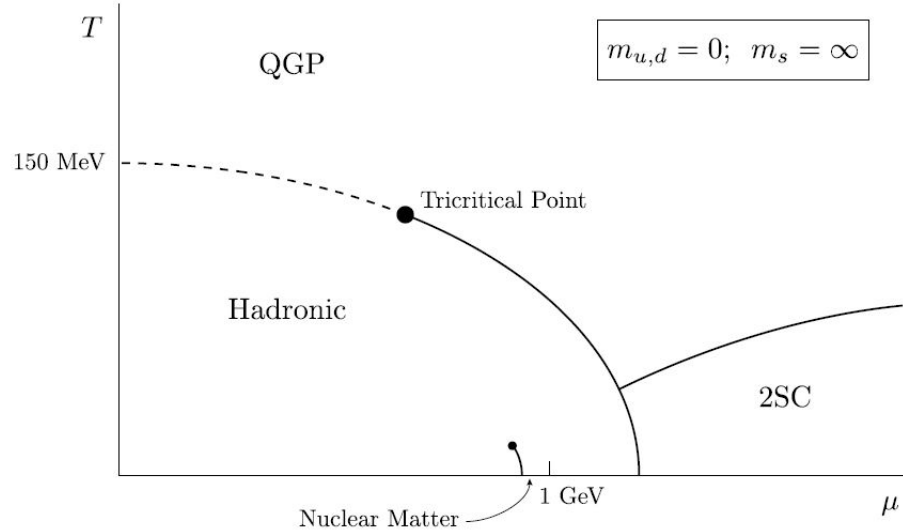


Figure 1.4: The phase diagram of QCD in Temperature T and baryon-chemical potential μ_B plane [34].

The large experimental observation for signature of QGP implies the formation of QGP in heavy ion collisions at Relativistic Heavy Ion Collider (RHIC) in Brookhaven National Laboratory (BNL). We briefly review the most important experimental signature of QGP, high transverse momentum particle suppression and strong elliptic flow.

High p_T suppression

The point-like hard scattering with large momentum exchange between partons in the incoming nucleon is well described by perturbative QCD as introduced in Sec. 1.2. The scattered partons emerge back-to-back direction and fragment into a pair of hadron jets. In such process, the high transverse momentum particles produced. If the hot and dense matter is created in nucleus-nucleus collisions ($A + A$), the scattered partons pass through the matter created in the $A + A$ collisions. Therefore, these high transverse momentum particles may be suppressed due to an energy loss by parton-matter interaction in the matter. In contrast, the particle production in $A + A$ collisions is described by the superposition of the particle production in $p + p$ collisions when no such effects are present.

To quantify the high p_T particle production in $A + A$ collisions comparing with $p + p$ collisions, the nuclear modification factor R_{AA} is defined as

$$R_{AA} = \frac{d^2 N^{AA}/dydp_T}{\langle N_{coll} \rangle \times d^2 N^{pp}/dydp_T} \quad (1.9)$$

where p_T is the transverse momentum, y is the rapidity, $d^2 N^{AA}/dydp_T$ and $d^2 N^{pp}/dydp_T$ is the differential yield per event in $A + A$ collisions and $p + p$ collisions, respectively. $\langle N_{coll} \rangle$ is the number of inelastic binary nucleon-nucleon collisions. $\langle N_{coll} \rangle$ depends on impact parameter of collision event and is calculated by Glauber Monte-Carlo simulation. If $R_{AA} = 1$, this indicates that the particle production in $A + A$ collisions is described by the superposition of the particle production in $p + p$ collisions.

The PHENIX experiment reported the nuclear modification factor R_{AA} and large suppression of high p_T various neutral and charged hadron yield in central Au + Au collisions with respect to the result in $p + p$ collisions scaled by number of nucleus-nucleus binary collisions [36–43]. The nuclear modification factor R_{AA} for neutral pions in central to peripheral Au + Au collisions at $\sqrt{s_{NN}} = 200$ GeV is shown in Fig. 1.5 [36]. In the central Au + Au collisions, R_{AA} indicates the yield is strongly suppressed by the factor of ~ 5 at $p_T > 5$ GeV/ c compared to the binary scaled $p + p$ reference. While as becoming the central to peripheral collisions, R_{AA} approaches unity $R_{AA} = 1$ as it is interpreted that the size of the medium should be smaller.

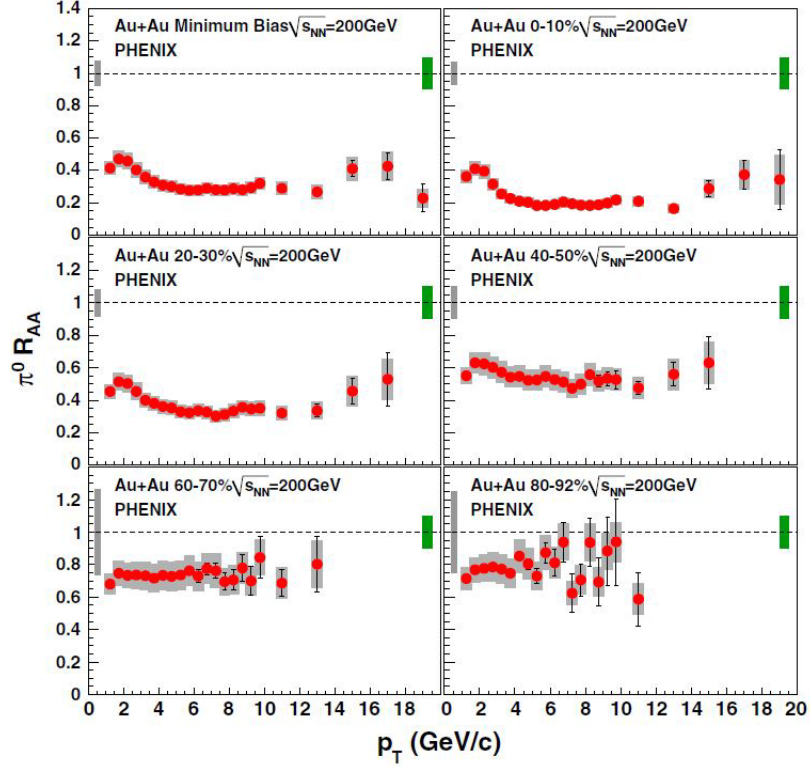


Figure 1.5: Nuclear modification factor R_{AA} for π^0 as a function of p_T for minimum bias and five centrality classes in Au + Au collisions in $\sqrt{s_{NN}} = 200$ GeV [36]. Error bars are statistical and p_T uncorrelated errors, boxes around the points indicate p_T correlated errors. Single box around $R_{AA} = 1$ on the left is the error due to N_{coll} , whereas the single box on the right is the overall normalization error of the $p + p$ reference spectrum.

The modification factor in $d + Au$ collisions, R_{dAu} reflects the contributions of initial state normal nuclear effect such as Cronin effect [44], the nuclear modified parton distribution functions (nPDFs) [46] and gluon saturation [45]. As a consequence of observation of R_{AA} and R_{dA} , The data suggest that the suppression at high p_T particles in Au + Au collisions is due to final state interactions in the extremely dense medium produced by the collisions.

1.3.2 Chiral Symmetry breaking and restoration

The left-handed and right-handed quarks as two eigenstates of chirality operator, γ^5 with the eigenvalues ± 1 can be describe as follows

$$q_L = \frac{1 - \gamma^5}{2}q, \quad q_R = \frac{1 + \gamma^5}{2}q. \quad (1.10)$$

For the massless quarks, the chirality is equivalent to the helicity $\mathbf{s} \cdot \mathbf{p}/|\mathbf{s} \cdot \mathbf{p}|$. Then the quark mass, M , becomes an $N_f \times N_f$ matrix, the QCD Lagrangian Eq.1.1 may be decomposed as follows

$$L_{QCD} = -\frac{1}{4}F_{\mu\nu}^a F_a^{\mu\nu} + \bar{q}_L i\gamma^\mu D_\mu q_L + \bar{q}_R i\gamma^\mu D_\mu q_R - (\bar{q}_L \mathbf{M} q_R + \bar{q}_R \mathbf{M} q_L). \quad (1.11)$$

It is clear from this expression that, in the limiting case where $m = 0$, the QCD Lagrangian Eq.1.1 are invariant under the global transformation (chiral transformation):

$$q_L \rightarrow e^{-i\lambda^j \theta_L^j} q_L \quad (1.12)$$

$$q_R \rightarrow e^{-i\lambda^j \theta_R^j} q_R \quad (1.13)$$

where the $\theta_{R,L}^j$ ($j = 0, 1, \dots, N_f - 1$) are space time independent parameters and $\lambda^0 = \sqrt{2/N_f}$, $\lambda^j = 2t^j$ ($j = 1, \dots, N_f - 1$). This is called chiral symmetry.

In the real world where quarks have a finite current mass, chiral symmetry is explicitly broken by the mass term, $-(\bar{q}_L \mathbf{M} q_R + \bar{q}_R \mathbf{M} q_L)$, in the Lagrangian. However, the current masses of u and d quarks is quite small comparing with $\Lambda_{QCD} \sim 200\text{MeV}$. Therefore, the chiral symmetry is expected to be an approximate symmetric in the light quark sector of QCD Lagrangian.

The symmetry is broken due to a non-vanishing ground state expectation value of the QCD vacuum for the quark condensate $\langle \bar{q}q \rangle$. The QCD vacuum $|0\rangle$ at zero temperature and density is considered. According to recent lattice QCD calculation, the order parameter $\langle 0|\bar{q}q|0\rangle = \langle 0|\bar{q}_R q_L + \bar{q}_L q_R|0\rangle$ is non-zero, $\langle 0|\bar{q}q|0\rangle = \sim -[251\text{MeV}]^3$ [55]. This result implies that QCD vacuum is the Bose-Einstein condensate of quark-antiquark pairs $\langle \bar{q}q \rangle$ and has a power to change left-handed quarks to right-handed quarks as well as right-handed quarks to left-handed quarks. Namely, the chiral symmetry is spontaneously broken and the condensate induces a dynamical quark mass.

Y.Nambu and G.Jona-Lasinio (NJL) introduced a model of dynamical mechanism of the chiral phase transition inspired by the phase transition of the superconductivity, in which the chiral condensate $\langle \bar{q}q \rangle$ corresponds to pair of the electron $\langle e^\uparrow e^\downarrow \rangle$ [49–51]. The QCD Lagrangian is expressed by NJL model as

$$L_{QCD} = \bar{q}i\gamma\partial_\mu q + \frac{1}{2}g((q\bar{q})^2 + (\bar{q}i\gamma^5\tau q)^2) \quad (1.14)$$

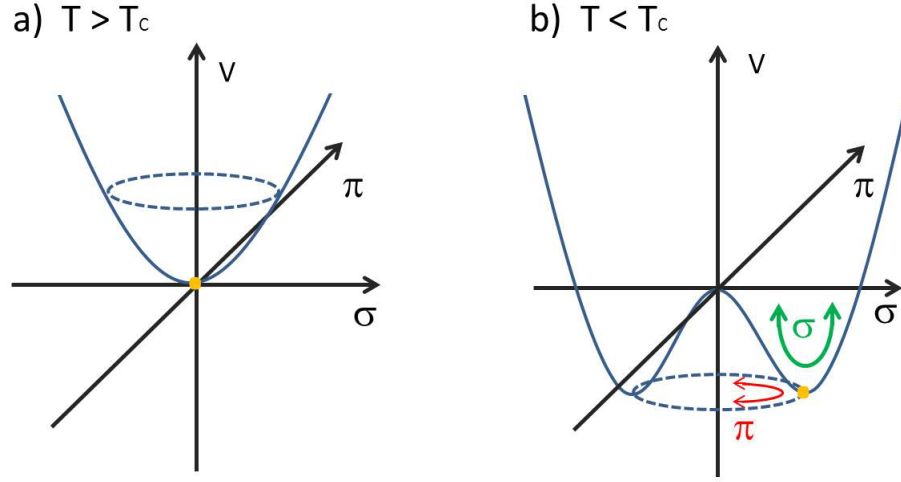


Figure 1.6: Potential of a) QCD vacuum in $T > T_c$. b) QCD vacuum in $T < T_c$.

This Lagrangian can be re-written by the linear sigma model as

$$L_{QCD} = \frac{1}{2}[(\partial_\mu \sigma)^2 + (\partial_\mu \pi)^2] + V(\sigma^2 + \pi^2) \quad (1.15)$$

where σ and π meson field are defined as

$$\sigma = \bar{q}q \quad (1.16)$$

$$\pi = \bar{q}i\gamma^5\tau q \quad (1.17)$$

Then, The π meson is created with zero mass as Nambu-Goldstone boson as result of chiral symmetry breaking. It is supported by the small mass of π meson as compared to other hadrons.

In the chiral symmetric phase, all states of hadrons have a chiral partner with opposite parity and same mass as doublet of parity. But experimental results indicate the chiral partners does not exist at the same masses. For instance, the mass of ρ meson ($J^{PC} = 1^{--}$: vector meson) is $770 MeV/c^2$, while the mass of the chiral partner A_1 meson ($J^{PC} = 1^{++}$: axial-vector meson), is $1250 MeV/c^2$. This is also direct evidence of dynamical breaking of chiral symmetry.

As the temperature and/or density increase, the $\langle q\bar{q} \rangle$ pair is dissociated and eventually the transition to chiral symmetric phase will take place [52]. The experimental observation of the effect of chiral symmetry restoration

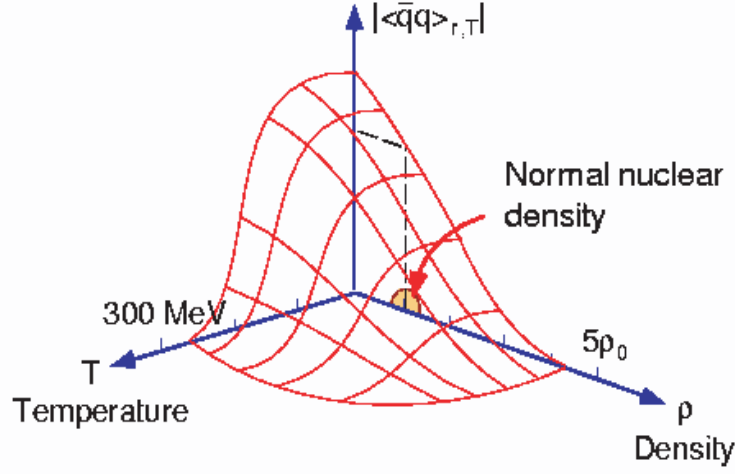


Figure 1.7: Temperature and density dependence of quark condensate $\langle \bar{q}q \rangle$ [52]

is essential to investigate the mechanism of generating hadron mass. But unfortunately the quark condensate $\langle \bar{q}q \rangle$ is not an observable and need the probe to investigate the effect of chiral symmetry restoration. According to the QCD sum rule, which can relate the hadronic spectral function to the QCD condensate, a modification of the hadron mass spectra, especially low mass vector mesons (ρ, ω, ϕ), are expected due to the partial chiral symmetry restoration in hot and/or dense environment [57]. Therefore, the low mass vector meson is powerful probe and the measurement of mass modification at hot and/or dense environment must be great interest.

1.3.3 Low mass vector meson

The light vector mesons (ρ, ω, ϕ) are theoretically most powerful probe to obtain the information related to quark condensate $\langle \bar{q}q \rangle$ as its mass modification in hot and/or dense medium due to their short life times which means larger probability of decaying in medium [57]. In addition, there are decay mode to di-lepton pairs of e^+e^- and $\mu^+\mu^-$. Di-leptons are excellent tool to study possible in-medium modification of vector mesons in the hot and/or dense medium, since the final state lepton is not strongly interact with the medium. Therefore, measurement of vector mesons via di-lepton pairs can extract clean information of mass in the medium. The large mounts of experimental efforts have been reported and continued by using various collision

system in CERES(NA45) [58,59], NA60 [60] at CERN, E325 [61–64] at KEK, E01-112(g7) [65] at J-Laboratory and CBELSA/TAPS [66].

1.4 Motivation and scopes of this thesis

Precise measurements of hadron production in $p+p$ collisions are essential for deeply understanding QCD phenomena such as parton dynamics and hadronization. That also provide a valuable baseline for particle production in heavy ion collision.

At high p_T region, the hadron spectra for the invariant differential cross section can be described by perturbative QCD as shown Section 1.2 and display a power-law behavior called "hard" process. On the other hand, at low p_T region, typically $p_T < 2$ GeV/c, the perturbative approach is not applicable. In addition, the contribution of the multiple parton interaction makes difficult to describe the behavior. The spectra at low p_T region is expected to be exponential behavior like thermal model called "soft" process in heavy ion collisions but it's not established in $p+p$ collision. In this way, the phenomena still has not been fully understood even so in case of $p+p$ collisions.

The observation of the mass modification for the light vector meson due to the partial chiral symmetry restoration in heavy ion collisions is expected as introduced in Section 1.3.2. But it is challenging assignment due to the large combinatorial background from other hadrons. Therefore, it is important to provide the baseline in $p+p$ collisions for analyzing mass spectra of light vector mesons in heavy ion collisions. In $p+p$ collisions, the modification of the mass spectra is not expected, since the system size crating the collision is much smaller than the life time of ϕ and ω mesons. The procedure to evaluate the mass shape assuming with modification in $p+p$ collisions will be considered as baseline for heavy ion physics.

We, PHENIX collaboration, are able to measure various hadrons simultaneously at mid-rapidity in $p+p$ collisions at $\sqrt{s}=200$ GeV. In this study, we measured the production of ω and ϕ meson via e^+e^- decay channel at lower transverse momentum range $0 < p_T < 4$ GeV/c in $p+p$ collisions at $\sqrt{s} = 200$ GeV. Moreover we will mention about analysis result of mass spectra of ω and ϕ meson and the scaling property of various hadrons (π , K , η , ω , ϕ , J/Ψ) at mid-rapidity in $p+p$ collisions at $\sqrt{s}=200$ GeV.

This thesis consists of follows. Chapter 2 gives a description of the PHENIX experimental setup and detector subsystems. Chapter 3 describes the analysis methods including electron identification, reconstruction of ω and ϕ mesons via e^+e^- decay channel and simulation studies. Chapter 4 shows results of ω and ϕ meson production including discussions of mass spectra and scaling properties. Chapter 5 is finally the conclusion of this analysis.

Chapter 2

Experimental Setup

The RHIC complex and PHENIX detector are overviewed in this chapter. The description of the RHIC complex is described in Section 2.1, and the PHENIX detectors is described in Section 2.2.

2.1 Relativistic Heavy Ion Collider (RHIC)

The Relativistic Heavy Ion Collider (RHIC) [69] at Brookhaven National Laboratory (BNL) in the United State was built to study the nuclear physics. The maximum energy at RHIC for heavy ion is 100GeV per nucleon and that for proton is 250GeV. The heavy ion and proton produced at the source are transported through a Tandem Van de Graaff and proton linac, respectively, and accelerate at Booster Synchrotron and the Alternating Gradient Synchrotron (AGS), after that, injected to RHIC. The RHIC ring has a circumference of 3.8km with the maximum bunch of 120 and the designed luminosity is $2 \times 10^{26} \text{ cm}^{-2} \text{ s}^{-1}$ for Au ion and $2 \times 10^{32} \text{ cm}^{-2} \text{ s}^{-1}$ for proton. The RHIC consists of two quasi-circular concentric rings, one("Blue Ring") for clockwise and the other("Yellow Ring") for counter-clockwise. The rings cross at six interaction points. Four experiments, PHENIX, STAR, BRAHMS and PHOBS are build in each one of six interaction points.

The PHENIX, the Pioneering High Energy Nuclear Interaction eXperiment [71], is one of four experiments and specialized experiment for measurement of lepton and photon. In this analysis, the data collected by PHENIX was used. The Detector design is described in the next subsection.

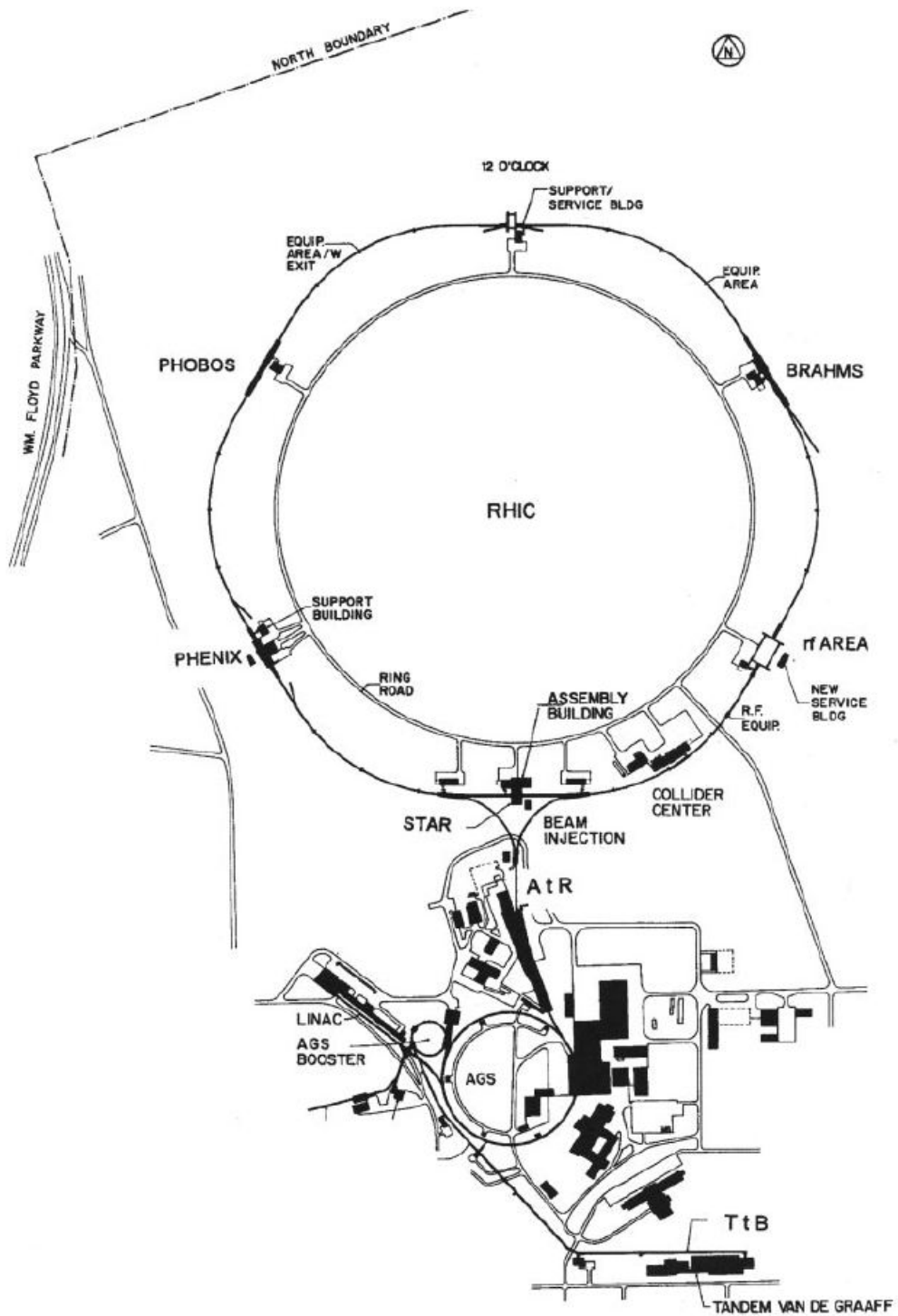


Figure 2.1: Overview of Brookhaven National Laboratory accelerator complex, consisting of LINAC, booster, AGS and RHIC [70]

RUN	Year	Species	$\sqrt{S_{NN}}$	$\int Ldt$
01	2000	Au+Au	130	$1 \mu b^{-1}$
02	2001/2002	Au+Au	200	$24 \mu b^{-1}$
		p+p	200	$0.15 pb^{-1}$
03	2002/2003	d+Au	200	$2.74 nb^{-1}$
		p+p	200	$0.35 pb^{-1}$
04	2004	Au+Au	200	$241 \mu b^{-1}$
		Au+Au	62.4	$9 \mu b^{-1}$
05	2004/2005	Cu+Cu	200	$3 nb^{-1}$
		Cu+Cu	62.4	$0.19 nb^{-1}$
		Cu+Cu	22.5	$2.7 \mu b^{-1}$
		p+p	200	$3.8 pb^{-1}$
06	2006	p+p	200	$10.7 pb^{-1}$
		p+p	62.4	$0.1 pb^{-1}$
07	2007	Au+Au	200	$0.813 nb^{-1}$
08	2008	d+Au	200	$80 nb^{-1}$
		p+p	200	$5.2 pb^{-1}$
09	2009	p+p	500	$10 pb^{-1}$
		p+p	200	$16 pb^{-1}$
10	2010	Au+Au	200	$1.3 nb^{-1}$
		Au+Au	62.4	$0.11 nb^{-1}$
		Au+Au	39	$40 \mu b^{-1}$
		Au+Au	7.7	$0.26 \mu b^{-1}$

Table 2.1: summary of the RHIC operation. The integrated luminosity is recorded in PHENIX.

2.2 the PHENIX Detector

The PHENIX detector was optimized for precision measurement with particular focus on electromagnetic probe. The PHENIX have selective triggers, high rate capability, and multiple fast detector systems to track and identify particles emitting from collisions. The PHENIX detector consists of 2 central arms [78, 82, 84] which has pseudo-rapidity coverage of ± 3.5 and 180° azimuthal angle in total, 2 muon arms [85] which has pseudo-rapidity coverage of $\pm (1.2-2.4)$, and beam detectors [72] which is near the beam pipe.

2.2.1 Beam Beam Counters (BBC)

Beam Beam Counters(BBC) [73] are located on North and South side at 144.35 cm along beam pipe from the nominal collision point. The BBC covers pseudo-rapidity $3.1 < |\eta| < 3.9$ and full azimuthal angle $\Delta\phi = 2\pi$. Each of them consists of 64 \hat{C} erenkov detector elements, which consist quartz \hat{C} erenkov radiator and mesh-dynode type photo multiplier tube (PMT).

BBC have four major tasks, to trigger the Minimum Bias events, to measure the collision vertex, to obtain the collision timing and determine the centrality. In addition, the reaction plain is determined by hit pattern of BBC in heavy ion collisions. The collision vertex and timing are determined by the difference and average hit time to north and South counters;

$$\text{collision vertex} = \frac{(T_S - T_N)}{2} \times c \quad (2.1)$$

$$\text{collision time} = \frac{T_S + T_N - (2 \times L)/c}{2} \quad (2.2)$$

where T_N and T_S are the averaged hit time of incoming particles, c is the light velocity and L is the distance from nominal collision point ($z = 0$) to both BBC location, $L = 144.35$ cm.

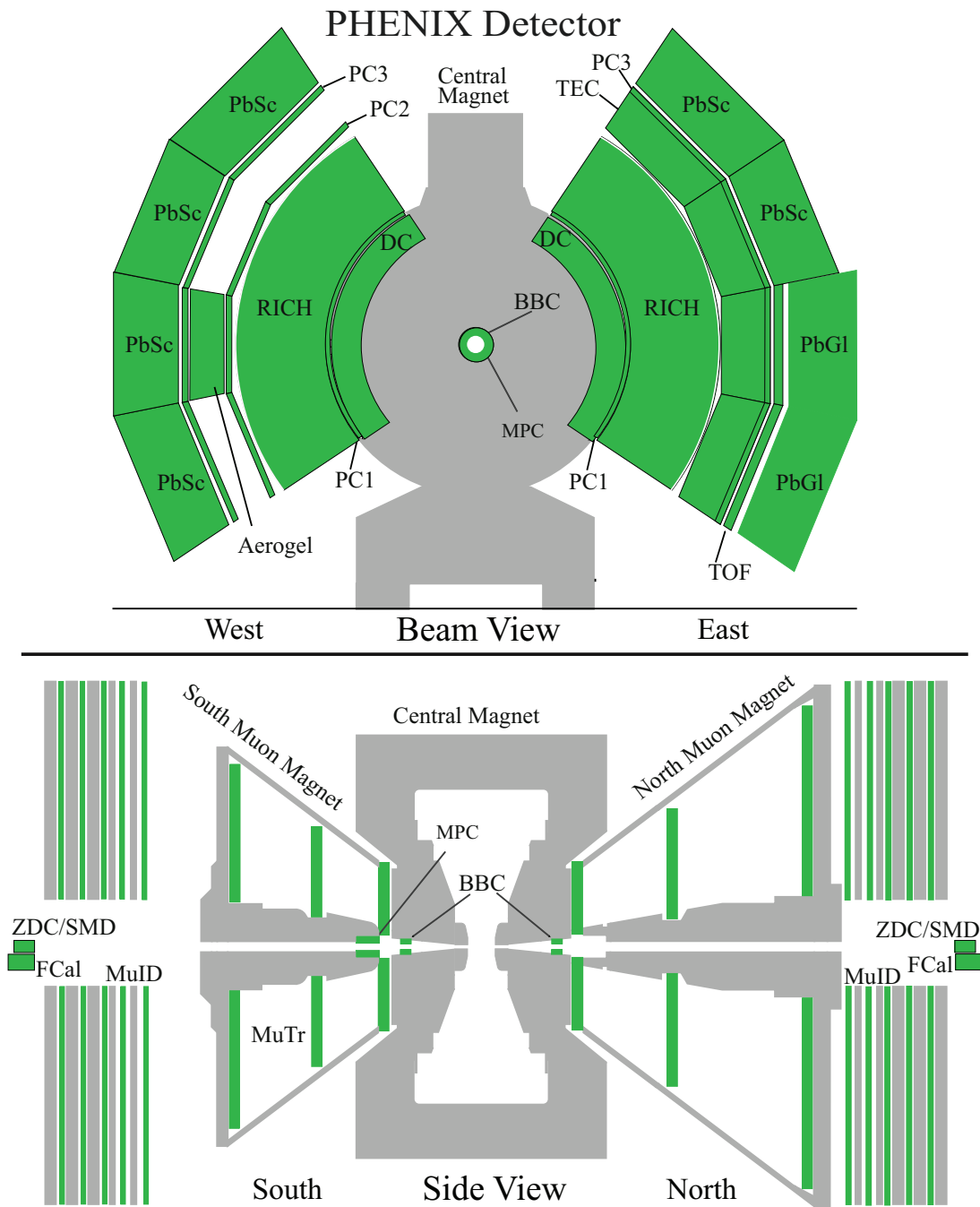


Figure 2.2: The PHENIX Detector configuration [88] The upper panel shows the beam view. Two central arms and central magnet can be seen. The bottom panel shows side view. Two muon arms and muon magnet can be seen.

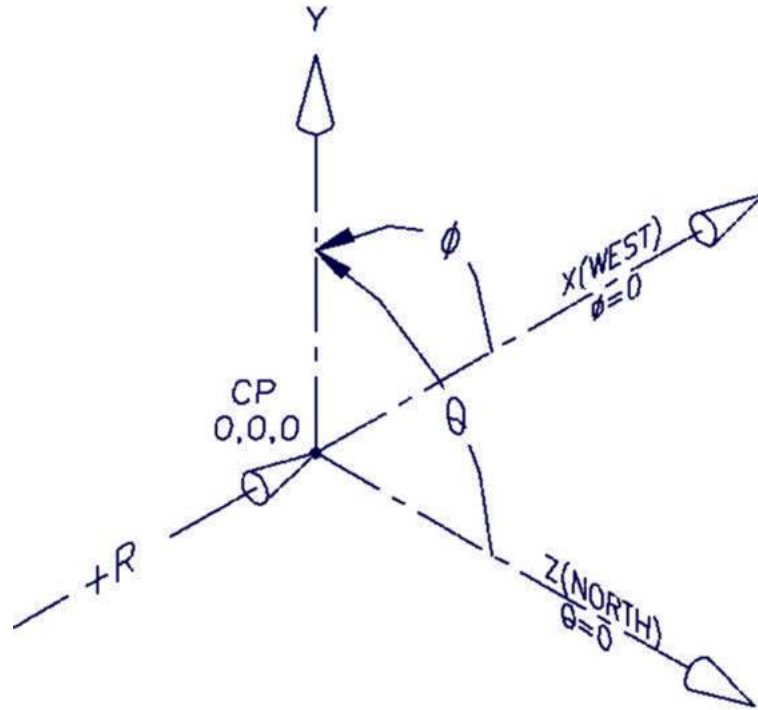


Figure 2.3: the PHENIX global coordinate system.

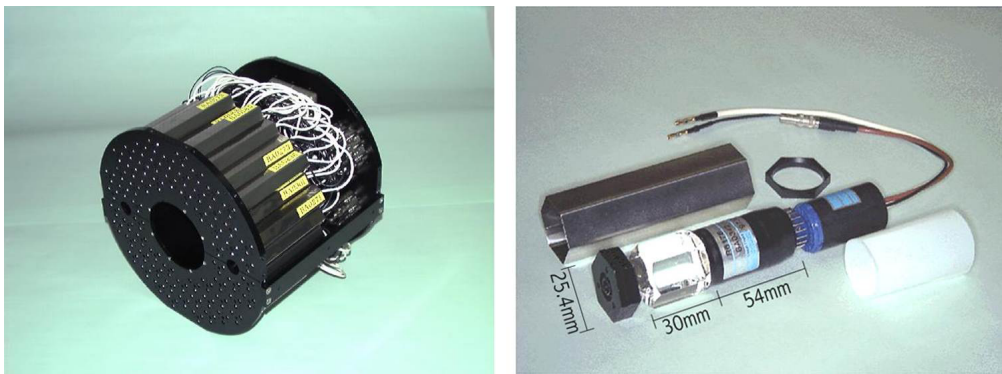


Figure 2.4: Left) BBC arrays consisting 64 elements. Right) One of the BBC elements consisting quartz Cherenkov radiator and mesh-dynode type PMT.

2.2.2 Zero Degree Counters (ZDC)

Zero Degree Calorimeters(ZDC) [74] are hadron calorimeter located at 18m North and South side along beam pipe from the collision point. Since the both north and south ZDC sit at just the upstream of the last bending magnet on the RHIC ring, most of charged particles are swept out from the acceptance. So, ZDC works as the minimum bias trigger counter and monitor the beam luminosity since ZDC measured neutrons from spectator part of heavy ion collision.

2.2.3 PHENIX tracking system

Magnet

The PHENIX has three magnet systems [75], one is the central magnet, others are north and south muon magnets. The central magnet provide a magnetic field around the collision point which is parallel to the beam. And the Central magnet consist of inner and outer coil, which can be optimized separately, together, or in opposition. During the run for this work, both inner and outer magnets are energized and integrated magnetic field is $1.15 T \cdot m$. the momentum of charged particles can be obtained by measuring the curvature of the track which is bended due to magnetic field.

Drift Chamber (DC)

The PHENIX Drift Chambers(DC) [77] are cylindrically shaped and located in the region from 2 to 2.4 m from the beam axis and 2 m along the beam axis. This places them in a residual magnet field with a maximum of 0.6 kG. Each DC measures charged particle trajectories to determine transverse momentum of each particles. The DC also participates in the pattern recognition at high particle track densities by providing position information that is used to link tracks thought the various PHENIX detectors. The good double track spatial resolution for the highest multiplicities at heavy ion collisions is required and the single wire two track separation batter than 1.5 mm.

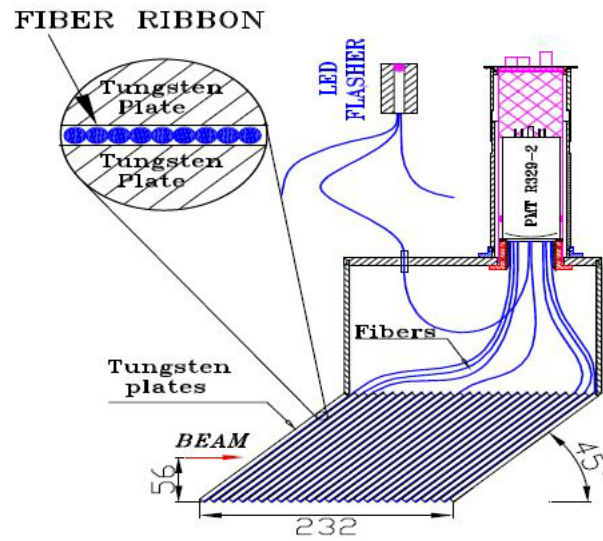
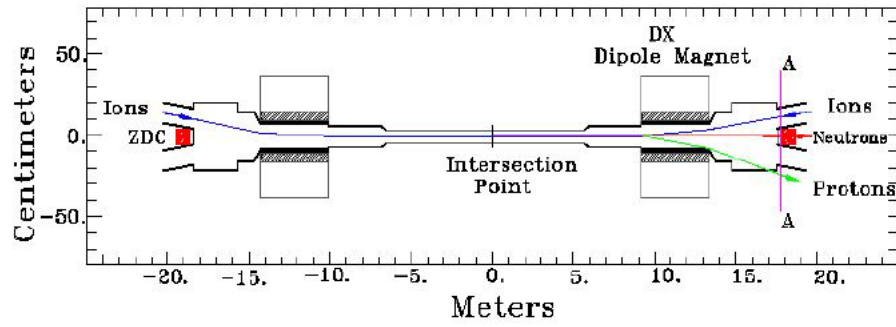
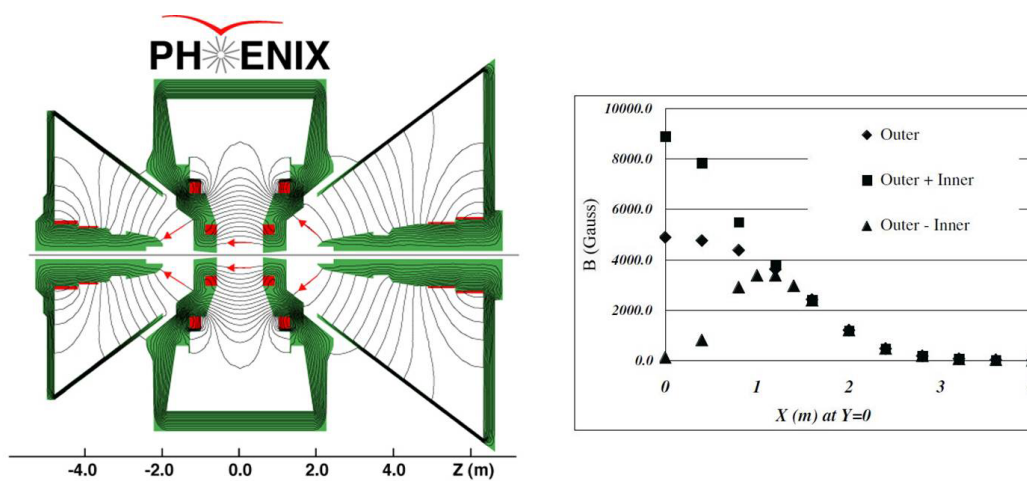


Figure 2.5: schematic view of the ZDC location including deflection of protons and charged fragments [74]



Magnetic field lines for the two Central Magnet coils in combined (++) mode

Figure 2.6: Left) overview of the PHENIX Magnets. The line shows the contour of the magnetic. Right) total magnetic field strength as a function of R at the $\theta=0$ symmetry plane of the Central Magnet for +(outer), ++(Outer+Inner), and +-(Outer-Inner) configuration .

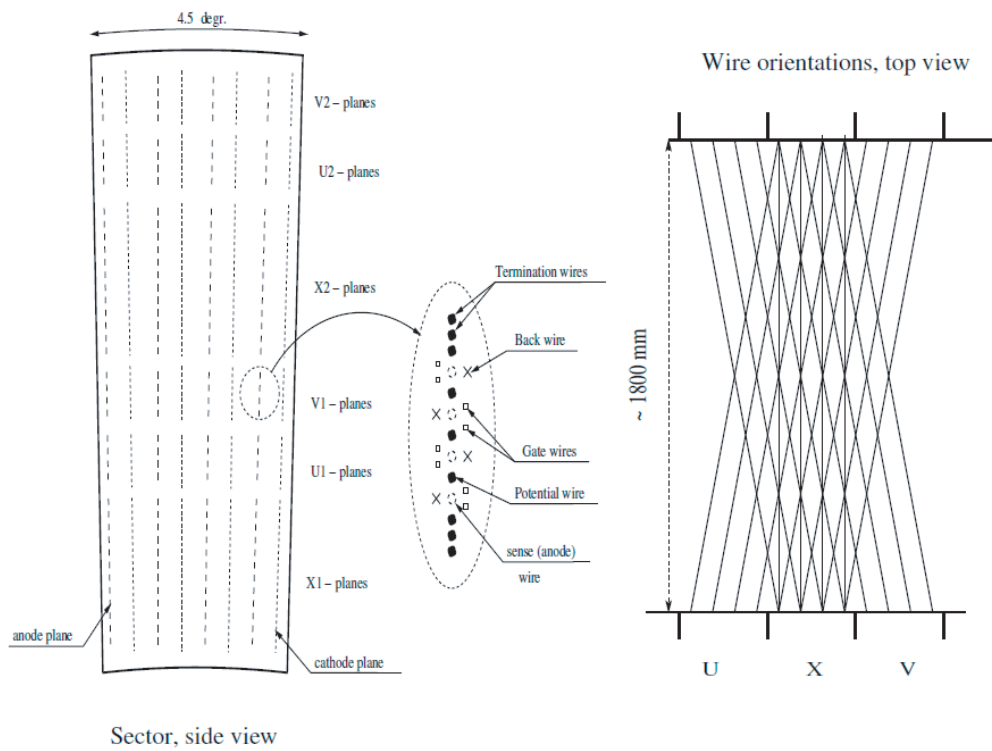


Figure 2.7: The layout of wire position of DC. The X1 and X2 wire cells runs in parallel to the beam to perform precise track measurements in $r-\phi$. U1, V1, U2, V2 wires have stereo angle of about 6° relative to the X wires and measure the z coordination of track [78].

Pad Chamber (PC)

The PHENIX Pad Chambers(PC) [76] are multiwire proportional chambers that form three separate layers. Each detectors consists of a single plane of wire inside a gas volume bounded by two cathode plane. One cathode is finely segmented into an array of pixels. The charge induced on a number of pixels when a charged particle starts an avalanche on an anode wire, is read out thorough specially designed read out electronics. The PC system determines space points along the straight line particle trajectories outside the magnetic field. Fig.2.3 shows position of PCs relative to the other detectors. The innermost pad chamber called PC1 is essential for determining the three-dimensional momentum vector by providing the z coordinate at the exit of the DC.

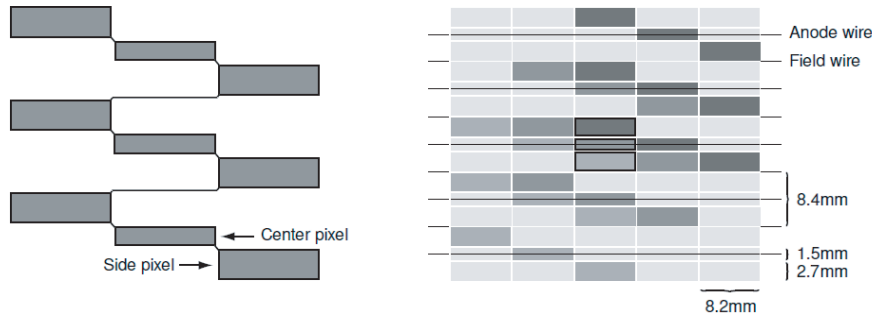


Figure 2.8: the pad and pixel geometry(left), A cell defined by three pixels is at the center of the right picture [78].

Track reconstruction

Charged particles emitted from collision vertex pass through the magnetic field and bend along with a plane perpendicular to beam pipe until reaching the DC. These particles reaching DC goes away in straight lines, since there is almost zero strength of the magnetic field at the outside of DC. Fig. 2.9 shows definition of track parameters for describing a charged particle trajectory though the magnetic field in PHENIX up to PC1 [78, 79].

The parameters measured with DC and PC1 and used to reconstruct the particle trajectory are defied as follows:

- α : The angle between the projection of trajectory in the x - y plane and the radial direction, at the interaction point of trajectory with the circle of reference radius $R_{DC} = 2.2$ m.

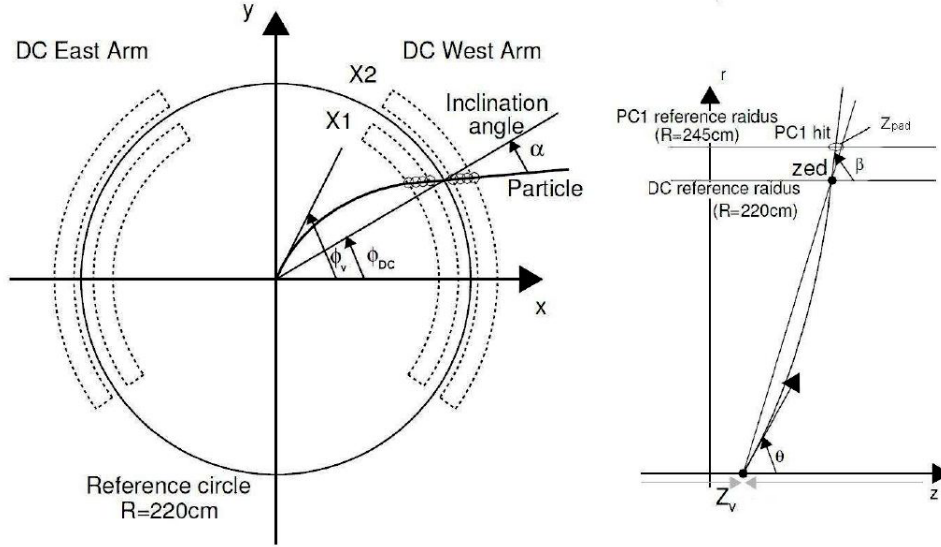


Figure 2.9: Illustration of the track reconstruction in the PHENIX up to PC1 on x - y plane and r - z plane.

- ϕ_{DC} : The azimuthal angle of the interaction point of the trajectory with the circle of radius R_{DC} .
- z_{pad} : The z coordinate of the interaction point of the trajectory with PC1 surface radius $R_{PC1} = 2.45$ m.
- β : The angle between the projection of trajectory in the r - z plane and the z -axis.
- ϕ_v : The initial azimuthal angle of the particle trajectory
- θ : The angle between the initial direction of particle trajectory and z -axis.

The track finding algorithm assumes that the all tracks originated at the collision vertex. The collision vertex is assumed to be $(0,0)$ in (x, y) plane and z position is determined by the timing information of BBC as described in Sec.2.2.1 The track reconstruction within DC is performed using a Hough transform technique [80]. In this technique, the DC hits in X1 and X2 are mapped for all possible X1-X2 hits combinations into a feature space defined by the azimuthal angle ϕ_{DC} and the track bending angle α . The basic assumption is that tracks are straight lines within the DC. In the case of that

all hit pairs of a given track will have the same ϕ and α , then result have maximum in the mapped space of ϕ and α . The reconstructed tracks are then associated with X1 and X2 hits. Once a track is found in ϕ and α plane, the z -coordinate of the track is determined using the Hough Transform with the associated PC1 cluster and the stereo U and V wire informations of the DC.

The momentum, p of the charged particle is determined using the θ and α measured in DC and PC1. The transverse momentum, p_T (GeV/ c) and the α -angle (mrad) have the following approximate relation:

$$\alpha \approx \frac{K}{p_T}, \quad (2.3)$$

where $K \approx 0.10$ (rad GeV/ c) is the effective field integral between the collision vertex and the DC, expressed as:

$$K = \frac{e}{R} \int l B dl. \quad (2.4)$$

Here, e is the elementary charge in the hybrid unit ($e = 0.2998$ GeV/ c T $^{-1}$ m $^{-1}$) and R is the DC reference radius.

The resolution of momentum depends on the intrinsic angular resolution of the DC and the contribution of multiple scattering. The momentum resolution is finally determined to be $\delta p/p = 0.7\% \oplus 1.0\% \times p$ (GeV/ c) [81]

The quality of track reconstructed by track finding algorithm with DC and PC is defined using the hit information of the X and the stereo U and V wires and the associated PC1 cluster. This *Quality* is defined as a binary pattern of 6 bit valuable as follow :

$$Quality = A \times 2^0 + B \times 2^1 + C \times 2^2 + D \times 2^3 + E \times 2^4 + F \times 2^5, \quad (2.5)$$

where A, B, C, D, E, F are quality bits defined as follows:

- A=1: X1-wire used
- B=1: X2-wire used
- C=1: UV-wire found
- D=1: UV-wire unique
- E=1: PC1 found
- F=1: PC1 unique

If the track is reconstructed by both X1 and X2 sections of DC and is uniquely associated with hits in U or V stereo wires, the value of *quality* is 63 (in case a unique PC1 hit is found) or 31 (in case the PC1 hit is found but ambiguous). In this analysis, the tracks of quality of 63 or 31 are used.

		ABCDEF	quality		
PC1 found/unique	no UV	1100xx	49	50	51
PC1 found/unique	UV found/unique	1111xx	61	62	63
PC1 found/ambiguous	no UV	0100xx	17	18	19
PC1 found/ambiguous	UV found	0101xx	21	22	23
PC1 found/ambiguous	UV found/unique	0111xx	29	30	31

Table 2.2: Summary of the track quality

2.2.4 Ring Image Cherenkov Counters (RICH)

The Ring Image Cherenkov Counters(RICH) [83] occupies the radial region between 2.575 and 4.1 m from the beam line. Each of the detectors in the east and west central arms has a volume of 40cm². the minimum thickness of the radiator gas, which is CO₂, is 87 cm, the maximum is about 150 cm. The RICH provides e/π discrimination below the π Cherenkov threshold, which is set at 4.65 GeV/c. The Cherenkov photon produced in the radiator gas are reflected on the mirror and are detected by the photon multiplier tubes (PMTs). The average size of the Cherenkov ring is 8 cm and average number of the Cherenkov photon produced by electron is 10.8 on the plane where the PMTs are sitting. Fig.rich show the cut through view of RICH detector.

2.2.5 Electro Magnetic Calorimeter (EMC)

The Electro Magnetic Calorimeter (EMCal) is designed primarily to measure the energies and spatial position of photon and electrons. It also plays a major role of in particle identification and is an important part of the PHENIX trigger system. The EMCal system can trigger on rare events with high transverse momentum photons and electrons. The EMCal system consists of a total of 24768 individual detector modules divided between the Pb-Scintillator calorimeter (PbSc), which provides 6 sectors of central arm and the Pb-Glass calorimeter (PbGl) comprised of 2 sectors.

The PbSc is a sampling calorimeter made of alternating tile of Pb and scintillator consisting of 15552 individual towers and covering an area of approximately 48 m². The basic block is a module consisting of 4 towers, which are optically isolated, and are read out individually. The tower has 5.52×5.25 cm² cross section and 3.75 cm in length. Figure 2.11 show the interior view of the module. A super-module is composed of 12×12 towers and a sector is composed of 18(12×12) super-modules.

The PbGl is a Cherenkov type calorimeter. A lead glass has 4.0×4.0

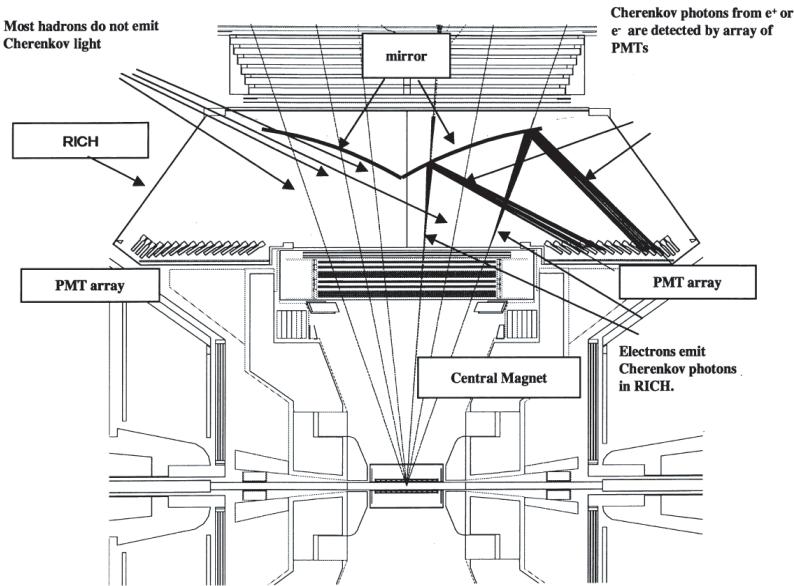


Figure 2.10: A cut through view of RICH detector

parameter	PbSc	PbGl
Radiation length (X_0)	2.1 cm	2.8 cm
Moliere radius	~ 3.0 cm	3.7 cm
Nuclear interaction length (λ_I)	44 cm	38 cm
Total η coverage	0.7	0.7
Total ϕ coverage	$\pi/2 + \pi/4$	$\pi/4$
Number of towers in one sector	72×36	96×48
Total depth	37.5 cm ($18X_0, 0.85\lambda_I$)	40 cm ($14X_0, 1.05\lambda_I$)

Table 2.3: Summary of parameters of two type of PHENIX EMCal

cm^2 cross section and 40 cm length. Figure 2.12 shows the interior view of one super-module, composed by 4×6 towers. A sector is composed of 192(12×12) super-modules.

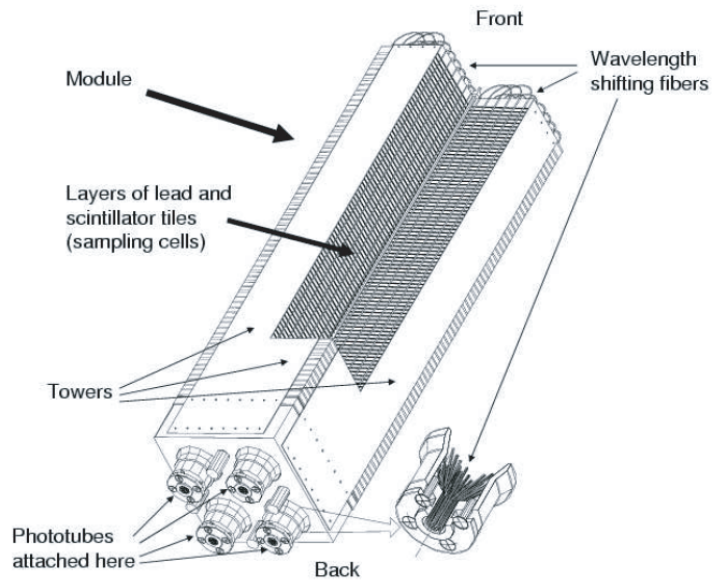


Figure 2.11: Interior view of a lead-scintillator calorimeter module

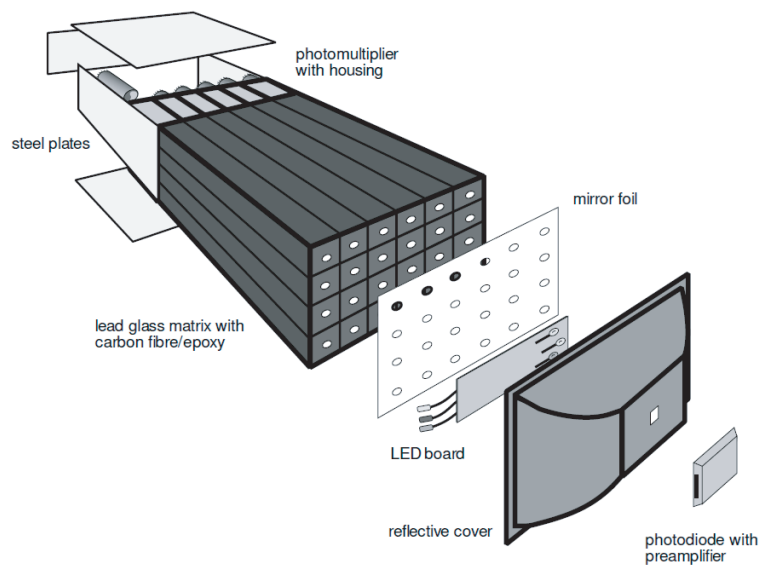


Figure 2.12: Exploded view of a lead-glass detector supermodule

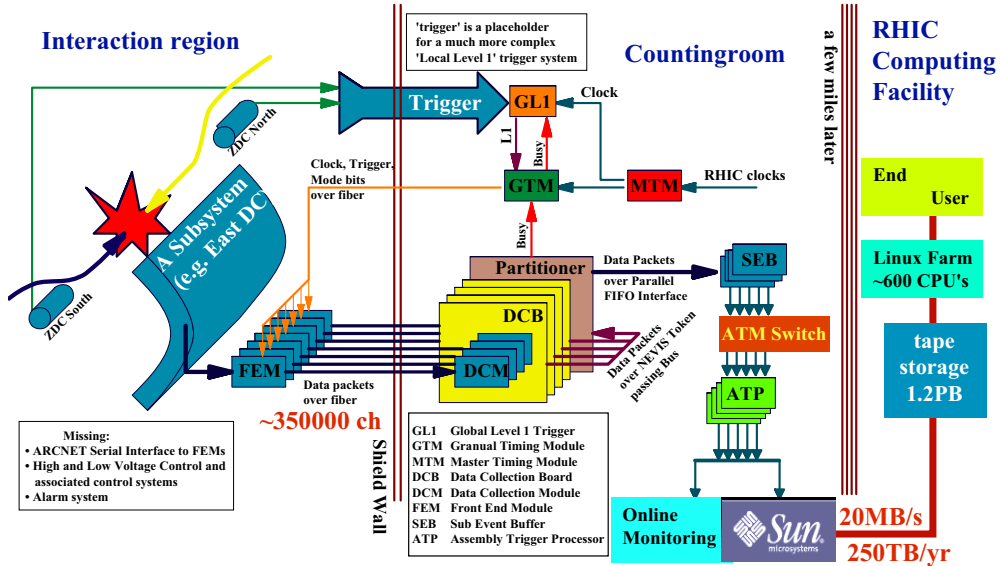
2.3 Data Acquisition system (DAQ)

PHENIX is designed to make measurements on a variety of collision system from p+p to Au+Au. The occupancy in the detector varies from a few tracks in p+p interaction to approximately 10% of all detector channels in central Au+Au interactions. The interaction rate at design luminosity varies from a few kHz for Au+Au central collisions to approximately 500 kHz for minimum bias p+p collisions. The PHENIX DAQ system was designed to seamlessly accommodate improvements in the design luminosity. This was accomplished through the pipelined and deadtimeless features to the detector front ends and the ability to accommodate higher-level triggers.

In PHENIX it is necessary to measure low-mass lepton pair and low p_T particles in a high-background environment. In order to preserve the high interaction-rate capability of PHENIX a flexible system that permits tagging of events was constructed. The On-Line system has two levels of triggering denoted of LVL1 and LVL2. The LVL1 trigger is fully pipelined, therefore the On-Line system is free of deadtime through LVL1. Buffering is provided that is sufficient to handle fluctuations in the event rate so that deadtime is reduced to less than 5% for full RHIC luminosity. The LVL1 trigger and lower levels of the readout are clock-driven by bunch-crossing signals from the 9.4 MHz RHIC clock. The higher levels of readout and the LVL2 trigger are data-driven where the results of triggering and data processing propagate to the next higher level only after processing of a given event is completed.

The general schematic for the PHENIX On-Line system is shown in Fig. 2.13. Signals from the various PHENIX subsystems are processed by Front End Electronics (FEE) that convert detector signals into digital event fragments. This involves analog signal processing with amplification and shaping to extract the optimum time and/or amplitude information, development of trigger input data and buffering to allow time for data processing by the LVL1 trigger and digitization. This is carried out for all detector elements at every beam crossing synchronously with the RHIC beam clock. The timing signal is a harmonic of the RHIC beam clock and is distributed to the FEM's by the PHENIX Master Timing System (MTS). The LVL1 trigger provides a fast filter for discarding empty beam crossings and uninteresting events before the data is fully digitized. It operates in a synchronous pipelined mode, generates a decision every 106 ns and has an adjustable latency of some 40 beam crossings.

Once an event is accepted the data fragments from the FEM's and primitives from the LVL1 trigger move in parallel to the Data Collection Modules (DCM). The PHENIX architecture was designed so that all detector-specific electronics end with the FEM's, so that there is a single set of DCM's that



communicate with the rest of the DAQ system. The only connection between the Interaction Region (IR) where the FEM's are located and the Counting House (CH) where the DCM's are located is by fiber-optic cable. The DCM's perform zero suppression, error checking and data reformatting. Many parallel data streams from the DCM's are sent to the Event Builder (EvB). The EvB performs the final stage of event assembly and provides an environment for the LVL2 trigger to operate. In order to study the rare events for which PHENIX was designed, it is necessary to further reduce the number of accepted events by at least a factor of six. This selection is carried out by the LVL2 triggers while the events are being assembled in the Assembly and Trigger Processors (ATP) in the EvB. The EvB then sends the accepted events to the PHENIX On-line Control System (ONCS) for logging and monitoring. The logged data, which is named as PHENIX Raw Data File (PRDF), are sent to RHIC Computing Facility (RCF) for sinking on the tape in High Performance Storage System (HPSS). The data in the HPSS are analyzed and converted into an intermediated data format in the linux computer at RCF and Computing Center in Japan (CCJ).

2.4 Event trigger

The PHENIX has had various kinds of the Level 1 triggers corresponding to aim of physics. In this section, two type triggers of BBCLL1 trigger as Minimum Bias trigger and EMCal RICH level 1 are introduced.

Minimum Bias Trigger

The Minimum Bias trigger in PHENIX is generated by BBCLL1 based on hit information of BBCs. It requires the coincidence of BBC north and south with at least one hit for each side and reconstructed collision vertex is within 30cm of nominal interaction point.

$$\text{Min.Bias} \equiv (\text{BBCN} \geq 1) \ \&\& \ (\text{BBCS} \geq 1) \ \&\& \ (|\text{vertex}| < 38\text{cm}) \quad (2.6)$$

Since the low event multiplicity in $p+p$ collisions for the rapidity coverage of BBCs, the Minimum Bias trigger accepts only part of the total cross section. This efficiency of minimum bias trigger is estimated to be $54.5 \pm 5\%$ of total inelastic cross section of $\sigma_{inel}^{pp} = 42 \pm 3\text{mb}$ for $p+p$ collisions in $\sqrt{s} = 200\text{GeV}$. Namely, the Minimum Bias trigger absolute cross section is $23\text{mb} \pm 9.7\%$. The fraction of events with particles in the central arm acceptance is $\epsilon_{bias} = 79 \pm 2\%$ with p_T and physics process independent, which determined from the ratio of data collected with and without required the Minimum Bias trigger. Therefore, the measured particles yield is divided by $0.79/0.545$ to correct the fraction of the event missed by the Minimum Bias trigger in $p+p$ collisions.

EMCal and RICH Trigger

The other is the EMCal and RHIC trigger(ERT) designed to enhance the electron, positron, pair of electron and positron, high p_T π_0 . The ERT trigger is crucial for e^+e^- measurement since the events including e^+e^- pairs are rare. The ERT trigger requires a minimum energy deposit of 400MeV in 2×2 EMCal towers matched to a hit in the RICH and coincidence with the Minimum Bias trigger. The schematic view of ERT trigger is shown in Figure 2.15.

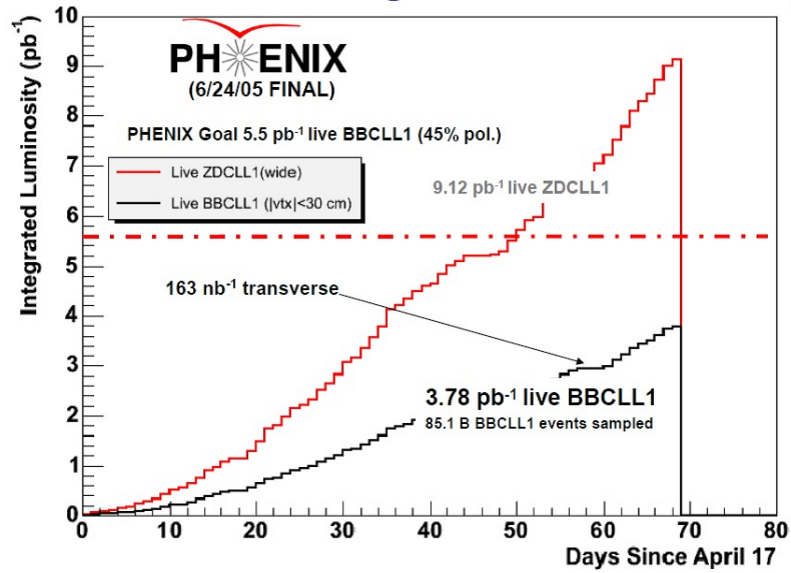


Figure 2.14: Integrated luminosity as a function of date for 200GeV $p+p$ collisions collected by PHENIX in year2004/2005.

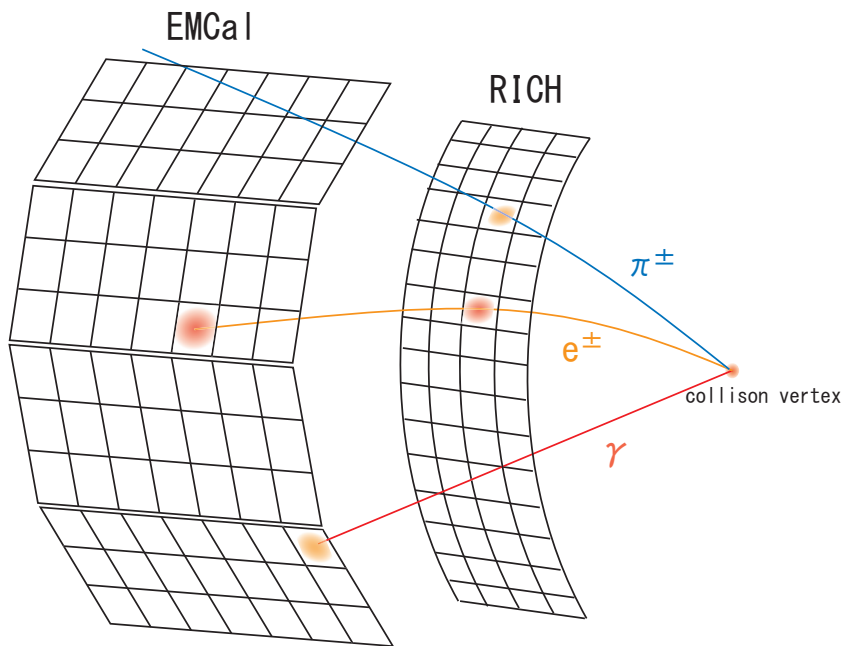


Figure 2.15: schematic view of EMCAL RICH level1 Trigger: Both the super-Module of EMCAL and RICH are fired for e^+, e^- . Only the EMCAL is fired for photon, while only the RICH is fired for high p_T pion. We are able to effectively collect the events including e^+e^- pair.

Chapter 3

Analysis

3.1 Outline of Analysis

In this section, the outline of the analysis is introduced. First, the run and trigger selection is explained in Section 3.2. The methods of track selection to extract electrons from charged hadrons background are described in Section 3.3. By using extracted electrons, the invariant mass of electron and positron are kinematically reconstructed. The procedure of invariant mass reconstruction are introduced in Section 3.4. The background component to invariant mass distribution is explained in Section 3.5. The extraction of raw yield for ω and ϕ is described in Section 3.6. The acceptance, electron ID efficiency and trigger efficiency calculated by using Monte-Carlo simulation are explained in Section 3.7. Finally, the ω and ϕ cross section and systematic uncertainties are presented in Section 3.8.

3.2 Run and Trigger Selection

In proton-proton collisions in year 2004 to 2005 (RUN05), the PHENIX collected 3.8 pb^{-1} as total integrated luminosities which contains 262TByte data as a PRDF(PHENIX Raw Data File) format. 16587 DST(Data Summary Tape) files were made from PRDF. The run number which correspond to $p + p$ collisions in RUN05 is from run168314 to run179846. Run171595 to run172080 are the converter runs where an additional converter (a thin brass sheet of 1.67% X_0) was installed around the beam pipe. Run176417 to run176613 are the higher energy runs at $\sqrt{s} = 410 \text{ GeV}$. The normal runs (non-converter runs and $\sqrt{s} = 200 \text{ GeV}$ runs) are analyzed in this work.

The vertex distribution for Minimum Bias triggered events reconstructed by timing information of BBCs is shown in Fig. 3.1. Fig. 3.2 shows the

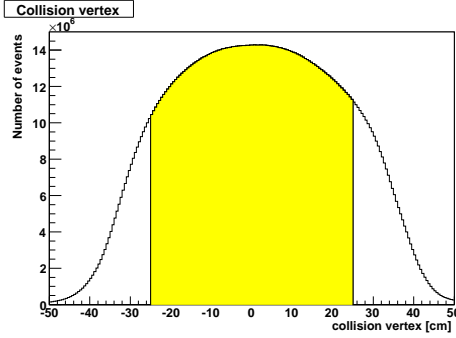


Figure 3.1: Collision vertex distribution. The events in yellow band range are selected for this analysis.

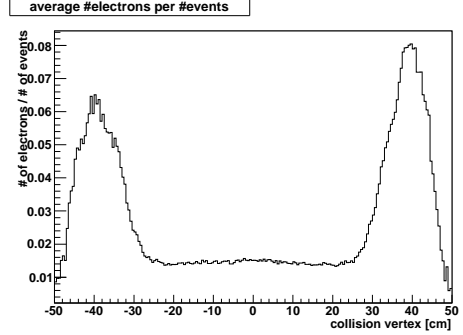


Figure 3.2: number of electrons per events as a function of collision vertex.

average number of electrons per event as a function of the collision vertex. the events with the collision vertex out of ± 25 cm contains the large amounts of conversion electrons generated in detector materials. Therefore, the events with the collision vertex within ± 25 cm of nominal interaction point is selected.

This analysis have done using data samples collected by the Minimum bias trigger(and the ERT trigger that introduced in Section 2.4, with the energy threshold setting of 400MeV on the 2x2 EMCal tower. Fig.3.3 shows the number of electrons per Minimum Bias triggered event as function of run number. If electron yield is less than 2×10^{-4} , these run were rejected from our analysis since the detectors condition were not stable in these run. The yield is very stable until run 178937. The electron yield drops after run 178937 since two of RICH data packets for ERT trigger were disable. The efficiency for ERT triggered electrons in run 169645-169667, 169719-169884, 175815-175831, 175945-175978 were not consistent with one of the nominal runs due to the wrong setting of EMCal High Voltage. Number of events including these run periods were about 2 % of total luminosity, which were small and removed in this analysis.

Fig.2.4 shows the ratio of the number of Minimum Bias triggered event in the ERT triggered sample and the number of ERT triggered event in the Minimum Bias triggered sample. If there is no file segment lost during data reconstruction, this ratio is equal to unity. Runs with the ratio > 2 or < 0.5 were removed from this analysis.

In PHENIX, the Minimum Bias event in $p + p$ collisions were not fully recorded due to the limited bandwidth of data acquisition as compared to trigger rate. A fraction between recorded and all minimum bias events follows

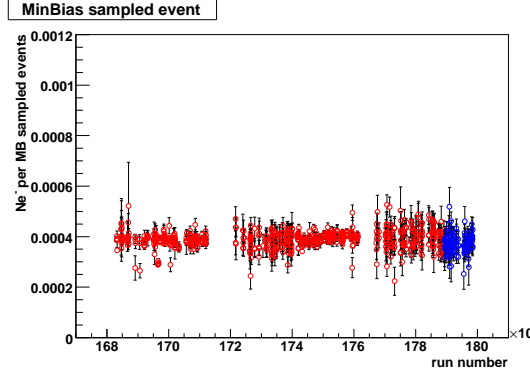


Figure 3.3: Number of electron in $0.3 < p_T < 4.0 \text{ GeV}/c$ per sampled Minimum Bias triggered event as a function of run number.

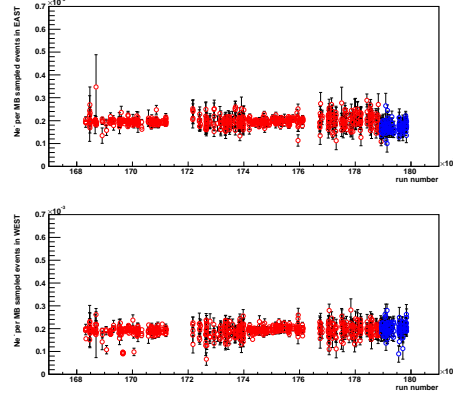


Figure 3.4: Number of electron detected in EAST (top) and WEST (bottom) arms per sampled Minimum Bias triggered event.

the scale down factor, which was specified at the beginning of each run for each triggers and depends on the beam conditions. After run selection, the total number of samples Minimum Bias events corresponding to the ERT trigger set were calculated as follow:

$$\begin{aligned}
 N_{MB}^{sampled} &= \sum_{run} N_{MB} \times f_{Scale-Down-Factor} \\
 &= 55831.6M
 \end{aligned}
 \tag{3.1}$$

where N_{MB} is the number of events recorded with the Minimum Bias trigger and $f_{scale-down-factor}$ is scaled down factor for each run.

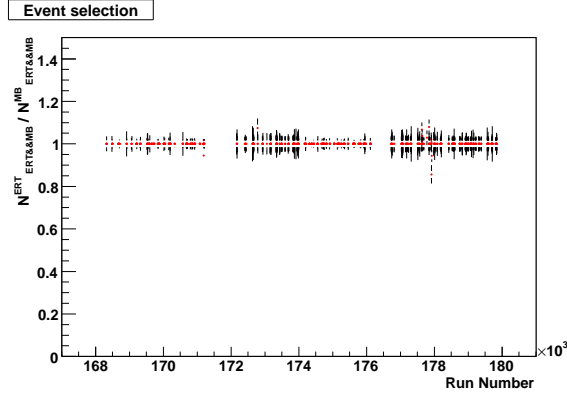


Figure 3.5: $N_{ERT\&\&MB}^{ERT} / N_{ERT\&\&MB}^{MB}$ as a function of run number. This ratio should be unity when there is no file segment lost at data reconstruction.

3.3 Track Selection and electron identification (eID)

In this section, the methods of electron identification from charged hadron background are introduced. The fraction of produced electrons in all of charged hadron, mainly pions, is less than 1%. Electrons are identified with RICH and EMCal.

3.3.1 Number of Hit PMT (n0)

The number of fired RICH PMTs in a ring with inner radius of 3.4 and outer radius of 8.4 cm around the projection point of the track onto the PMT plane of RICH. The expected radius of a Cherenkov ring emitted by an electron is 5.9 cm, the width of ± 2.5 cm around it corresponds to the position resolution of the PMT hits.

3.3.2 RHIC match

The absolute displacement of the projection ring center to the measured ring center, determined from RICH PMTs in the ring area between 3.4 and 8.4 cm. The measured ring center is the weighted average of the hit PMT position.

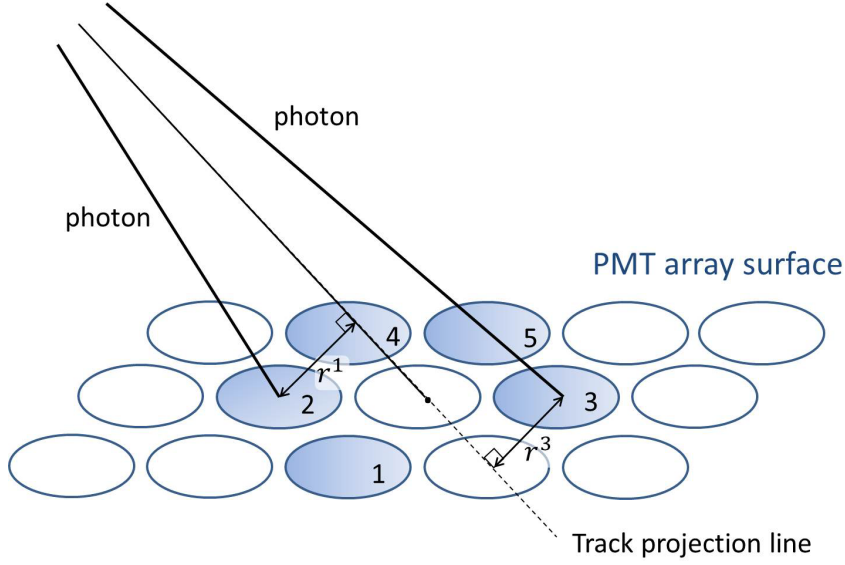


Figure 3.6: Schematic description of the definitions of variable which characterized the RICH ring. The five fit PMTs are shown as an example.

3.3.3 EMC match

EMCal match ($\Delta\phi$)

Distance in ϕ direction between the position of the associated EMCal cluster and the projection on the track onto the EMCal. The distance is normalized by its standard deviation $\sigma_{\Delta\phi}$.

$$\Delta\phi = \frac{\phi_{projection} - \phi_{hit}}{\sigma(\Delta\phi)} \quad (3.2)$$

EMCal match (Δz)

Distance in z direction between the position of the associated EMCal cluster and the projection on the track onto the EMCal. The distance is normalized by its standard deviation $\sigma_{\Delta z}$.

$$\Delta z = \frac{z_{projection} - z_{hit}}{\sigma(\Delta z)} \quad (3.3)$$

The mean and sigma of variables $\sigma_{\Delta\phi}$ and $\sigma_{\Delta z}$ should be zero and one, respectively.

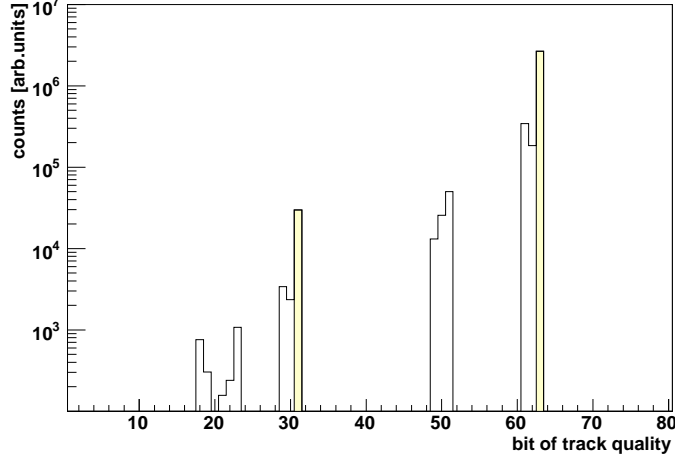
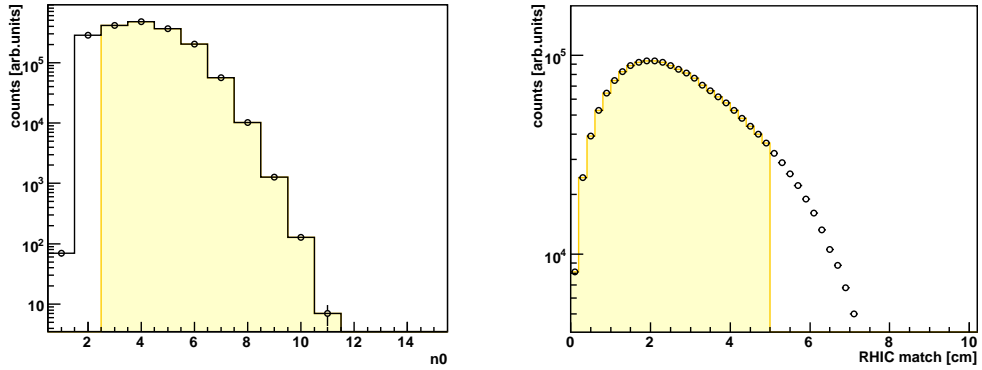


Figure 3.7: Track quality distribution.

Figure 3.8: (distribution of n_0 (left) and *RICH* matching(right)).

3.3.4 deposition energy over momentum ratio (*dep*)

The relative deviation of $E/p - 1$, where E is the energy measured by EMCal, p is the momentum of the track.

$$dep = \frac{E/p - 1}{\sigma(E/p)} \quad (3.4)$$

Figure 3.10 shows the E/p distribution for all charged tracks(black) and for electron candidates(red) which fulfill all the eID cuts listed in Table 3.1 except the *dep*. The electron mass is light compared to its momentum $p > 200 MeV/c$. In case of electron, deposition Energy into EMCal(E) over momentum(p) ratio will be $E/p \simeq 1$, since its all energy is deposited into the

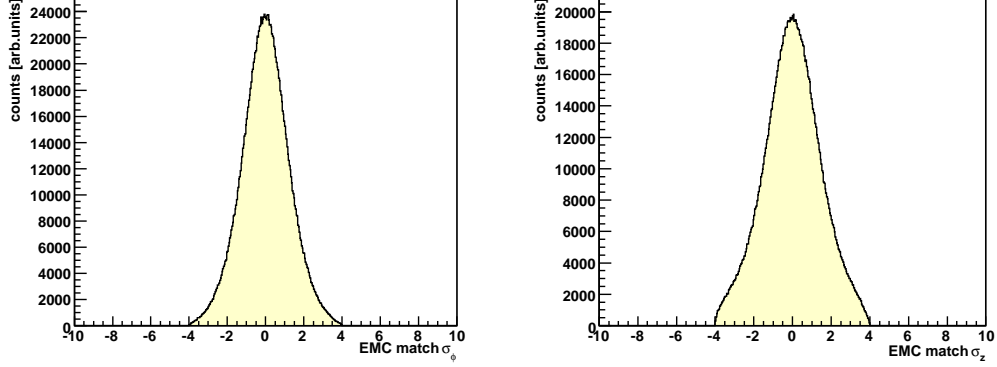


Figure 3.9: distribution of *EMCAL matching* for σ_ϕ (left) and σ_z (right)

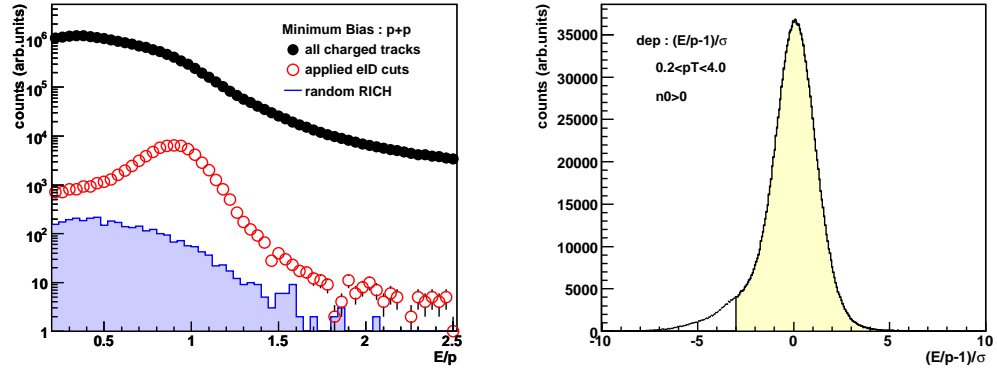


Figure 3.10: (left) E/p distribution in minimum bias event for all charged tracks, for electron candidates and for randomly associated hadrons. (right) dep distribution applying $n_0 > 0$.

EMCAL due to electromagnetic shower. In contrast, the hadrons only deposit fraction of their energy into EMCAL as the result of ionization loss. Therefore, It doesn't leads the peak structure in E/p distribution. While the distribution of all charged tracks are not seen clear electron peak, the clear peak at $E/p \simeq 1$ is seen when applying eID cuts. Signal-to-background ratio is improved by requiring the eID cuts.

3.4 Fiducial cut

For selecting stable detector condition through the analyzing period, unstable area of DC and EMCAL were removed. The relation between the board number

eID cuts	
Track quality	$31 \cup 63$
Number of Hit PMT (n0)	> 2
RHIC match	< 5 cm
EMC match $\sqrt{\sigma_{\Delta\phi}^2 + \sigma_{\Delta z}^2}$	$< 4 \sigma$
deposition energy over momentum ratio (dep)	$> -3 \sigma$

Table 3.1: Electron ID cuts used in this analysis.

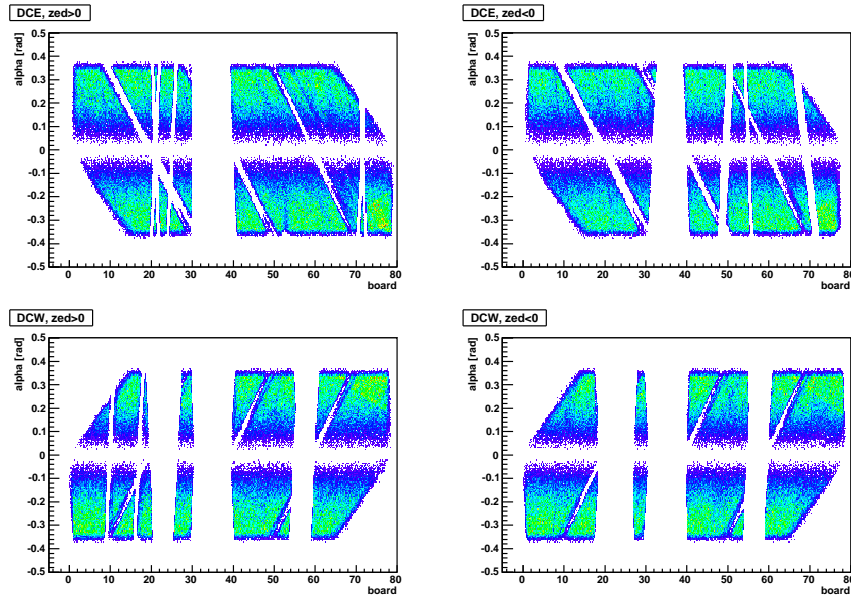


Figure 3.11: Alpha vs board distribution for both sides of the DC East and West after applying the fiducial cuts

in the DC and the azimuthal angle ϕ is as follows:

$$(\text{East arm})_{\text{board}} = (3.72402 - \phi + 0.008047 \times \cos(\phi + 0.87851))/0.01963496$$

$$(\text{West arm})_{\text{board}} = (0.573231 + \phi - 0.0046 \times \cos(\phi + 0.05721))/0.01963496$$

Using the hardware related coordinates as *board* number can easily identify the malfunction part of detector. Fig.3.11 shows track bending angle α vs *board* distribution for track reconstructed in the East and West side DC after applied the fiducial cuts. Fig.3.12 shows occupancies of EMCAL sectors removed dead and warm towers after applied the fiducial cuts.

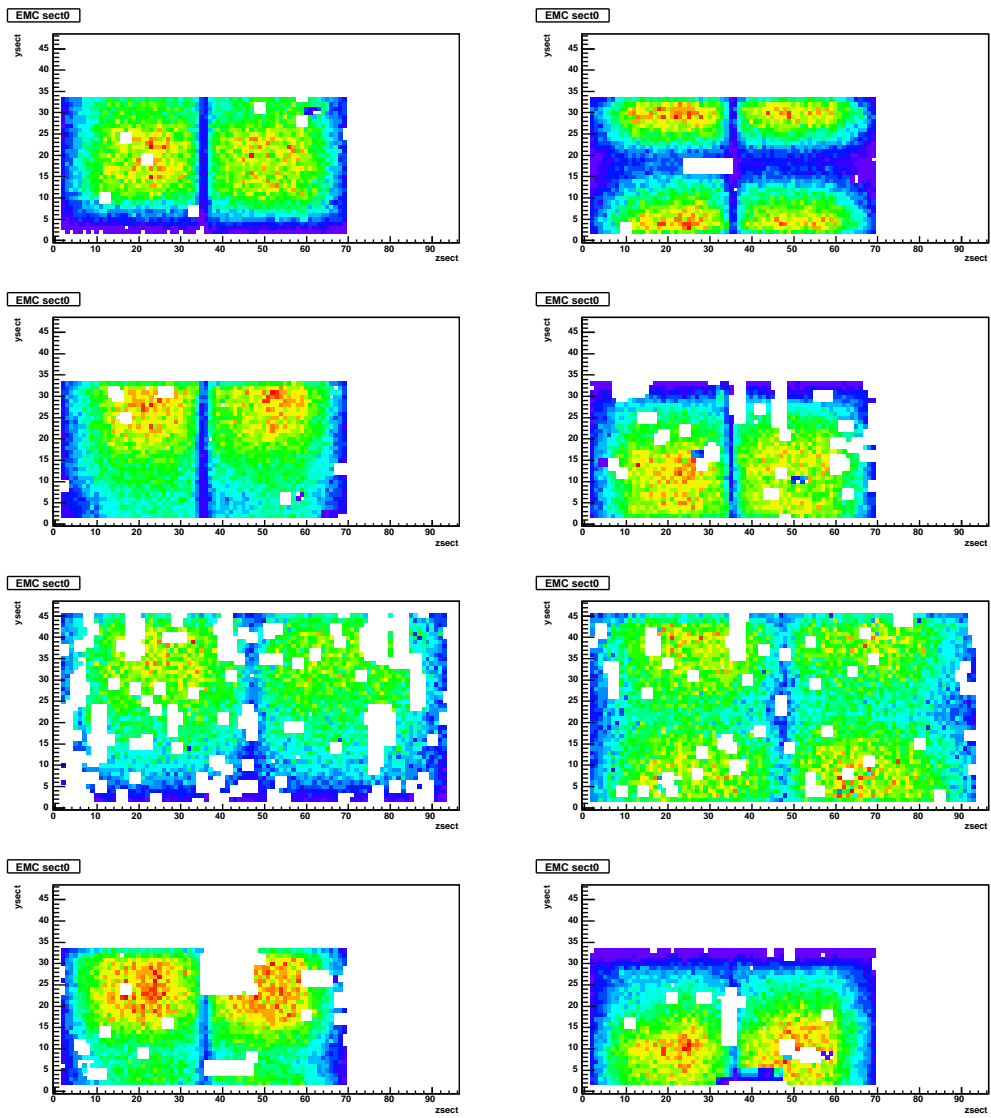


Figure 3.12: Occupancy of EMCal sectors after applying the fiducial cuts

3.5 Pair reconstruction

The invariant mass of electron and positron pairs are calculated from measured energy and momentum of electron and positron itself.

$$M_{ee} = \sqrt{(E_{e^+} + E_{e^-})^2 - (\vec{p}_{e^+} + \vec{p}_{e^-})^2} \quad (3.5)$$

where E is the energy of the particle, \vec{p} is particle momentum,

$$(E_{e^+} + E_{e^-})^2 = (\sqrt{m_{e^+}^2 + p_{e^+}^2} + \sqrt{m_{e^-}^2 + p_{e^-}^2})^2 \quad (3.6)$$

and,

$$(\vec{p}_{e^+} + \vec{p}_{e^-})^2 = (p_{e^+x} + p_{e^-x})^2 + (p_{e^+y} + p_{e^-y})^2 + (p_{e^+z} + p_{e^-z})^2. \quad (3.7)$$

p_x, p_y, p_z is written as following,

$$\begin{aligned} p_x &= p \times \sin \theta \cos \phi \\ p_y &= p \times \sin \theta \sin \phi \\ p_z &= p \times \cos \theta \end{aligned}$$

where θ is the polar angle measured from the beam axis and ϕ is the azimuthal angle. The invariant mass distribution are derived by combination all identified e^+e^- pairs.

3.6 Background subtraction

The obtained invariant mass spectra contains all identified electron and positron pairs. To improve signal/background ratio of ω and ϕ mesons, we need to understand source of background and remove it.

1. The background contributed from following is possible to identify in pair-by-pair.
 - (a) Fake electron pair
 - (b) photon conversion pair
2. On the other hand, the following background components are impossible to identified in pair-by-pair. but we are able to subtract statistically.
 - (a) uncorrelated combinatorial background
 - (b) e^+e^- continuum from hardron decay

3.6.1 Fake electron pairs

If the tracks are closer in the detectors, the pairs are candidate of fake electron pairs.

Two tracks share the same Cerenkov ring projection on RICH PMT plane due to the spherical mirror optics of RICH when a track is parallel to a true electron while passing through the RICH radiator. These pairs have a small and correlated opening angle and therefore made correlation in the invariant mass spectrum around $0.5 \text{ GeV}/c^2$.

To eliminate the fake pairs, the cut for the distance between two tracks on z and ϕ plane of each detectors are applied. In Drift Chamber, the cuts applied $\Delta z < 0.5 \text{ cm}$ and $\Delta\phi < 0.02 \text{ rad}$. In RICH, the cuts applied $\Delta z < 28 \text{ cm}$ and $\Delta\Phi < 0.07 \text{ rad}$. In addition, the the case of RICH, the cut defined as the angle between two tracks at Drift Chamber called "PFOA(Post-Field Opening Angle)" is also used. Fig.3.14 shows correlation between PFOA(Post-Field Opening Angle) and $\Delta RICH$. $\Delta RICH$ is defined as

$$\Delta RICH \equiv \sqrt{(|\Delta z_{RICH}|/\sigma_z)^2 + (|\Delta\phi_{RICH}|/\sigma_\phi)^2} \quad (3.8)$$

where σ_z and σ_ϕ means 1σ for Δz_{RICH} and $\Delta\phi_{RICH}$ distribution, respectively. If any two tracks fulfill $|\Delta RICH| < 3 \sigma$ and PFOA $< 0.25 \text{ rad}$, both of the tracks are eliminated. These cut parameters were determined by comparing real with mixed event as mentioned in Section 3.6.3.

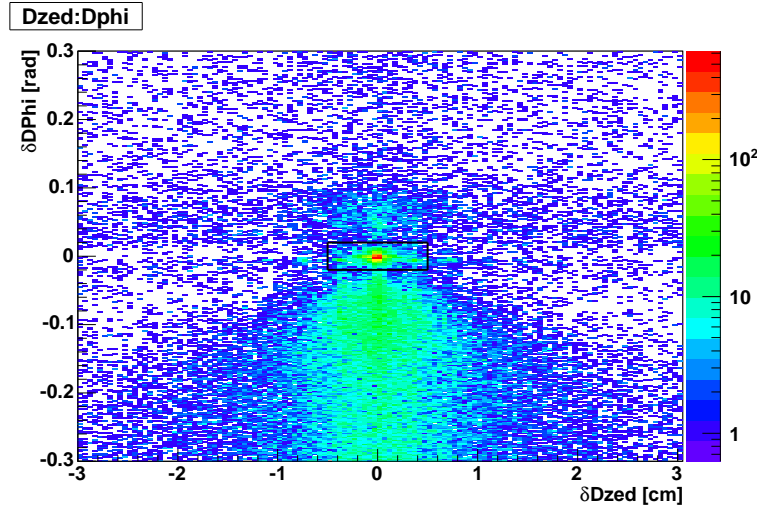


Figure 3.13: $\Delta\phi$ and Δz distribution for pairs of the tracks in DC. The box represents the cut for removed fake pairs in DC.

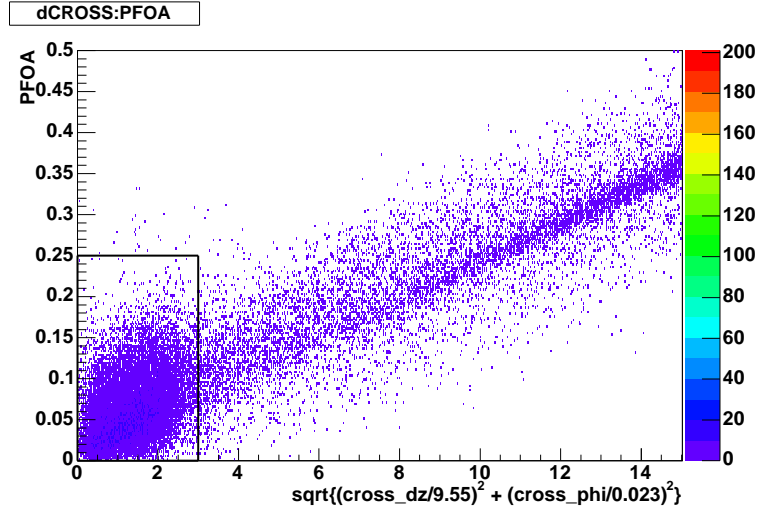


Figure 3.14: The distribution for $PFOA$ and $\Delta RICH$. The detail is in the sentence. The box represents the cut for removed fake pairs for ring sharing tracks.

3.6.2 Photon conversion

The pairs originating from photon conversion in the detector material is reconstructed as background. Tracking algorithm assumes all particles come from collision vertex corresponding azimuthal radial distance $R = 0$. Therefore pairs from photon conversion occurring off vertex ($R \neq 0$ cm) are reconstructed incorrect momentum. Their reconstructed momentum is higher which leads to an fake invariant mass that increase with radial distance between collision vertex and conversion point.

beam pipe material ($R=4$ cm)	$m_{ee} = 20 MeV/c^2$
detector support structures ($R=25$ cm)	$m_{ee} = 125 MeV/c^2$
from the entrance window of DC	$m_{ee} < 300 MeV/c^2$

The procedure to identify the pair of photon conversion is shown below. The opening angle of Conversion pairs is exactly zero since photon is massless. They are bent only azimuthal direction by magnetic field along the beam axis \vec{z} .

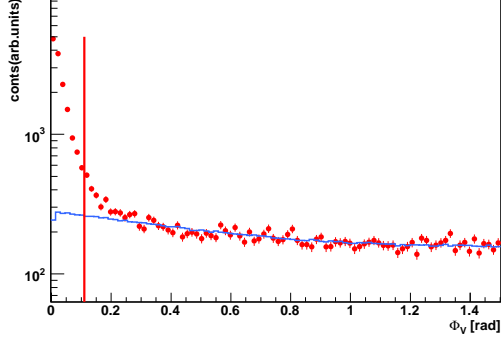


Figure 3.15: Φ_V distribution in the mass range $30 < m_{ee} < 90 MeV/c^2$. blue line show the Φ_V distribution reconstructed in event mixing which normalized arbitrary range. Vertical red line on $0.035\pi[rad]$ indicates cut value in this mass region

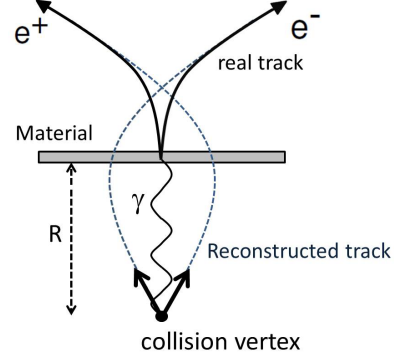


Figure 3.16: Schematic view of conversion pair. The electrons produced at $R > 0$ are reconstructed with incorrect momentum.

$$\vec{u} = \frac{\vec{p}_+ + \vec{p}_-}{|\vec{p}_+ + \vec{p}_-|} \quad (3.9)$$

$$\vec{v} = \frac{\vec{p}_+}{|\vec{p}_+|} \times \frac{\vec{p}_-}{|\vec{p}_-|} \quad (3.10)$$

$$(3.11)$$

We can defined the orientation of the actual opening angle as

$$\vec{w} = \vec{u} \times \vec{v} \quad (3.12)$$

We can also define the expected orientation of the opening angle for conversion pairs

$$\vec{w}_c = \vec{u} \times \vec{z} \quad (3.13)$$

Finally, we can define Φ_v as the angle between these two vectors

$$\Phi_V = \cos^{-1}(\vec{w} \cdot \vec{w}_c) \quad (3.14)$$

The filled blue histogram in Fig.3.17 for di-electron mass distribution is shown as contribution of the conversion pairs.

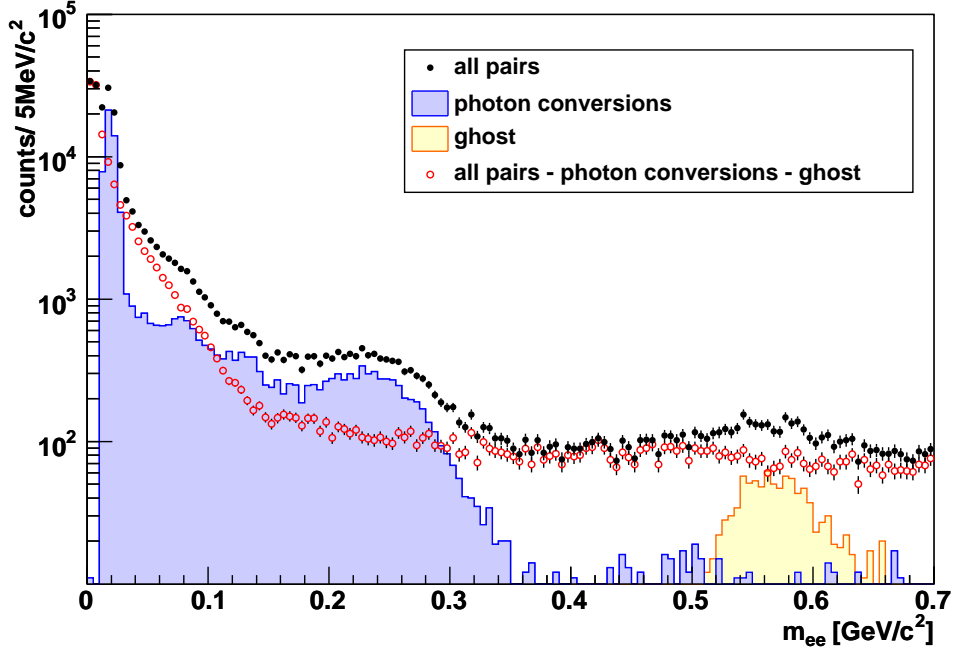


Figure 3.17: Invariant mass distribution for all e^+e^- pairs. The filled yellow histogram shows the ghost pairs. The filled blue histogram shows the pairs removed by the ϕ_V angle cut.

3.6.3 Combinatorial background

Combinatorial background arise as a result of all the combinations of two electrons which origin is uncorrelated. Uncorrelated combinatorial background can be statistically reproduced by mixed event technique, which combines tracks from different events. The mixed event is generated by combining the all of the electrons in one event and the all the electrons in another events which have the similar event topology. Since the tracks are from different events, this technique reproduces the uncorrelated background by definition. This technique also generate the background shape with negligible statistical errors since the background has much statistics related to accumulate number of event in buffer.

In this analysis, we used ERT trigger event sample in which at least one high p_T electron must be required at event by event. If mixed events background is reconstructed using ERT trigger event sample, the background can't represent true uncorrelated background shape due to the trigger bias. Therefore The mixed events background should be constructed from Minimum Bias event sample requiring that at least one of the two electrons fired the ERT

trigger. That pairs can represent true uncorrelated background reconstructed in ERT trigger event sample.

The reproduced combinatorial background is needed to be normalized. unlike-sign spectrum N_{+-} reconstructed e^+e^- pairs in same event, like-sign spectra N_{++} and N_{--} reconstructed e^+e^+ and e^-e^- in same event, respectively.

$$N_{+-} = N_{+-}(m_{ee}, p_T), \quad B_{+-} = B_{+-}(m_{ee}, p_T) \quad (3.15)$$

$$N_{++} = N_{++}(m_{ee}, p_T), \quad B_{++} = B_{++}(m_{ee}, p_T) \quad (3.16)$$

$$N_{--} = N_{--}(m_{ee}, p_T), \quad B_{--} = B_{--}(m_{ee}, p_T) \quad (3.17)$$

As long as both electrons and positrons are produced in one event, the size of the unlike-sign combinatorial background is given by the geometric mean of the number of positive and negative like-sign pairs: $B_{+-} = 2\sqrt{B_{++}B_{--}}$.

Measured all unlike-sign pairs contains correlated pairs originating from other hadron decay as shown in Section 3.6.4. In case of like-sign pairs, there is no contribution from other hadron decay due to no existence decay into e^+e^+ or e^-e^- pairs. But even if the measured like-sign pairs has correlation parts which origin from follows:

- the pairs originating from same jet which have strong correlation on $\Delta\phi \sim 0$ or π [rad]
- pairs from decay in $\pi^0 \rightarrow (e^+e^-\gamma \text{ or } \gamma\gamma) \rightarrow e_1^+e_1^-e_2^+e_2^-$

By study of Monte Carlo simulation, we found the region as shown in Fig. 3.18 in 2 dimensional space of p_T vs mass is less contributed from correlated like-sign pairs [89]. Integration of the N_{++} and N_{--} in region A is used for calculation of normalization factors to avoid counting the number of correlated pairs.

$$N'_{++} = B_{++} \frac{\int_A N_{++}}{\int_A B_{++}} dm_{ee} dp_T \quad (3.18)$$

$$N'_{--} = B_{--} \frac{\int_A N_{--}}{\int_A B_{--}} dm_{ee} dp_T \quad (3.19)$$

The absolute normalization factor α is expressed as follow:

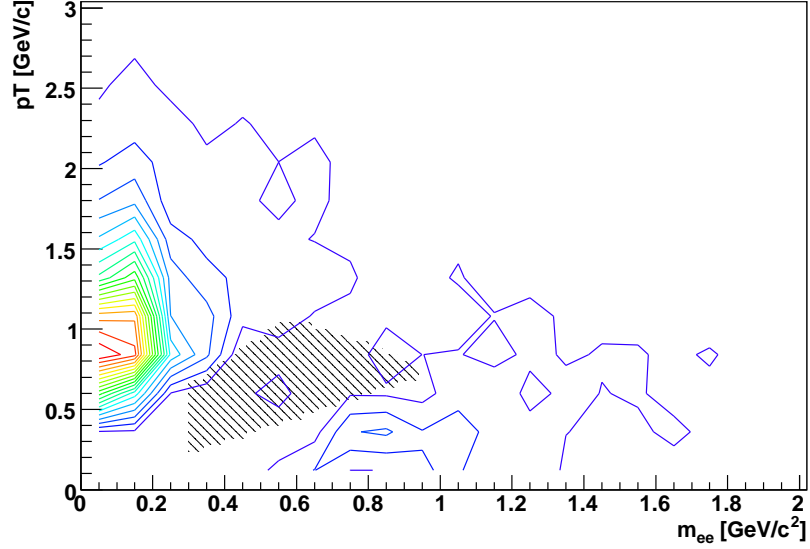


Figure 3.18: like-sign pairs distribution as a function of mass and pair p_T after subtraction of mixed event background. The background is normalized in the normalization area A shown as the dashed area.

$$\alpha = \frac{2\sqrt{N'_{++} \times N'_{--}}}{B_{+-}} \quad (3.20)$$

$$= \frac{2\sqrt{B_{++} \frac{\int_A N_{++}}{\int_A B_{++}} \times B_{--} \frac{\int_A N_{--}}{\int_A B_{--}}}}{B_{+-}} \quad (3.21)$$

$$= \sqrt{\frac{\int_A N_{++} \times \int_A N_{--}}{\int_A B_{++} \times \int_A B_{--}}} \quad (3.22)$$

The invariant mass distribution are shown in Fig.3.19 for all p_T and Fig.3.20 as divided by nine p_T bins of $0 < p_T < 0.25$, $0.25 < p_T < 0.5$, $0.5 < p_T < 0.75$, $0.75 < p_T < 1.0$, $1.0 < p_T < 1.25$, $1.25 < p_T < 1.5$, $1.5 < p_T < 1.0$, $1.5 < p_T < 2.0$, $2.0 < p_T < 4.0$. The combinatorial background contribution evaluated by event mixing technique and normalized by absolute normalization factor α is shown as blue line in Fig.3.19 and Fig.3.20.

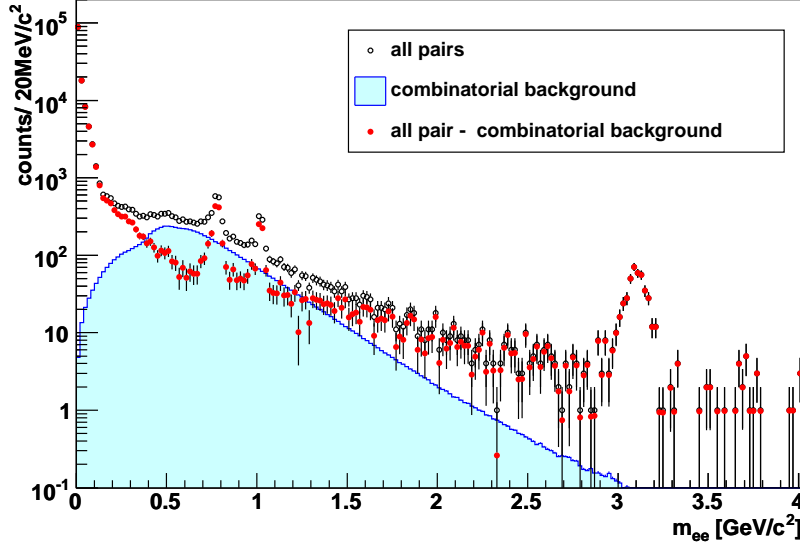


Figure 3.19: invariant e^+e^- mass spectrum. The blue line indicate combinatorial background evaluated by the event mixing method.

3.6.4 continuum contribution

In the remaining di-electron mass spectra represents contribution of correlated pairs so-called continuum, originated from various hadron decay into di-electron mainly as follows; $\pi^0 \rightarrow \gamma e^+e^-$, $\eta \rightarrow \gamma e^+e^-$, $\rho, \omega, \phi \rightarrow e^+e^-$, $J/\Psi \rightarrow e^+e^-$ and open *charm* $c\bar{c}$. The shape of continuum from other hadrons in the mass range of 0.5 to 1.2 GeV/c^2 and assumed as exponential function + constant. The amount of the contribution for ω and ϕ mesons were approximately less than factor of 0.1 and 0.3, respectively.

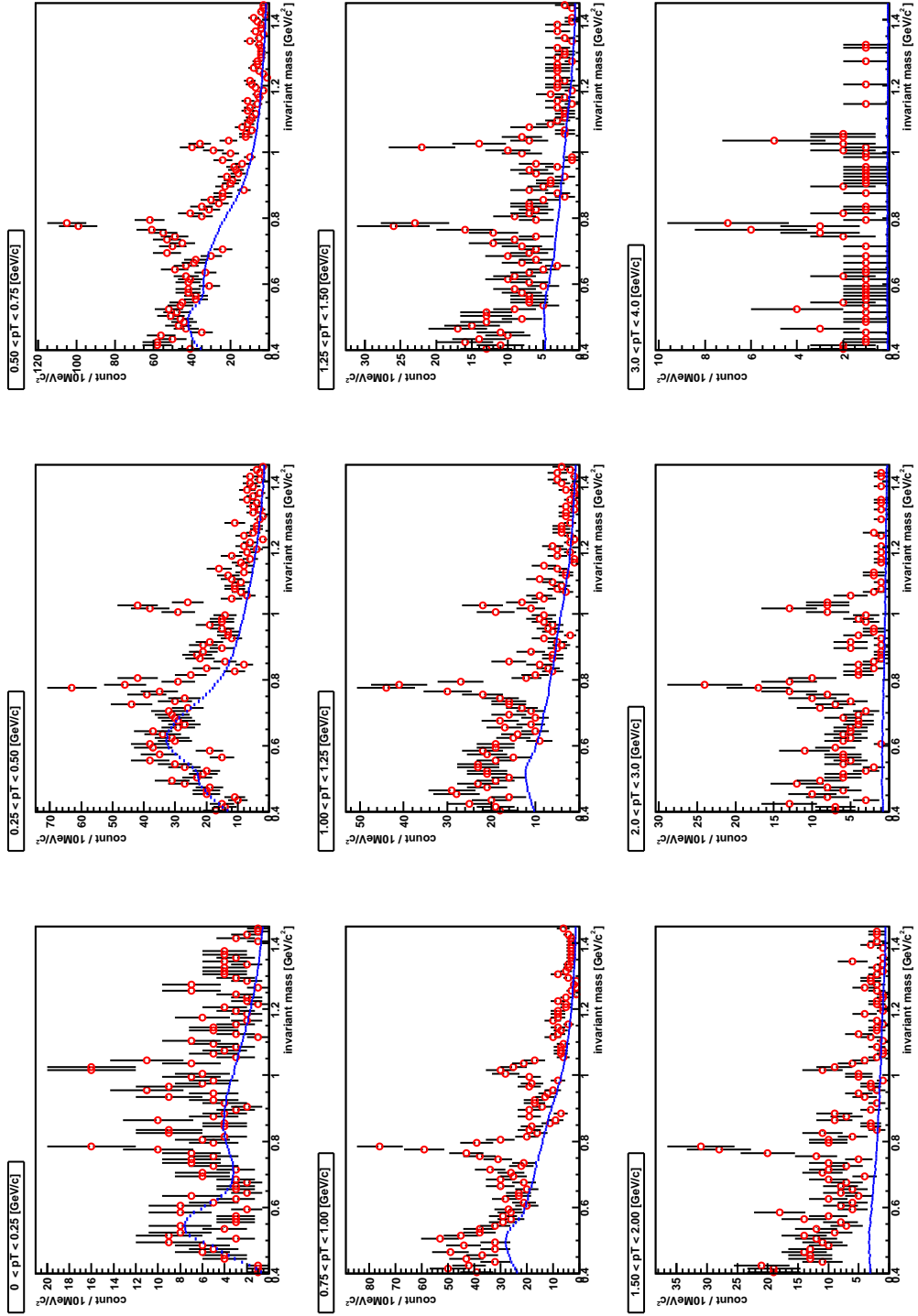


Figure 3.20: Invariant mass spectra divided by pT bins. The blue line indicate combinatorial background evaluated by the event mixing method.

3.7 Signal Extraction

3.7.1 Spectral Shape of Resonances

Spectral shape of resonances were generated using the relativistic Breit-Winger distribution

$$rBR(m) = \frac{m^2 \Gamma_{tot}(m) \Gamma_{ee}(m)}{(m^2 - m_0^2)^2 + m_0^2 \Gamma_{tot}(m)^2} \quad (3.23)$$

with the pole mass, m_0 , total decay width, $\Gamma_{tot}(m)$ and the energy dependent partial decay width of the vector meson going to e^+e^- , $\Gamma_{ee}(m)$. $\Gamma_{tot}(m)$ and $\Gamma_{ee}(m)$ can be parametrized as

$$\Gamma_{tot}(m) = \frac{m}{m_0} \Gamma_{tot} \quad (3.24)$$

$$\Gamma_{ee}(m) = \frac{m_0^3}{m^3} \Gamma_{ee} \quad (3.25)$$

where Γ_{tot} is the natural decay width, Γ_{ee} is the partial width of the vector meson decaying into e^+e^- . The values of the natural decay widths and pole masses of vector mesons are shown in table 3.2

Due to the finite detector resolution, the spectral shape smeared. therefore the relativistic Breit-Winger function is convoluted by Gaussian. The sigma of the Gaussian is obtained by simulation as mention later in Sec.xxx.

	mass [MeV/c ²]	Γ_{tot} [MeV/c ²]	$c\tau$ [fm]	Γ_{ee}/Γ_{tot}
ρ	771.1	149.2	1.3	0.454×10^{-4}
ω	782.57	8.44	23.2	0.695×10^{-4}
ϕ	1019.456	4.26	46.2	2.96×10^{-4}

Table 3.2: The pole masses and natural decay widths of the vector mesons taken from the PDG [48]

Radiative tail correction

The internal radiative correction to e^+e^- was estimated. The observation of radiative decays $J/\psi \rightarrow e^+e^-\gamma$ was reported and the result is consistent with a QED calculation based on final state radiation [90]. The internal radiative decay is described by the diagrams shown Figure 3.21.

An analytic formula for the di-lepton mass spectra in radiative decays is derived [91]. The fraction of decays corresponding to the emission of hard

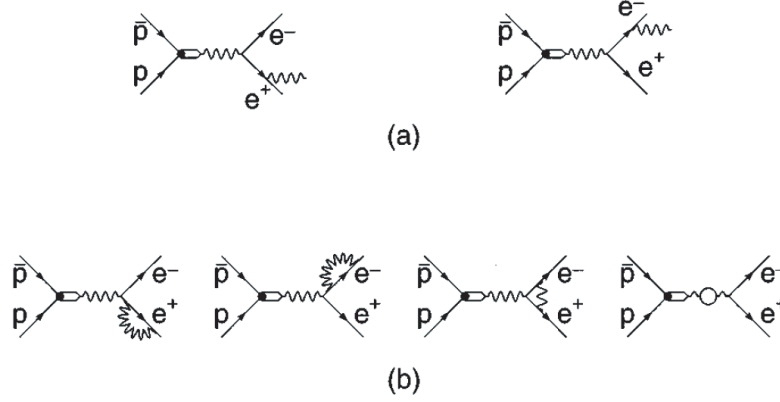


Figure 3.21: Diagrams for final state radiation [90]. The decay into $e^+e^-\gamma$ is described by (a). The infrared divergence in the decay is canceled by interference with the diagrams in (b).

photons is

$$C_{hard} = \frac{\alpha}{2\pi} \left[4 \ln \frac{M}{2E_{min}} \left(\ln \frac{M^2}{m_l^2} - 1 \right) - 3 \ln \frac{M^2}{m_l^2} - \frac{2}{3} \pi^2 + \frac{11}{2} \right] \quad (3.26)$$

where E_{min} is the minimal photon energy, M is a mass of parent particle and m_l is a mass of leptons. The di-lepton mass m is shifted by photon emission

$$m = \sqrt{M(M - 2E_\gamma)} \approx M - E_\gamma (E_\gamma \leq M) \quad (3.27)$$

Hard photon emission cause a tail towards lower mass in the di-lepton mass spectrum. The distribution $P(m)$ of the di-lepton mass in the radiative decay is described as

$$P(m) = \frac{\alpha}{\pi} \frac{2m}{(M^2 - m^2)} \left(1 + \frac{m^4}{M^4} \right) \left(\ln \frac{1+r}{1-r} - r \right) \quad (3.28)$$

where $r = \sqrt{1 - 4m_l^2/m^2}$ is also a function of m . For instance, fig. 3.22 shows the de-electron mass spectra in the radiative decay $\phi \rightarrow e^+e^-\gamma$ for $E_{min} = 10\text{MeV}$. The broad curve is expressed as smeared spectra by detector mass resolution of $10\text{MeV}/c^2$.

Measured resonance peak of ω and ϕ meson were fit into the function of relativistic Breit-Wigner plus radiative tail which were convoluted by Gaussian as the detector mass resolution obtained Monte Carlo simulation as shown in Section 3.8.1.

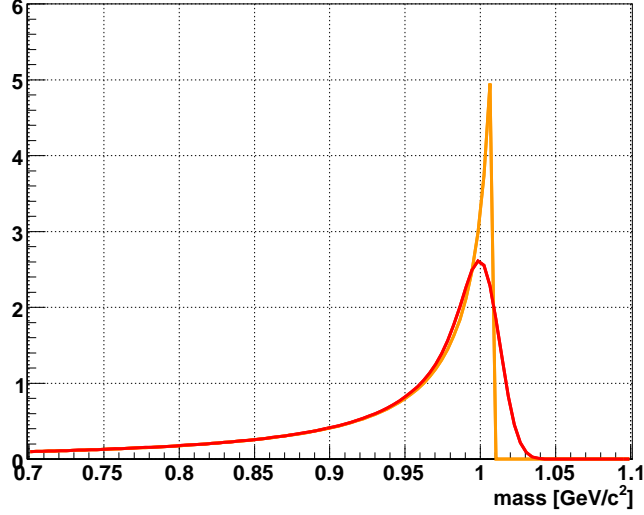


Figure 3.22: e^+e^- mass spectrum in the radiative decay $\phi \rightarrow e^+e^-\gamma$ for $E_{min} = 10\text{MeV}$ (orange) smeared with 10MeV (red).

3.7.2 Signal extraction

Number of signal S was obtained $N^{+-} - B$. The remaining background is contribution from continuum of other hadrons. We assumed the shape of the continuum on the mass range of ω and ϕ is exponential. To obtain background contribution on the mass range of ω and ϕ meson, the invariant mass distribution is fit into following function

$$\begin{aligned}
 f(m_{ee}) = & \text{Gaussian convoluted (r.BW + radiative tail)} \\
 & + \text{Breit Wigner} \\
 & + (\text{exponential + constant})
 \end{aligned}
 \tag{3.29}$$

The first term is for ω and ϕ mesons. The second term, Breit-Wigner, is for ρ mesons. Finally, the function of exponential + constant is for remaining background by continuum contribution.

The fitting parameters for ω and ϕ mesons were the peak amplitude, mass center and the width Γ_{tot} while the experimental mass resolution are fixed to the value obtained by Monte Carlo simulation as mention Section xx. In addition, mass center and the width Γ_{tot} for ρ mesons are fixed to PDG value. The experimental mass resolution is not included for ρ mesons since the Γ_{tot}

of ρ meson is much broader than resolution. The ratio between the number of ρ and ω meson were fixed. The ω/ρ ratio is fixed to 1.53, which obtained by ration of branching into $e^+ + e^-$ with the assumption that the production yields of ω and ρ were same. Then, we assumed that the production cross section of ω and ρ is same. The fitting result for invariant mass spectra as a function of p_T were shown in Fig.3.23.

The number of ω and ϕ was obtained by counting the number of entries within 3σ on the each peaks, and subtracted the contribution of background B contained hadron continuum and ρ meson.

Fig.3.24 shows raw yields for ω and ϕ mesons, ρ meson contribution, combinatorial background, remaining background as exponential function + constants and the sum of all components, divided by bin width of p_T and number of used events as a function of p_T .

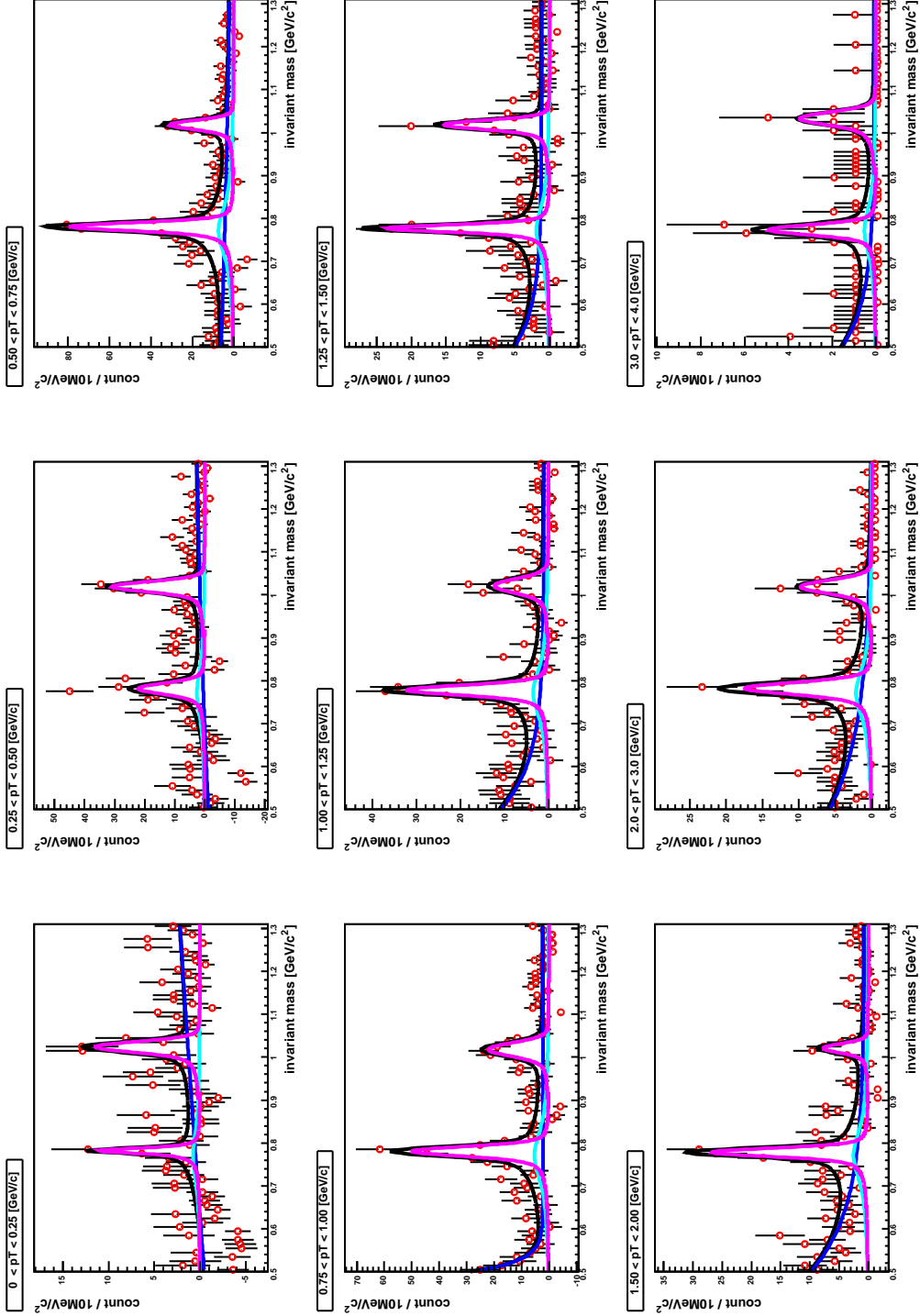


Figure 3.23: Invariant mass spectra divided by pT bins after background subtraction. The black line are the fitting result, which is sum of the known decays, ω (left magenta line), ϕ (right magenta line), ρ (orange line), radiative decay of ω and ϕ (blue line) and BG (blue line).

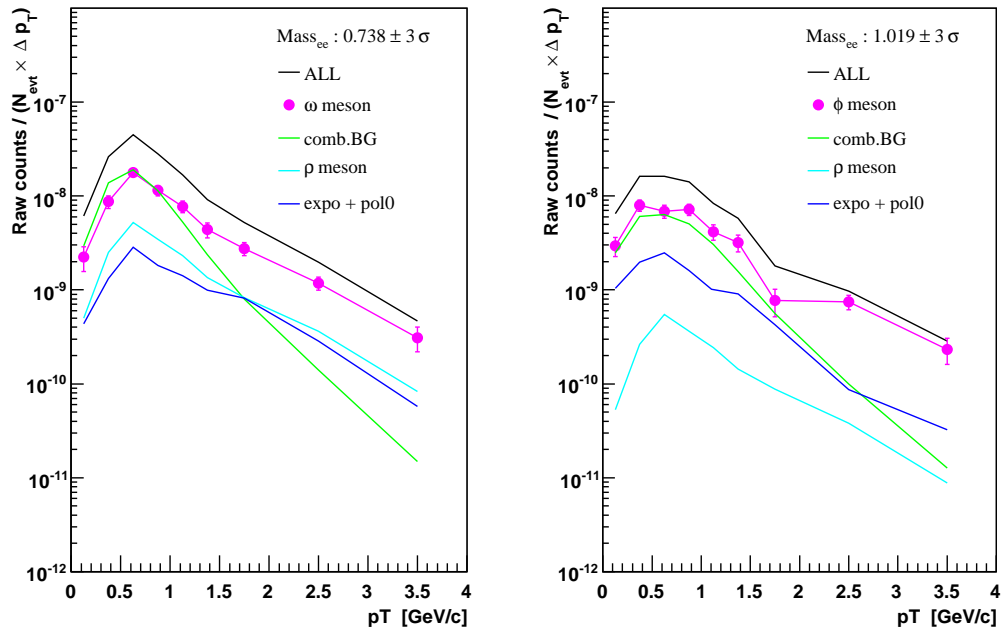


Figure 3.24: Raw counts in counting range for ω (left) and ϕ (right) mesons as a function of p_T . The black lines show all contributions, the magenta points show ω (left) and ϕ (right) mesons including statistical errors, green line lines show combinatorial background, the light blue lines show ρ mesons, and blue lines show exponential+polynomial as contribution of other hadron continuum.

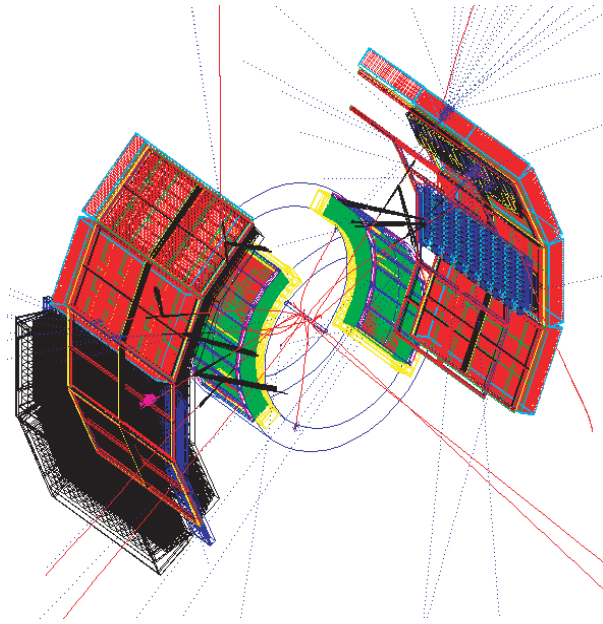


Figure 3.25: The PHENIX central arm detectors represented in GEANT simulation

3.8 Monte Carlo simulation

3.8.1 Reconstruction efficiency

The detector acceptance was determined by single particle Monte Carlo simulation. The ω and ϕ mesons were generated and decay into e^+e^- by using single particle event generator, EXODUS. The ϕ and ω mesons were uniformly generated within $|y| < 0.5$ in rapidity and full azimuthal angle of $0 < \Phi < 2\pi$, and the z-vertex within $|z| < 30\text{cm}$. The generated transverse momentum range was 0 to $5\text{GeV}/c$ which enough covered the measured range of signal extracted from data. The generated transverse momentum spectra were weighted to much the measured particle spectra.

The PHENIX detector simulation was based on GEANT code, called PISA ("PHENIX Integreted Simulation Application"), which including detector performance of momentum, spacial, energy resolutions. In addition, PISA tracks secondary particles generated from the interaction with represented detector materials. Indeed the simulation data should be reproduced same detector performance with real data. The detector acceptance for single electron on ϕ and z direction, each electron identification parameters were compared to confirm consistency between simulation and real data. In fig.3.28 shows the ϕ distribution for single electron and positron with North

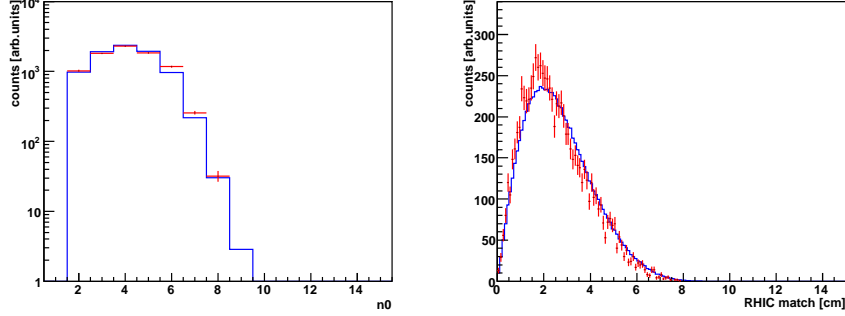


Figure 3.26: Left panel) RICH n_0 . Right panel) RICH displacement.

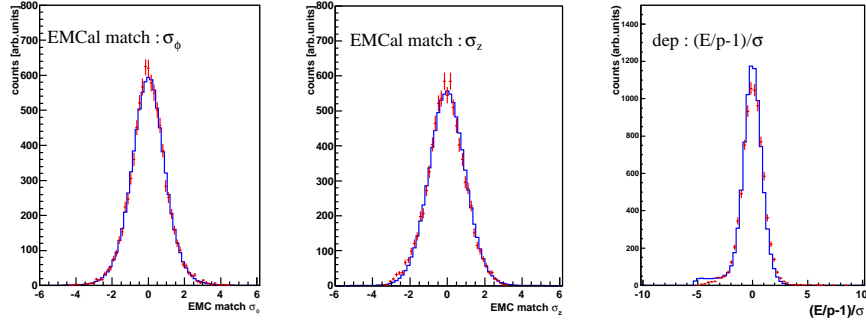


Figure 3.27: Left panel) EMC match for ϕ direction. Middle panel) EMC match for z direction. Right panel) Energy over momentum ratio normalized that width : dep direction.

and South side of Drift Chamber in the real and simulated data. The simulated ϕ distribution is weighted by appropriate electron p_T distribution in real data. The simulated data is scaled such that the integral of the whole range of ϕ distribution in the real and simulated data are agreed.

The electron identification parameters of RICH, n_0 and displacement are shown in Fig.???. The electron identification parameters of EMCal matching for ϕ and z direction are shown in Fig.???. The electron identification parameters of Energy momentum ratio is shown in Fig.???. The systematic uncertainty of the acceptance is estimated due to a little discrepancy of the acceptance between the real and simulation data.

The same analysis code was used for reconstruction of simulated and real data. The invariant mass spectra for ω and ϕ mesons reconstructed e^+e^- in simulation are shown in left panel of Fig.3.30 and Fig.3.31, respectively. The spectra can be described by the function of Gaussian convoluted relativistic Breit-Wigner, where the term of the width of Gaussian will reproduce the

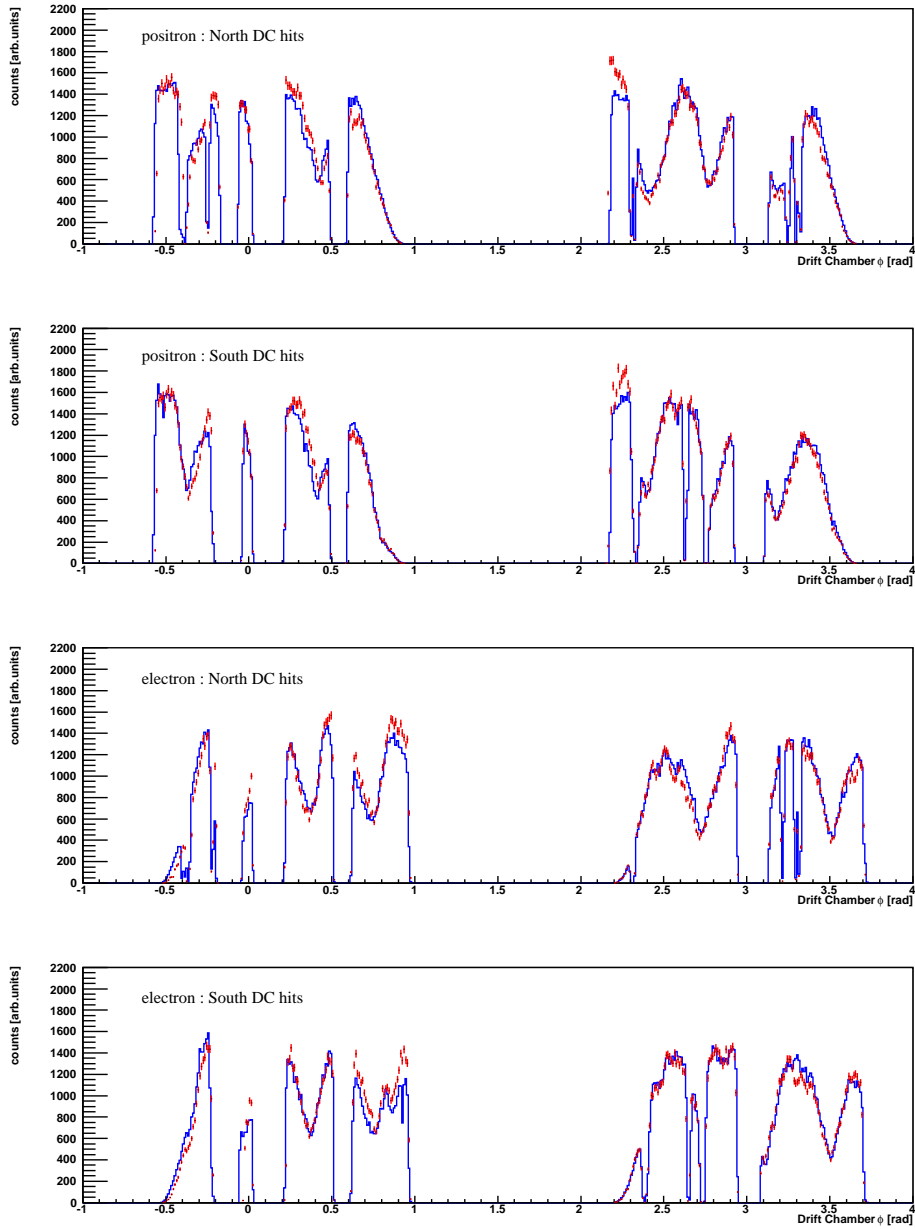


Figure 3.28: Comparison of Drift Chamber hit distribution for ϕ direction in the real data (red) and simulation data (blue). The p_T range of the electron is $0.3 < p_T < 4.0 \text{ GeV}/c$ for both real and simulation data.

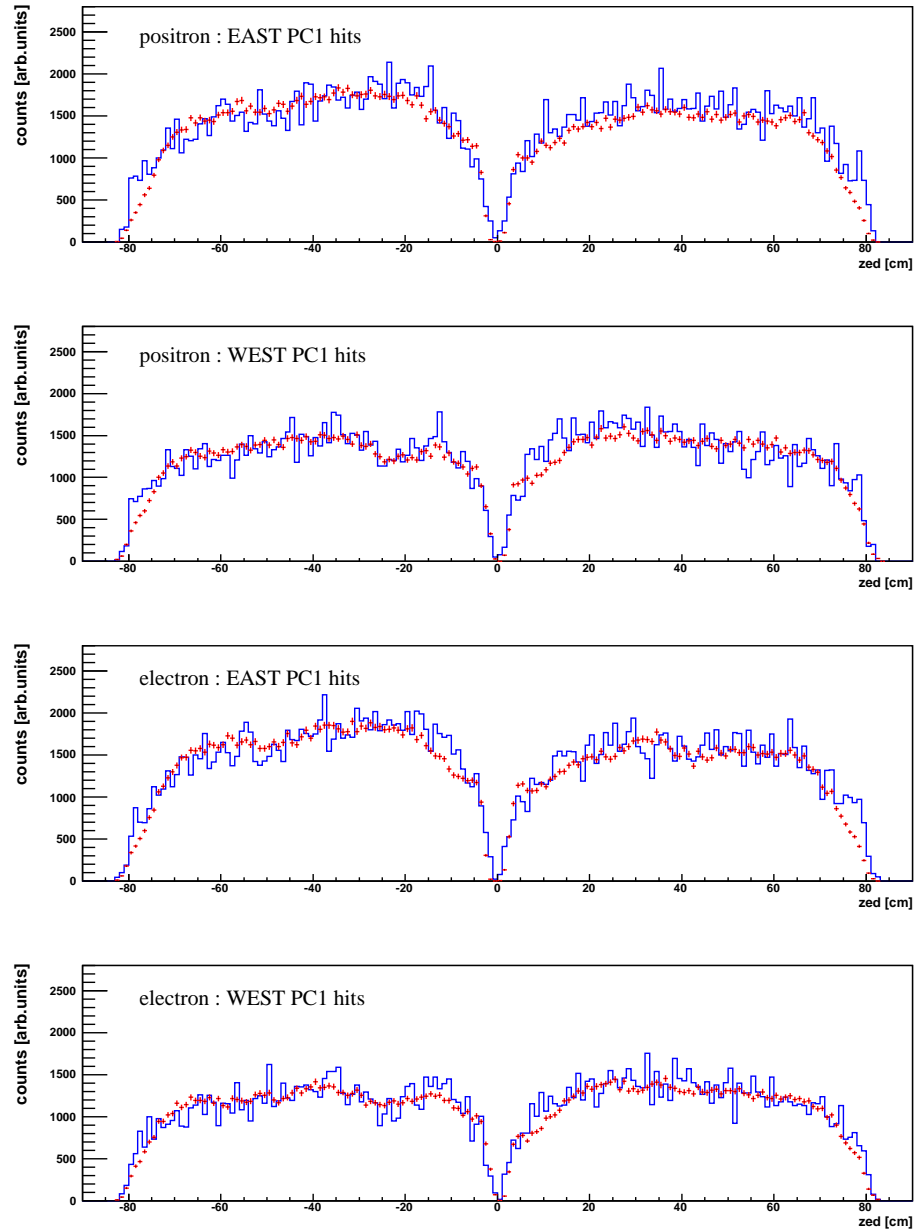


Figure 3.29: Comparison of PC1 hit distribution for z direction in the real data (red) and simulation data (blue). The p_T range of the electron is $0.3 < p_T < 4.0 \text{ GeV}/c$ for both real and simulation data.

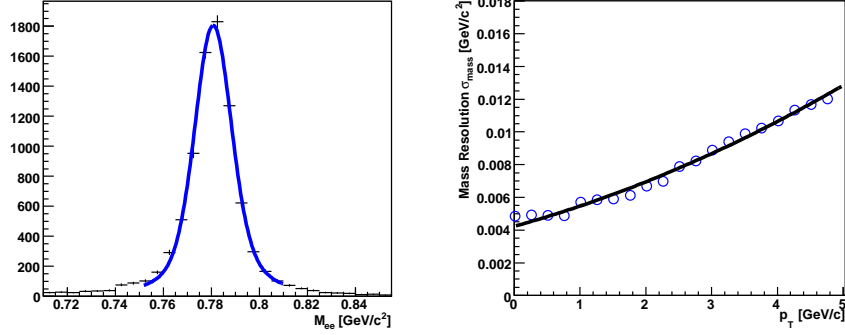


Figure 3.30: Left panel) The invariant mass spectra for ω meson reconstructed e^+e^- in simulation for the $1.0 \leq p_T < 1.25$ GeV/ c . The solid line shows Gaussian convoluted relativistic Breit-Winger function. Right panel) p_T dependent detector mass resolution.

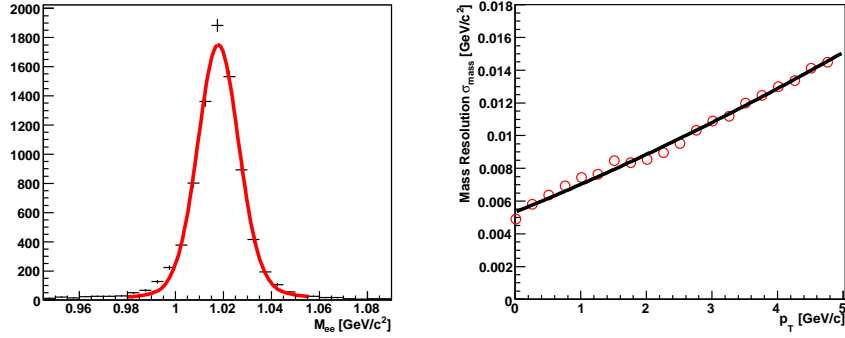


Figure 3.31: Left panel) The invariant mass spectra for ϕ meson reconstructed e^+e^- in simulation for the $1.0 \leq p_T < 1.25$ GeV/ c . The solid line shows Gaussian convoluted relativistic Breit-Winger function. Right panel) p_T dependent detector mass resolution.

detector mass resolution mainly related to momentum resolution of PHENIX detectors. The detector mass resolution for the mass range of ω and ϕ mesons are shown as a function of p_T in right panel of Fig.3.30 and Fig.3.31, respectively.

The reconstruction efficiency is calculated as the ratio of the number of fully reconstructed particle to the number of generated particle. Fig.3.32 shows the reconstruction efficiency as a function of transverse momentum of ω and ϕ meson. the curve take into account for the detector geometry, particle decay kinematics, analysis cuts for electron identification.

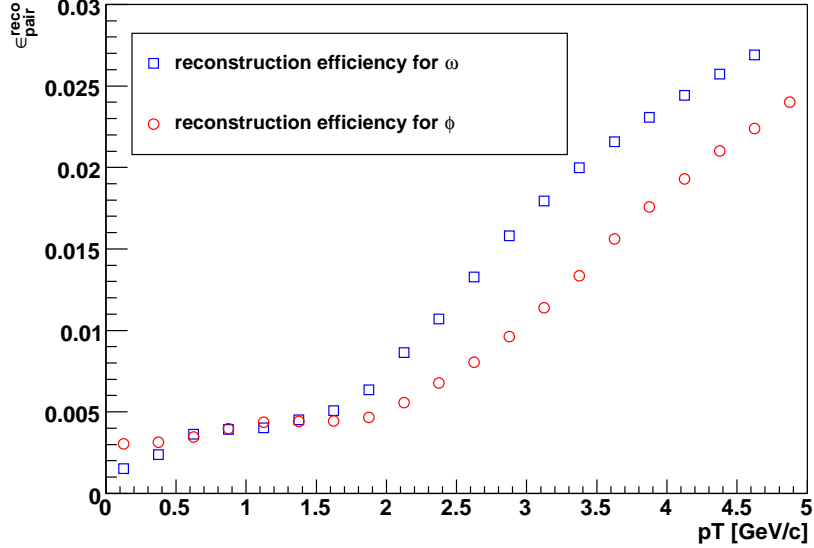


Figure 3.32: Reconstruction efficiency for ω and ϕ mesons ϵ_{pair}^{reco} as a function of p_T .

3.8.2 ERT trigger efficiency

The efficiency of ERT trigger for single electron is determined in sector-by-sector using Min.Bias event sample therefore Min.Bias trigger sample contains ERT trigger sample. We are able to identify the electron which fires ERT trigger tile (both RICH and EMCal Super Module). The single electron ERT trigger efficiency was calculated as the ratio of number of triggered electrons to number of all electrons for each sector and shown in Fig.3.33 as a function of transverse momentum.

The curve is steeply growing up and half of the height is corresponding to approximately EMCal trigger threshold of 400MeV. The reason why trigger efficiency is below 100% is due to the inactive area of the RICH ERT efficiency.

The curve of trigger efficiency for single electron is described as

$$f(p_T) = \epsilon \times \text{Erf}\left(\frac{p_T - a}{\sigma}\right) \quad (3.30)$$

$$\text{Erf}(x) = \frac{2}{\sqrt{\pi}} \int_0^x e^{-t^2} dt \quad (3.31)$$

where ϵ , a , σ are free parameters.

For the evaluating the ERT trigger efficiency for ω and ϕ meson this curve for single electron is embedded into Monte Carlo simulation as was used for reconstruction efficiency calculation. At first we required that the both

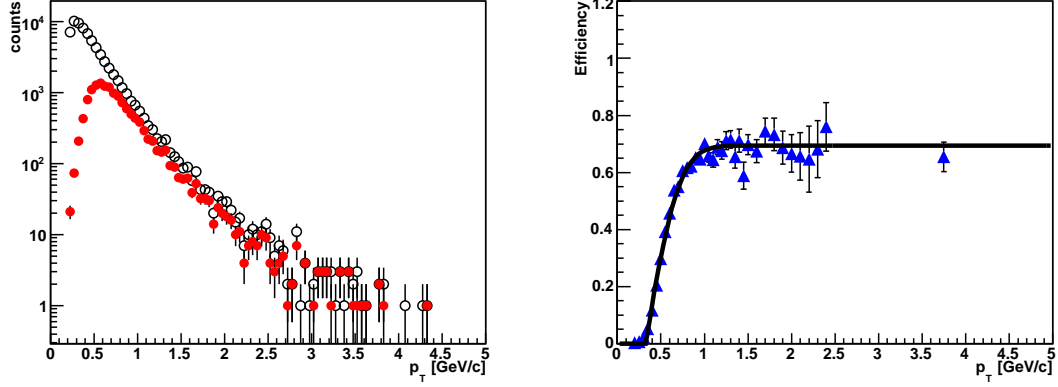


Figure 3.33: (left) The p_T distribution for single electron in MB (black) and fired ERT (red). (right) Trigger efficiency for single electrons ϵ_{single}^{ERT} as a function of p_T .

electron and positron are reconstructed within PHENIX acceptance without the ERT trigger requirement. Then, for the all sectors of EMCAL associated with electrons, we generated a random number between 0 to 1 and compared it to the magnitude of the curve shown Eq.xx at the same transverse momentum. The particle was considered to fire the ERT trigger if at least one of the randomly generated numbers was lower than the corresponding magnitude of the curve. The probability of fire the ERT trigger for ω and ϕ mesons is shown in Fig.3.34.

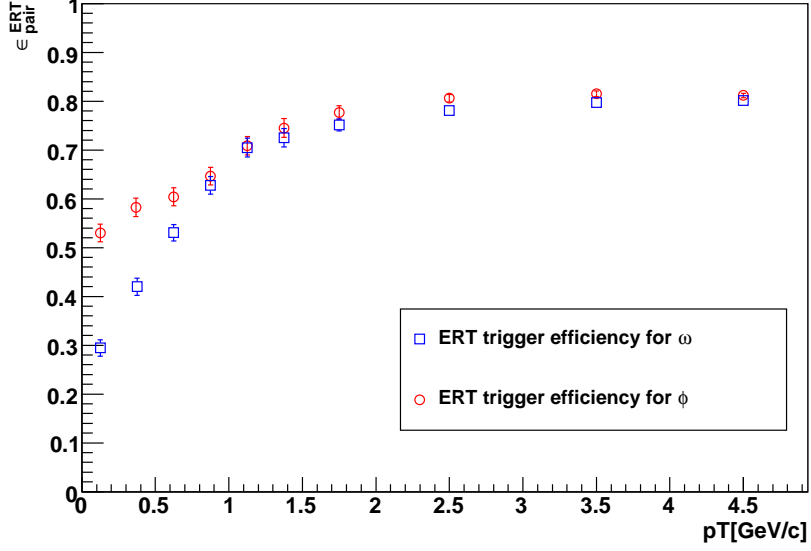


Figure 3.34: Trigger efficiency for ω (blue) and ϕ (red) mesons ϵ_{pair}^{ERT} as a function of p_T .

3.9 Invariant differential cross section

The invariant differential cross section for ϕ and ω production as a function of p_T in $p + p$ collisions can be written as follows;

$$E \frac{d^3\sigma}{dp^3} = \frac{1}{2\pi p_T} \frac{d^2\sigma}{dp_T dy} \quad (3.32)$$

$$= \frac{1}{2\pi p_T} \frac{1}{\mathcal{L}} \frac{1}{BR} \frac{1}{\epsilon_{bias} \epsilon_{pair}^{reco} \epsilon_{pair}^{ERT}} \frac{N_{\omega,\phi}(\Delta p_T)}{\Delta p_T \Delta y} \quad (3.33)$$

with integrated luminosity

$$\mathcal{L} = \frac{N_{event}^{MB}}{\sigma_{BBC}}, \quad (3.34)$$

where

- N_{event} is the Number of MinBias sampled events.
- BR is branching ratio into e^+e^- , $7.28 \pm 0.14 \times 10^{-5}$ for ω meson and $2.95 \pm 0.03 \times 10^{-4}$ for ϕ meson.
- Δp_T is the width of p_T bin.

- ϵ_{pair}^{reco} is the acceptance and reconstruction efficiency.
- ϵ_{pair}^{ERT} is the ERT trigger efficiency.
- $\sigma_{BBC} = 23.0 \pm 2.2 [\text{mb}]$ is the Minimum Bias trigger cross section. The efficiency of the minimum bias trigger is estimated to be $55 \pm 5\%$ of total inelastic cross section of $\sigma_{inel}^{pp} = 42 \pm 3 \text{mb}$.
- $\epsilon_{bias} = 0.79 \pm 0.02$ is the minimum bias trigger efficiency for events containing meson.

Bin shift correction

The bin shift correction was applied to take into account the finite width of p_T bins used in the analysis. The measured yield in each p_T bins is not the value at the center of p_T bin but the average in the p_T bin. The bin width is large and/or the spectra is steeply fall, then this effect is more significant. To correct for this effect, we moved the data point vertically and leave the p_T of the data point.

The procedure is below. At first the data points were fit into the Levy function $f(p_T)$ which can be approximately described real spectra shape. the correction factor r , which is the ratio between the average yield in this p_T bin and the value of the function at the bin center p_T^C , can be calculated as

$$r = \frac{\frac{1}{\Delta} \int_{p_T^C - \Delta/2}^{p_T^C + \Delta/2} f(p_T) dp_T}{f(p_T^C)} \quad (3.35)$$

where Δ is the bin width. The corrected yield in the given p_T bin is then calculated as

$$dN/dp_T|_{corrected} = \frac{dN/dp_T|_{uncorrected}}{r} \quad (3.36)$$

The effect of this bin shift correction is approximately a few % in $\Delta p_T = 1 \text{GeV}/c$ and shown in Fig.3.35 and Fig.3.36.

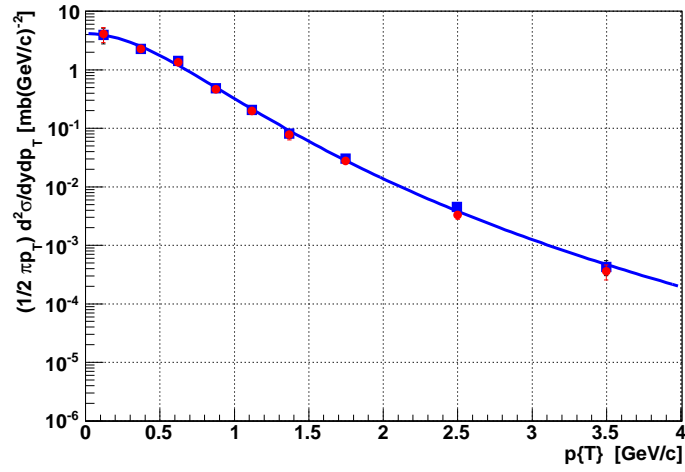


Figure 3.35: Bin shift correction for ω . Blue point and line shows before correction, and red point shows after correction.

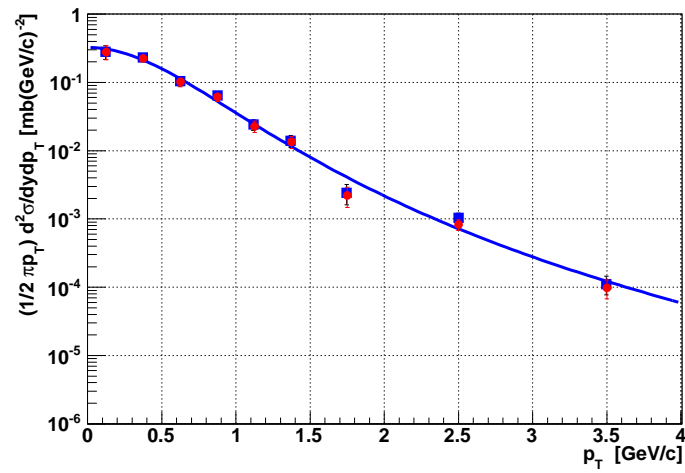


Figure 3.36: Bin shift correction for ϕ . Blue point and line shows before correction, and red point shows after correction.

3.10 Systematic Uncertainty

This section summarizes the source of the systematic uncertainties that contribute to invariant cross section as follows:

signal extraction

This is the uncertainty for methods of signal extraction for the window to count the signal, fitting range, background shape, threshold emitting gamma energy for radiative tail. The uncertainties are evaluated by varying 1)the window to count the signal to 2σ and 4σ , 2)the fitting range to 0.5-1.15GeV/ c^2 and 0.4-1.25GeV/ c^2 , 3)background shape to 2nd polynomial and 3rd polynomial, 4)threshold of emitting gamma energy for radiative tail to 5MeV and 15MeV. For each case, the raw yield was extracted and the resulting RMS of these yield for each p_T bins are assigned as systematic errors.

Acceptance

This is the uncertainty in how well the acceptance of PHENIX detectors in the simulation agrees with real data. We evaluate this comparing the phi distribution of hit position in the data and simulation.

electron ID

This is the uncertainty of electron identification efficiency for RHIC cut, EMC track matching and energy momentum ratio. We evaluate this by varying each eID cuts parameters in both of real and simulation, and monitoring the deviation of recalculating cross section from basic value as systematic errors.

ERT trigger efficiency

The uncertainties in the ERT trigger efficiency are evaluated by varying the single electron efficiency curve for every EMCal sectors in simulation.

bin shift correction

The uncertainty for bin shift correction due to function shape assumed to fit real data was evaluate to use other functions; Hagedron function and exponential function.

3.10.1 Total systematic error

Various systematic errors are summarized in Table.3.3, 3.4.

pT	0.-0.25	0.25-0.5	0.5-0.75	0.75-1.0	1.0-1.25	1.25-1.5	1.5-2.0	2.0-3.0	3.0-4.0
signal	10.5%	17.3%	5.4%	7.6%	8.4%	8.1%	5.9%	6.7%	5.5%
acceptance	4.5%								
electron ID	8.9%								
ERT trigger	2.4%	2.0%	1.8%	1.1%	1.2%	1.3%	1.3%	1.1%	1.1%
bin shift	2.7%	1.7%	0.4%	0.3%	0.5%	0.4%	0.6%	5.1%	10.3%
σ_{BBC}	9.6%								
ϵ_{bias}	2.5%								
Total	17.9%	22.5%	15.2%	16.0%	16.4%	16.3%	15.3%	16.4%	18.3%

Table 3.3: Total systematic error for ω meson

pT	0.-0.25	0.25-0.5	0.5-0.75	0.75-1.0	1.0-1.25	1.25-1.5	1.5-2.0	2.0-3.0	3.0-4.0
signal	16.7%	6.0%	3.8%	5.7%	8.7%	5.2%	15.8%	9.6%	6.0%
acceptance	4.5%								
electron ID	8.1%								
ERT trigger	1.1%	1.2%	2.0%	1.8%	1.5%	1.4%	1.1%	1.2%	1.1%
bin shift	1.6%	1.0%	0.7%	0.4%	0.3%	0.4%	2.2%	12.6%	16.3%
σ_{BBC}	9.6%								
BBC bias	2.5%								
Total	21.6%	14.9%	14.3%	14.9%	16.2%	14.6%	21.0%	20.9%	22.1%

Table 3.4: Total systematic error for ϕ meson

Chapter 4

Results and Discussions

In this section, we show the result of ω and ϕ meson production via di-electron decay channels in p+p collisions at $\sqrt{s} = 200\text{GeV}$; the spectra of invariant cross section as a function of p_T , total cross section for ω and ϕ and the particle ratio of ω/π^0 , ϕ/π^0 . We also present the the transverse mass(m_T) spectra for various mesons and scaling behavior. In addition, the di-electron mass distribution is analyzed with simple model to evaluate mass shift quantitatively.

4.1 Spectra of the invariant cross sections

Figure 4.1 shows the invariant cross section for ω and ϕ production measured in di-electron decay channel in p+p collisions at $\sqrt{s} = 200\text{GeV}$, as a function of p_T . Bars and boxes represent statistical and systematic errors, respectively.

In addition, we already measured ω and ϕ mesons via other decay modes, $\omega \rightarrow \pi^0\pi^+\pi^-$, $\omega \rightarrow \gamma\pi^0$ [93] and $\phi \rightarrow K^+K^-$ [42], in the PHENIX experiment. Figure 4.2 and 4.2 show the invariant cross section for ω and ϕ production measured in dielectron and hadronic decay modes for wide p_T range, $0 < p_T < 13\text{GeV}/c$ for ω and $0 < p_T < 7\text{GeV}/c$ for ϕ , in p+p collisions at $\sqrt{s} = 200\text{GeV}$, as a function of p_T , respectively. The error bars of the cross section measured in hadronic decay modes show statistic uncertainties added in quadature with the systematic uncertainties.

The underlying physics for particle production at low p_T and high p_T is different. According to pQCD calculation as shown Section1.2, a pure power-law spectrum describes the high p_T region of particle spectra. A similarly good agreement is observed for π^0 with modified power-law function [92] :

$$E \frac{d^3\sigma}{dp^3} = A \left(1 + \frac{p_T}{b}\right)^{-n} \quad (4.1)$$

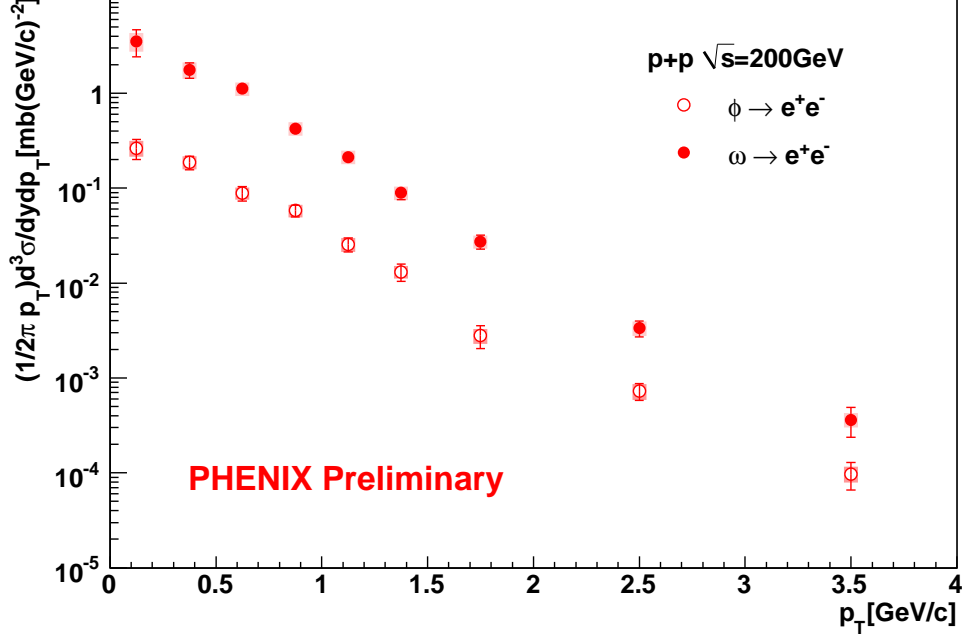


Figure 4.1: Invariant cross section of ω and ϕ production in $p + p$ collision at $\sqrt{s} = 200\text{GeV}$ measured in $\omega \rightarrow e^+e^-$ and $\phi \rightarrow e^+e^-$ decay channels as a function of p_T . Bars and boxes represent statistical and systematic errors, respectively.

where, A , b and the power n are the parameters of this function. However the power law is seen to fail in region below $p_T = 3\text{GeV}/c$. At low p_T region, where particle are largely produced in soft(thermal-like) process, the shape of the spectrum can be well described by:

$$E \frac{d^3\sigma}{dp^3} = \frac{1}{2\pi T^2} \frac{d\sigma}{dy} \exp^{-\frac{p_T}{T}} \quad (4.2)$$

where, $\frac{d\sigma}{dy}$ and the inverse slope parameter T are parameters of this function.

The Tsallis statistics extend Boltzman-Gibbs statistic [107]. The p_T spectra of particle production are well described by a Levy function based on Tsallis statistics:

$$E \frac{d^3\sigma}{dp^3} = \frac{1}{2\pi} \frac{d\sigma}{dy} \frac{(n-1)(n-2)}{(nT + m_0(n-1))(nT + m_0)} \left(\frac{nT + \sqrt{p_T^2 + m_0^2}}{nT + m_0} \right)^{-n} \quad (4.3)$$

where $\frac{d\sigma}{dy}$ is the integrated production cross section, m_0 is the rest mass corresponding to particle species, T is the inverse slope parameter, and n is the

related to power. All the parameters except m_0 are free parameters in fit. In the limiting case of $1/n \rightarrow inf$, the Levy function approached an exponential function. In the another limiting case of $m_0 \rightarrow 0$, the Levy function approached similar function of Eq.4.1.

The solid (red) curve in Figure 4.2,4.3 shows levy function fit to the both data measured in di-electron and hadronic decay modes in $0 < p_T < 13$ GeV/c for ω and $0 < p_T < 7$ GeV/c for ϕ . We also try to fit by modified power-law (Eq. 4.1) as shown the solid curve(green) which can well describe the data at higher p_T region above 3 GeV/c. In contrast, the exponential function as shown the dash curve(black) well describes the data at lower p_T region below 3 GeV /c. The ratio of data to levy fit are shown in bottom Fig. 4.2 and Fig. 4.3. The levy fit is in an good agreed with data in the wide p_T range.

The spectra measured via di-electron and hadronic decay modes are smoothly connected. It notes that there are only a few data points within overlap p_T range of $2.0 < P_T < 4.0$ GeV/c for ω production, since the p_T range in di-electron decay modes is limited by statistics at high p_T and the p_T range in hadronic decay modes is limited by decreasing detector acceptance and trigger efficiency at low p_T .

Comparison with PYTHIA

The PYTHIA event generator is frequently used for the description of high-energy hadron+hadron collisions. We have used PYTHIA version 6.421, with Tune A for in-elastic cross section and including preset for multiple parton scattering process [108]. In this setting, the Lund symmetric fragmentation function $D_Q^h(z, \mu^2)$ [109, 110] and Leading order Parton Distribution Function (CTEQ 5L) [3] is used. Fig. 4.4 and Fig.4.5 show the invariant cross section compared with PYTHIA for ω and ϕ meson, respectively. It is in a good agreement with data within experimental error.

4.2 Integrated cross sections

First measurement of the ω and ϕ measured in di-electron decay mode extend the p_T region to zero momentum and allow a direct calculation of the integrated cross section $d\sigma/dy$. The $d\sigma/dy$ was calculated by summing up the data points:

$$\frac{d\sigma}{dy} = 2\pi \sum_i \left(\frac{d\sigma_i}{dp_T dy} \times p_T^i \times \Delta p_T^i \right) \quad (4.4)$$

The statistic and systematic errors on the data points are added quadrature, respectively.

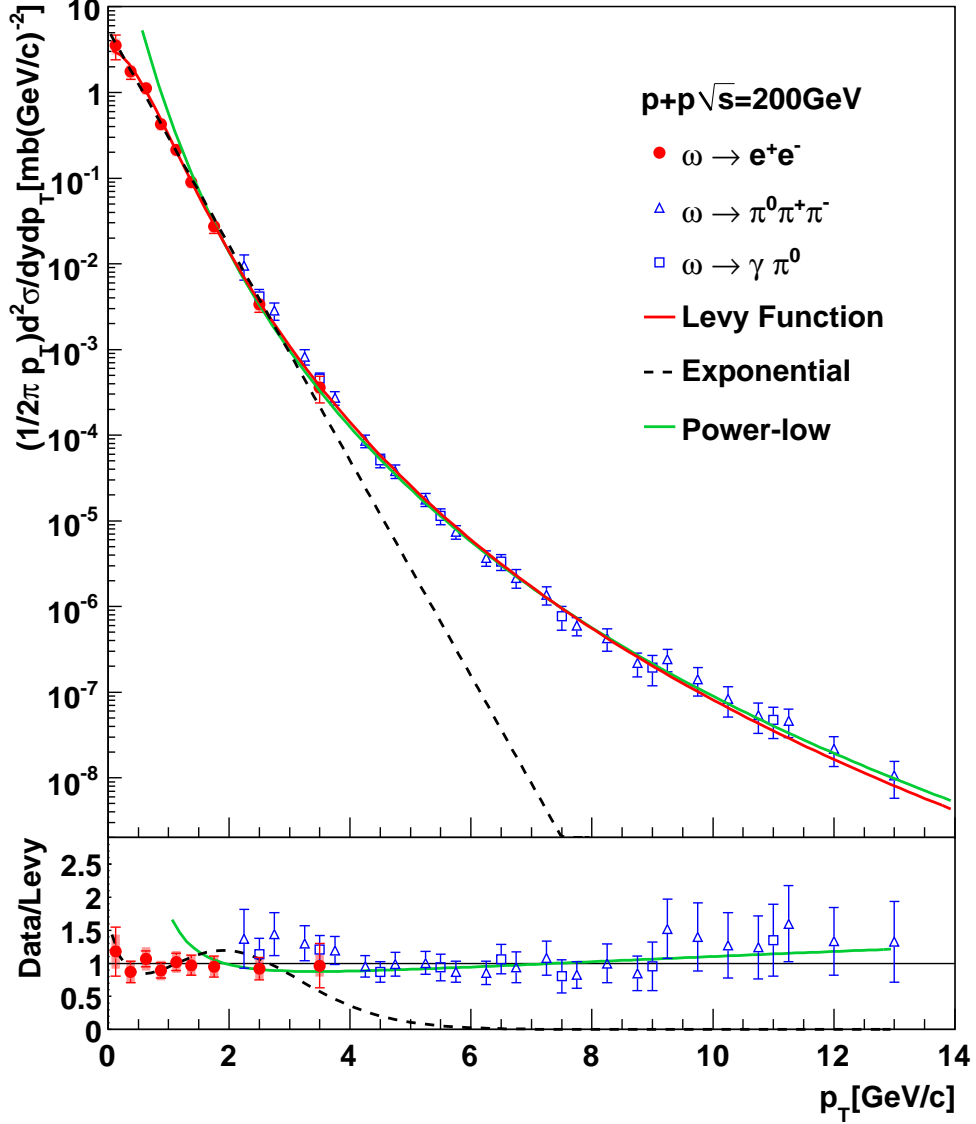


Figure 4.2: (Top) The invariant cross section of ω production in $p + p$ collision at $\sqrt{s} = 200 \text{ GeV}$ measured in $\omega \rightarrow e^+e^-$, $\pi^0\pi^+\pi^-$ and $\pi^0\gamma$ decay channels. The curves show Levy (red), modified Power-law (Green) and Exponential (black) fit to the data measured in both dilepton and hadronic decay modes. (Bottom) Ratio of the data and Levy fit.

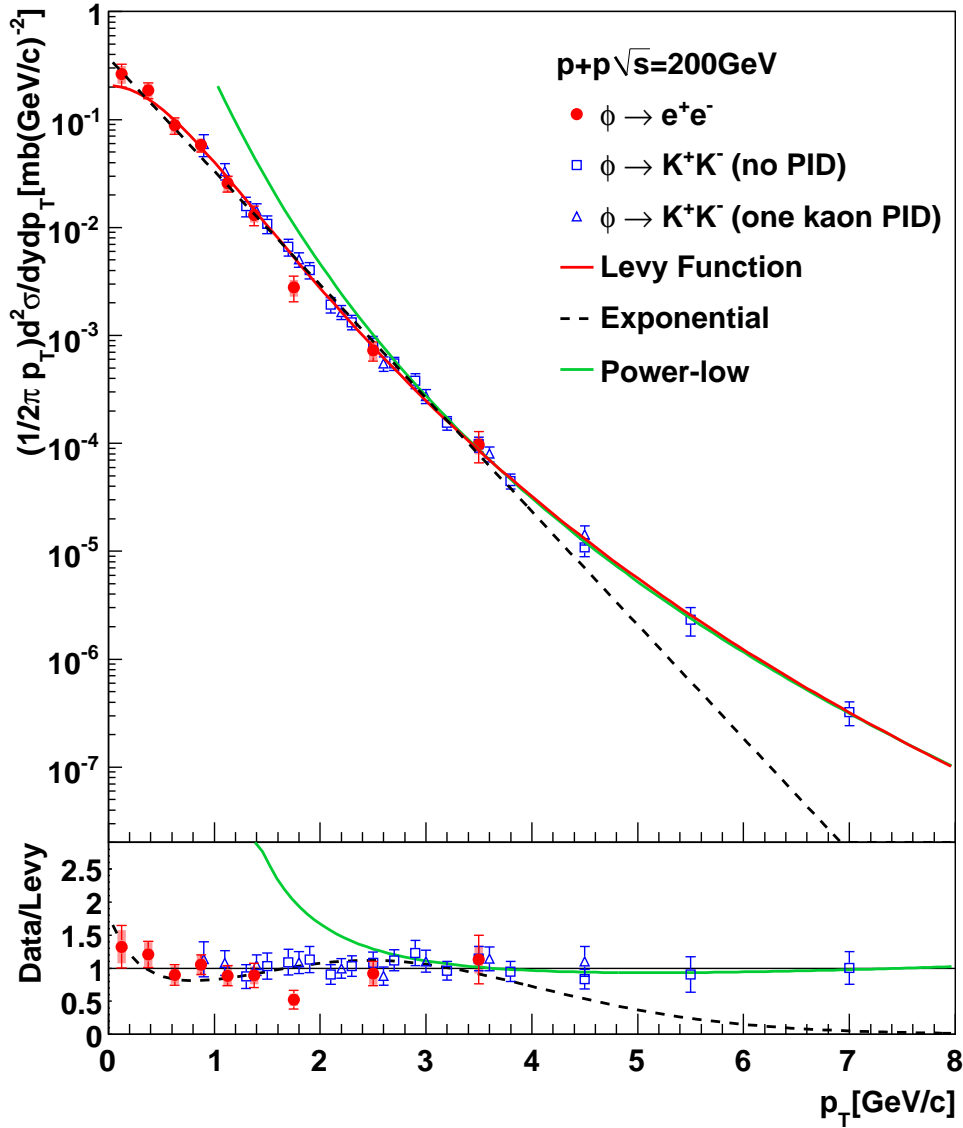


Figure 4.3: Invariant cross section of ϕ production in $p + p$ collision at $\sqrt{s}=200\text{GeV}$ measured in $\phi \rightarrow e^+e^-$, K^+K^- decay channels. The curves show Levy(red), modified Power-law(Green) and Exponential(black) fit to the data measured in both dilepton and hadronic decay modes. (Bottom)Ratio of the data and Levy fit.

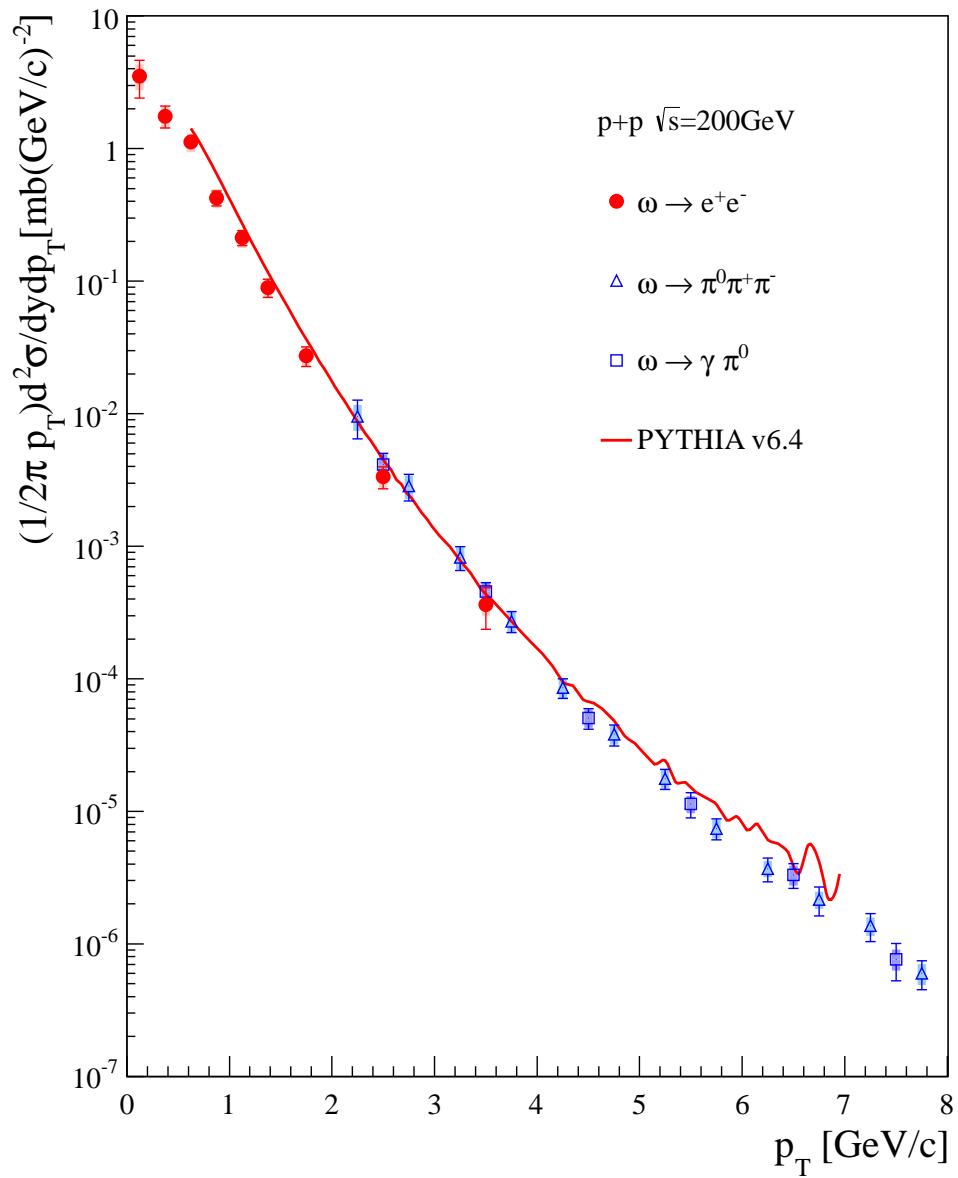


Figure 4.4: The invariant cross section of ω production in $p + p$ collision at $\sqrt{s}=200\text{GeV}$ compared with PYTHIA version 6.421 with Tune A.

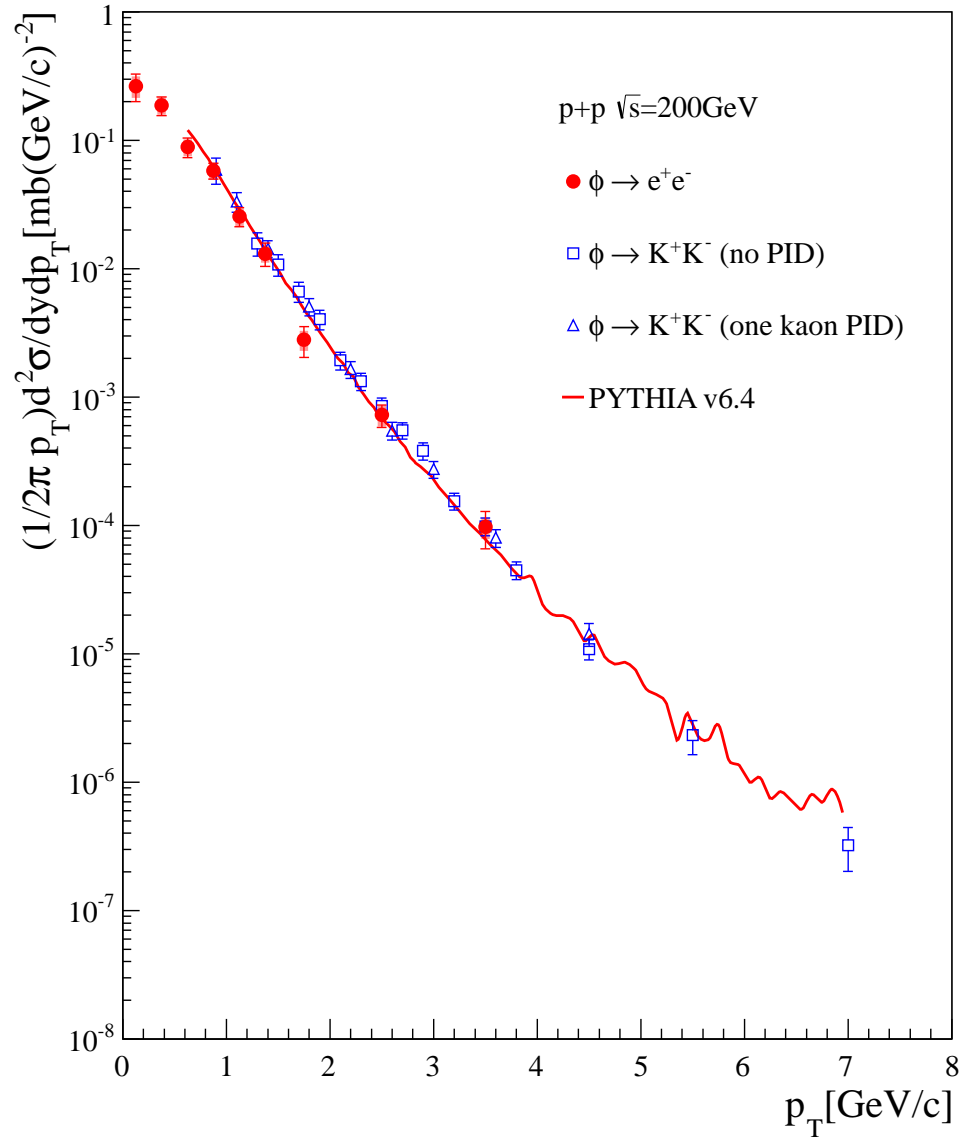


Figure 4.5: Invariant cross section of ϕ production in $p + p$ collision at $\sqrt{s}=200\text{GeV}$ compare with PYTHIA version 6.421 with Tune A.

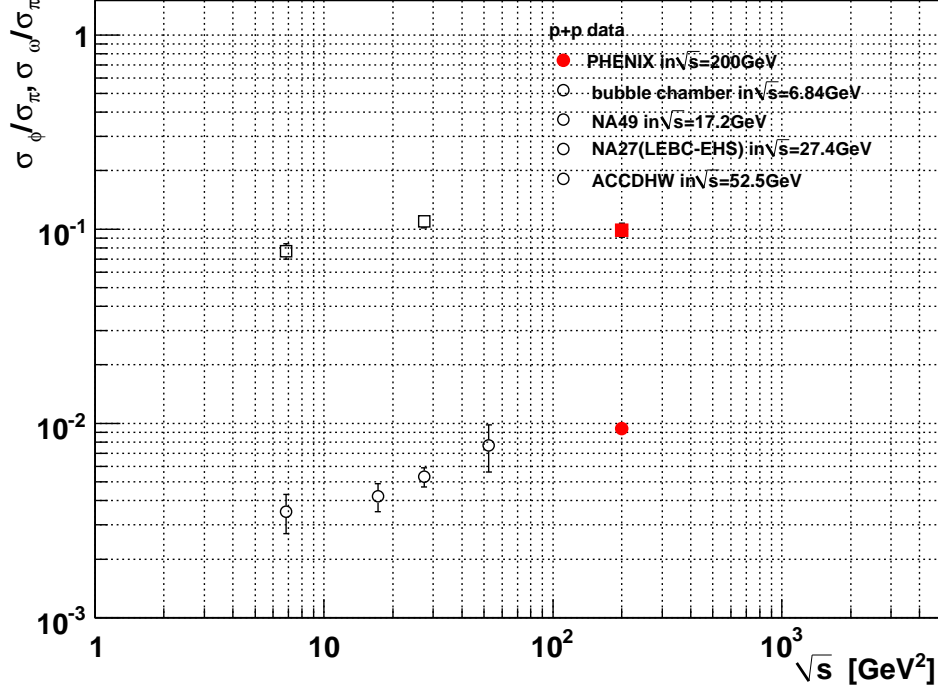


Figure 4.6: Ratio of cross section, σ_ω/σ_π (square) and σ_ϕ/σ_π (circle), measured for $p + p$ data as a function of center-of-mass energy.

The results for ω and ϕ are $d\sigma^\omega/dy = 4.19 \pm 0.33^{stat.} \pm 0.33^{sys.}$ mb and $d\sigma^\phi/dy = 0.431 \pm 0.031^{stat.} \pm 0.028^{sys.}$ mb which are consistent with one obtained by Levy fit within statistic error. The results are summarized in Table 4.1.

	Function	Fit range[GeV/c]	$d\sigma/dy$ [mb]	n	χ^2/NDF
$\phi \rightarrow ee$ & KK	Summing		$0.431 \pm 0.031 \pm 0.028$	—	—
	Levy	$0 < p_T < 7.0$	0.430 ± 0.035	11.0 ± 1.1	$19.0/29$
	exponential	$0 < p_T < 4.0$	0.400 ± 0.028	—	$26.7/27$
	power-law	$3 < p_T < 7.0$	—	9.8 ± 0.5	$2.8/6$
$\phi \rightarrow ee$	Levy		0.419 ± 0.063	6.5 ± 1.9	$3.1/4$
	exponential	$0.5 < p_T < 4.0$ (Overlap region)	0.418 ± 0.063	—	$7.3/5$
	power-law		—	6.7 ± 0.3	$6.8/4$
	Levy		0.454 ± 0.071	10.5 ± 2.1	$6.3/17$
$\phi \rightarrow KK$	exponential	$0.5 < p_T < 4.0$ (Overlap region)	0.402 ± 0.038	—	$15.0/18$
	power-law		—	7.8 ± 0.1	$21.7/17$
	Function	Fit range[GeV/c]	$d\sigma/dy$	n	χ^2/NDF
$\omega \rightarrow ee$ & $\pi^0\gamma$ & $\pi^0\pi\pi$	Summing		$4.19 \pm 0.33 \pm 0.33$	—	—
	Levy	$0 < p_T < 13.0$	4.23 ± 0.41	9.7 ± 0.4	$16.7/35$
	exponential	$0.5 < p_T < 3.0$	4.05 ± 0.55	—	$5.6/7$
	pow-law	$4.0 < p_T < 13.0$	—	9.2 ± 0.2	$6.1/20$
$\omega \rightarrow ee$	Levy	$0 < p_T < 4.0$ (Full range)	4.12 ± 0.45	9.6 ± 2.6	$0.9/6$
	exponential	$0.5 < p_T < 3.0$	4.48 ± 0.64	—	$1.0/4$
$\omega \rightarrow \pi^0\gamma$ & $\pi^0\pi\pi$	Levy	$2.0 < p_T < 13.0$ (Full range)	36.64 ± 39.20	8.3 ± 0.5	$8.5/26$
	pow-law	$4.0 < p_T < 13.0$	—	8.1 ± 0.2	$5.0/20$

Table 4.1: Summary of fitting parameters

4.3 particle ratio of ω and ϕ to π

The distributions of the particle ratios for ω/π and ϕ/π as a function of p_T in $p + p$ collision at $\sqrt{s} = 200\text{GeV}$ were shown Fig.4.7 and 4.8, respectively. The π meson yields were obtained by Tsallis fit results to $(\pi^+ + \pi^-)/2$ and π^0 spectra measured by PHENIX [95,102]. In high p_T region, $p_T > 3 \text{ GeV}/c$, they were constant of $\omega/\pi = 0.79 \pm 0.04^{stat.}$ and $\phi/\pi = 0.023 \pm 0.007^{stat.}$. It means that these mesons have same power n of power law function. This implied that the fragmentation functions to the mesons were same and it is consistent picture with pQCD expectation.

4.4 Scaling properties

The invariant cross section of K^\pm , K_s^0 , η and J/ψ meson in $p+p$ collision at $\sqrt{s} = 200\text{GeV}$ are also measured by PHENIX experiment [94,103–106]. The spectra of invariant differential cross section for $(\pi^+ + \pi^-)/2$, π^0 , $(K^+ + K^-)/2$, K_s^0 , η , ω , ϕ and J/ψ mesons as a function of p_T is shown in Fig.4.9. The fit of the Tsallis distribution to the spectra for each particles were shown as dash lines in Fig.4.9. This function consists only 2 parameters, since the m_0 is fixed to the mass corresponding to particle species. Nevertheless, the Tsallis function can describe the spectra of various particle species with masses are 0.1 to $3 \text{ GeV}/c^2$.

The Fig.4.10 shows the spectra of all measured mesons normalized to π_0 at $p_T = 6 \text{ GeV}/c$. The solid line show pure power law function fit into the range of $5 < p_T < 20 \text{ GeV}/c$ for all points. According to pQCD calculation, the power law behavior represented at high p_T region and this results consistent with pQCD picture.

In addition, the spectra of $(\pi^+ + \pi^-)/2$, π^0 , $(K^+ + K^-)/2$, K_s^0 , η , ω , ϕ and J/ψ as a function of transverse mass, $m_T (= \sqrt{p_T^2 + m_0^2})$, in $p + p$ collision at $\sqrt{s} = 200\text{GeV}$ were shown in Fig.4.11. The bottom figure shows the ratio of these spectra to Tsallis functional form fit into π meson spectrum. The ratio is approximately constant and it means that the spectra shape as a function of m_T for all particle species are very similar.

Fig.4.12 shows m_T spectra for all mesons normalized at one point of $p_T = 10 \text{ GeV}/c$. It is clear that the spectra shape for all particles are very similar forms for wide m_T region when plotted as a function of m_T . The Eq.4.3 can be expressed for transverse mass as follow:

$$E \frac{d^3\sigma}{dp^3} = \frac{1}{2\pi} \frac{d\sigma}{dy} \frac{(n-1)(n-2)}{(nT + m_0(n-1)(nT + m_0))} \left(\frac{nT + m_T}{nT + m_0} \right)^{-n} \quad (4.5)$$

In the limit of $m_0 \rightarrow 0$ Eq.4.6 becomes

$$E \frac{d^3\sigma}{dp^3} = \frac{1}{2\pi} \frac{d\sigma}{dy} \frac{(n-1)(n-2)}{(nT)^2} \left(1 + \frac{m_T}{nT}\right)^{-n}. \quad (4.6)$$

This form is very similar to expression inspired by QCD called Hagedorn formula [111] used fits to experimental data with success [112,113]. In this case, the form was written as a function of m_T instead of p_T . All the normalized points for all particles were fit simultaneously with Eq.4.6 and follows m_T scaling well as $\sqrt{s} = 200$ GeV.

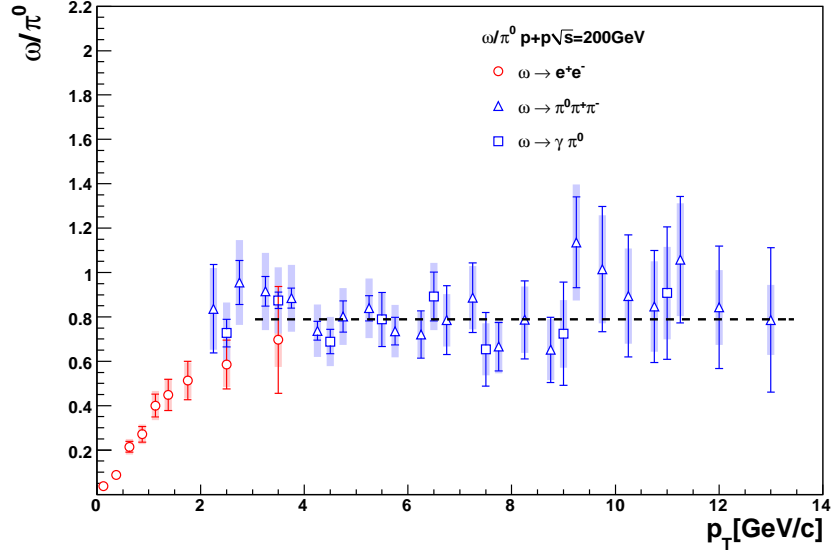


Figure 4.7: Measured ω/π^0 as a function of p_T in p+p collisions at $\sqrt{s} = 200$ GeV. Straight lines show fits to a constant for $2 < p_T < 3$ GeV/c

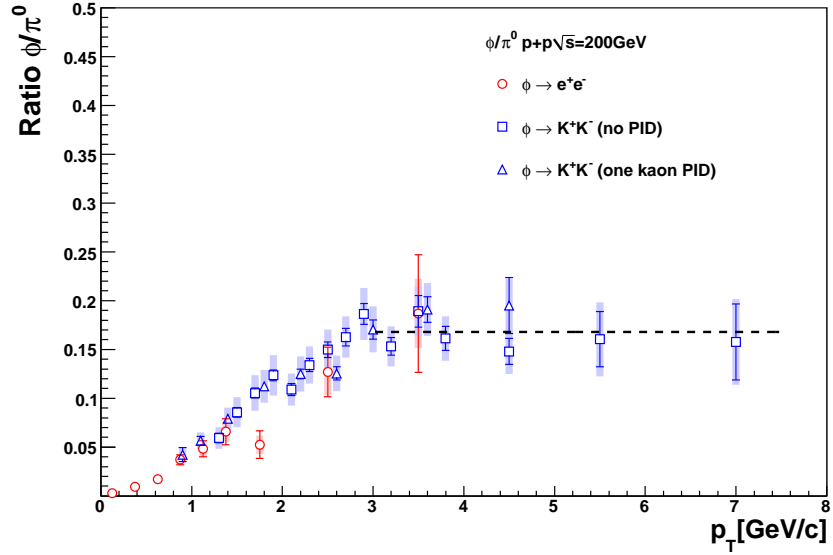


Figure 4.8: Measured ϕ/π^0 as a function of p_T in p+p collisions at $\sqrt{s} = 200$ GeV. Straight lines show fits to a constant for $3 < p_T < 7$ GeV/c

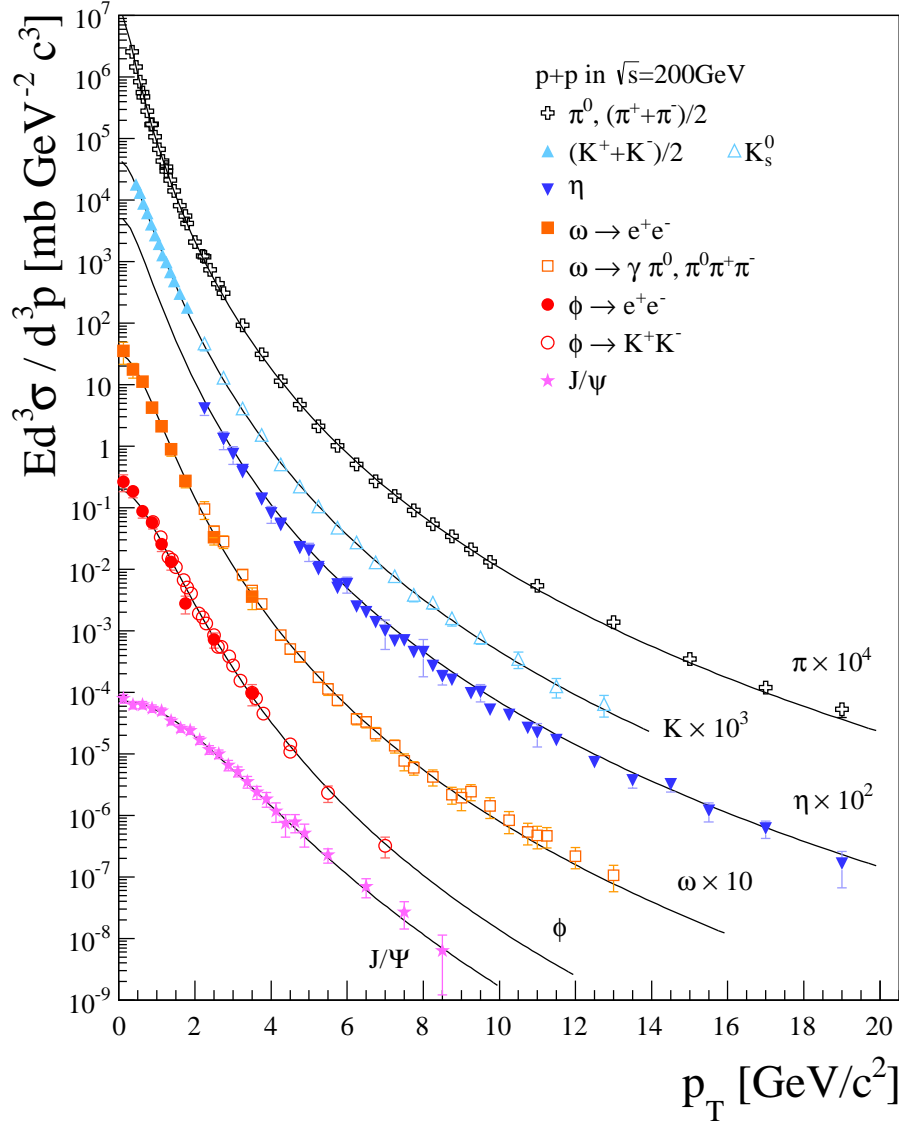


Figure 4.9: Spectra of invariant differential cross section as a function of p_T for $(\pi^+ + \pi^-)/2$, π^0 , $(K^+ + K^-)/2$, K_s^0 , η , ω , ϕ and J/ψ in $p + p$ collision at $\sqrt{s}=200\text{ GeV}$ at mid-rapidity.

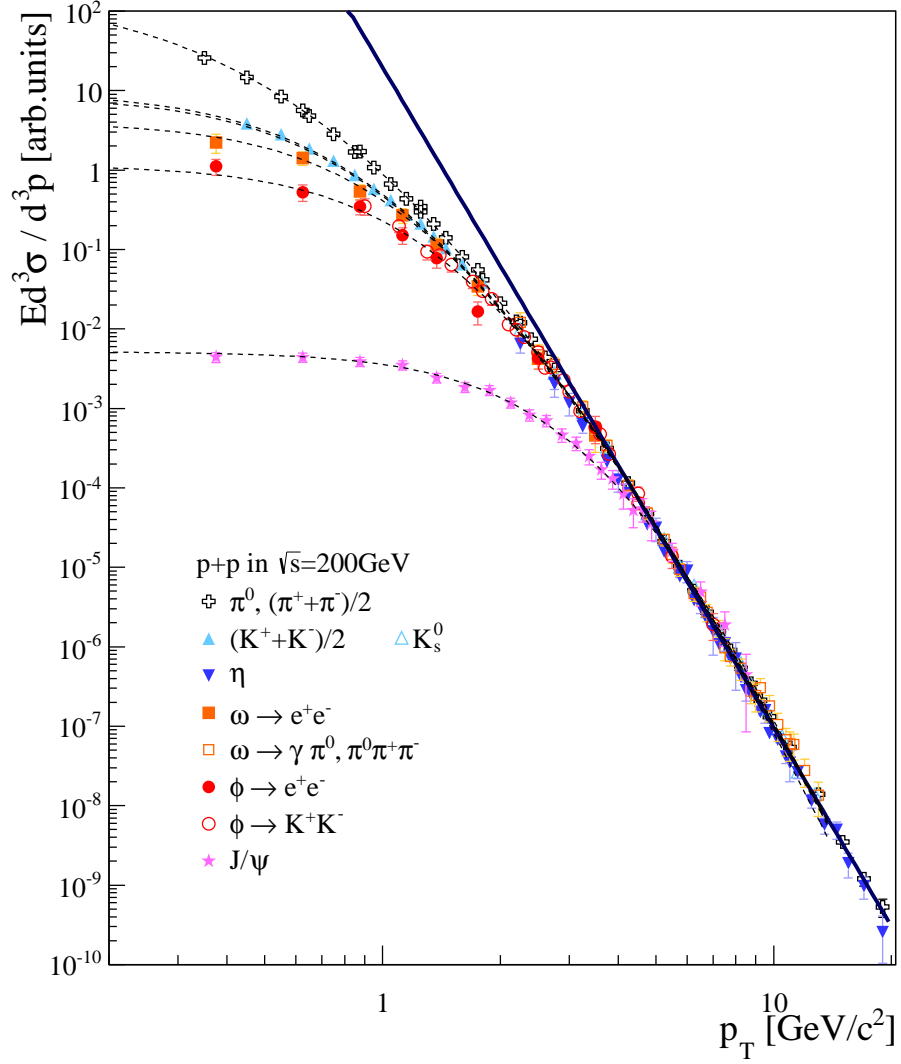


Figure 4.10: Scaled spectra of invariant differential cross section as a function of p_T for $(\pi^+ + \pi^-)/2$, π^0 , $(K^+ + K^-)/2$, K_s^0 , η , ω , ϕ and J/ψ in $p+p$ collision at $\sqrt{s}=200\text{GeV}$ at mid-rapidity. Solid line expressed pure power law function fitted in $5.0 < p_T < 20\text{GeV}/c$.

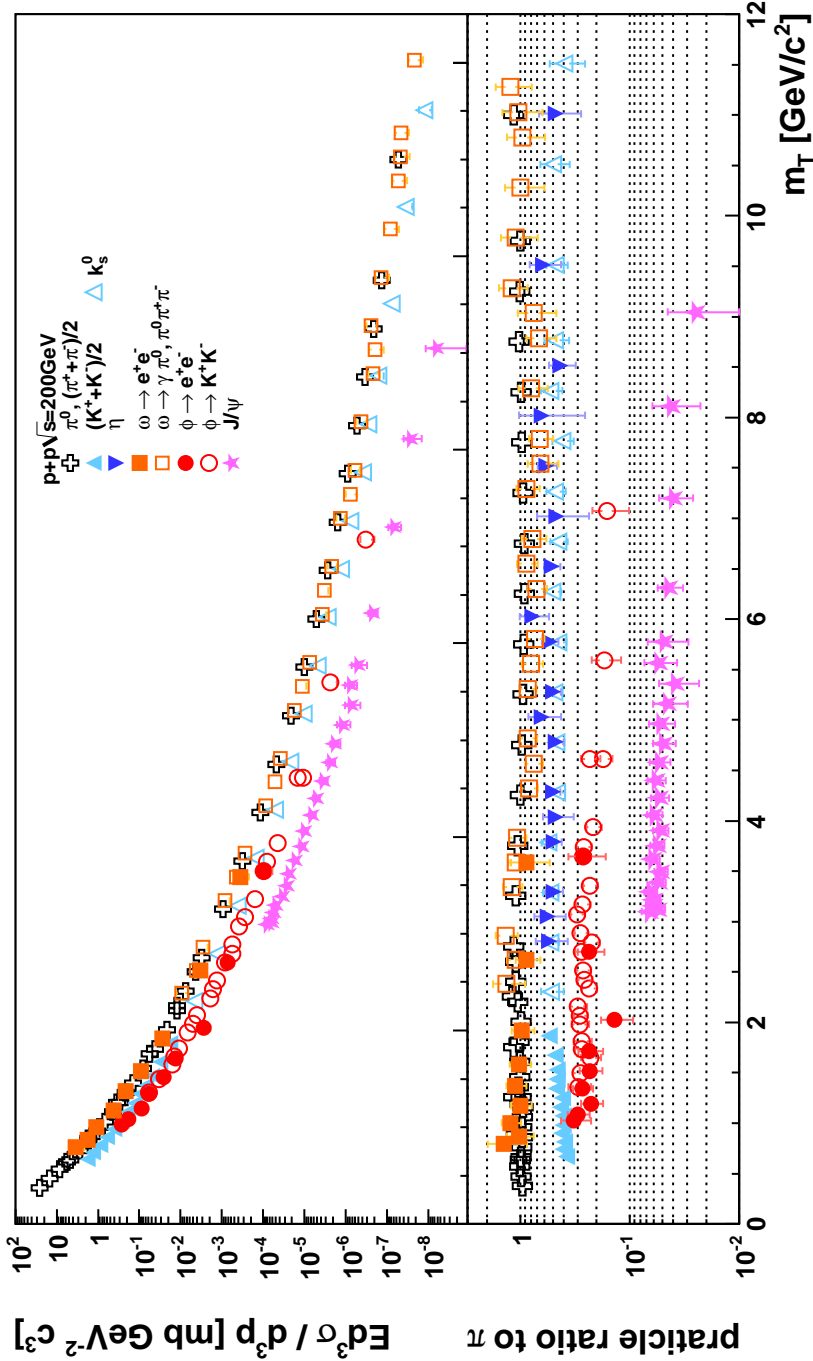


Figure 4.11: (top) m_T spectra for $(\pi^+ + \pi^-)/2$, π^0 , $(K^+ + K^-)/2$, K_s^0 , η , ω , ϕ and J/ψ in $p + p$ collision at $\sqrt{s}=200\text{GeV}$ at mid-rapidity. (Bottom) The ratio of the spectra to Levy fit to π . Bars show uncertainties combined with statistical and systematic errors.

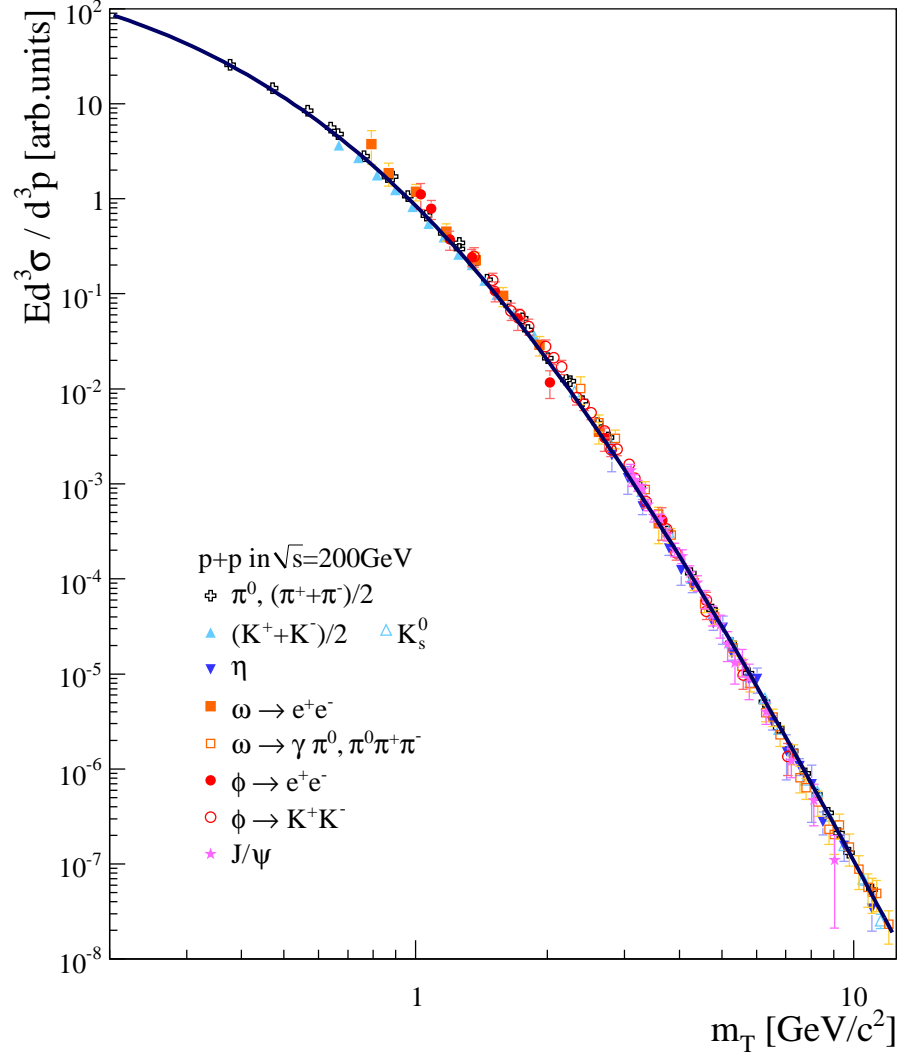


Figure 4.12: Scaled m_T spectra for $(\pi^+ + \pi^-)/2$, π^0 , $(K^+ + K^-)/2$, K_s^0 , η , ω , ϕ and J/ψ in $p + p$ collision at $\sqrt{s}=200\text{GeV}$ at mid-rapidity.

4.5 Mass line shape analysis

Due to the chiral symmetry restoration in the hot matter created by the high energy heavy ions collisions, the possible observation of mass modification of ω and ϕ mesons are expected. On the other hand, the observation of the mass modification is not expected in case of $p+p$ collisions, since the matter created by $p+p$ collisions should be much smaller than the life time of these mesons. The analyzing invariant mass distribution in $p+p$ collisions provides crucial baseline for challenging studies for measurement of ω and ϕ meson mass spectra due to the huge combinatorial background in heavy ion collisions.

The model of this analysis consists two parameters to consider mass shift quantitatively. Then one of the parameters, Δ were defined as the ratio how much center of mass were shifted:

$$M' = (1 + \Delta)M \quad (4.7)$$

If Δ equal to zero, it means no mass shift was observed. In the assumption of that the temperature of hot medium is stable, the Δ should be constant since the modification depend on temperature. Then, if the mesons decayed inside the medium, the position of center of reconstructed mass peak should be M' .

In addition, another parameter as the fraction of the meson yield decaying inside medium was defined as R ;

$$R = \frac{\text{Yield}|_{\text{decay inside medium}}}{\text{Yield}|_{\text{total}}} \quad (4.8)$$

where R is in the range of 0 to 1. We assumed that R depends $1/\beta\gamma$ corresponding to that the decay probability inside medium increase as moving slower.

Then, the total invariant mass spectra for the vector mesons represent as follows;

$$F(m_{ee}) = A \times (R \times f' + (1 - R) \times f) \quad (4.9)$$

Here

$$f(m_{ee}) = \text{Gaussian convoluted (r.BW + radiative tail)} \quad (4.10)$$

$$f'(m_{ee})|_{\text{mod}} = \text{Gaussian convoluted (r.BW + radiative tail)} \quad (4.11)$$

where A is normalization factor, $f'(m_{ee})|_{\text{mod}}$ represents mass spectra fully including mass shift as shown Eq.4.7. The center of mass and natural width Γ were fixed to PDG value as shown Table3.2. The ρ meson contamination

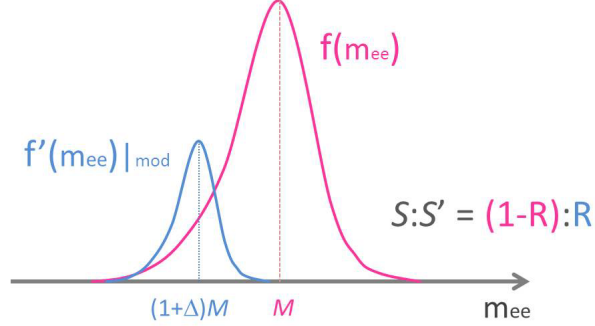


Figure 4.13: Schematic representation of the model to evaluate mass spectra with mass shift. The shapes of $f(m_{ee})$ and $f'(m_{ee})$ represent the measured spectra of vector meson decaying outside and inside medium, respectively.

into the mass spectra of ω meson was considered. The ratio of ω/ρ was fixed to 1.35 determined by their e^+e^- decay branching ratio in vacuum with the assumption of the ratio of the total production yield $\sigma_\rho/\sigma_\omega = 1.15$, consistent with jet fragmentation [89].

The invariant mass distribution reconstructed via e^+e^- in $p+p$ collisions analyzed by the function $F(m_{ee})$ were shown in Fig.4.14 and Fig.4.17 for ω and ϕ mesons, respectively. The invariant mass distributions were divided by three p_T binning correspond to the weighted average of $\langle\beta\gamma\rangle = 1.01, 2.04, 4.85$ and $\langle\beta\gamma\rangle = 0.74, 1.82, 3.68$ for ω and ϕ mesons, respectively. In the figures, the blue line shows $F(m_{ee})$, the magenta and light blue line correspond to f and f' , respectively. The dash line shows the fit result in case of $\Delta = 1$ and $R = 0$. And the green line shows contribution of ρ meson.

The best fit value of Δ and R were obtained as the result of global fit into the invariant mass distribution for these three p_T binning. In addition, statistical errors of Δ and R were estimated by χ^2 distribution as shown in Fig. 4.15 and Fig. 4.18 for ω and ϕ mesons, respectively. The best fit value for Δ and R with statistical errors were $\Delta = -3.3^{+2.4}_{-3.8} \%$, $R = 7.5^{+4.9}_{-4.9} \%$ for ω meson and $\Delta = -1.2^{+0.9}_{-0.8} \%$, $R = 9.7^{+8.0}_{-8.0} \%$ for ϕ meson. The χ^2 distributions for 2-dimensional space of Δ and R were shown in Fig.4.16 and Fig.4.19 for ω and ϕ mesons. The red points are the best fit value and the bars show statistic errors for Δ and R . If there were no mass shift, the parameters of Δ and R should be $\Delta = 0$ and/or $R = 0$. The obtained results including error are close to the $\Delta = 0$ and/or $R = 0$. The results for ω and ϕ mesons are consistent with assumption that no mass shift was observed in $p+p$ collisions within 1.4σ , respectively.

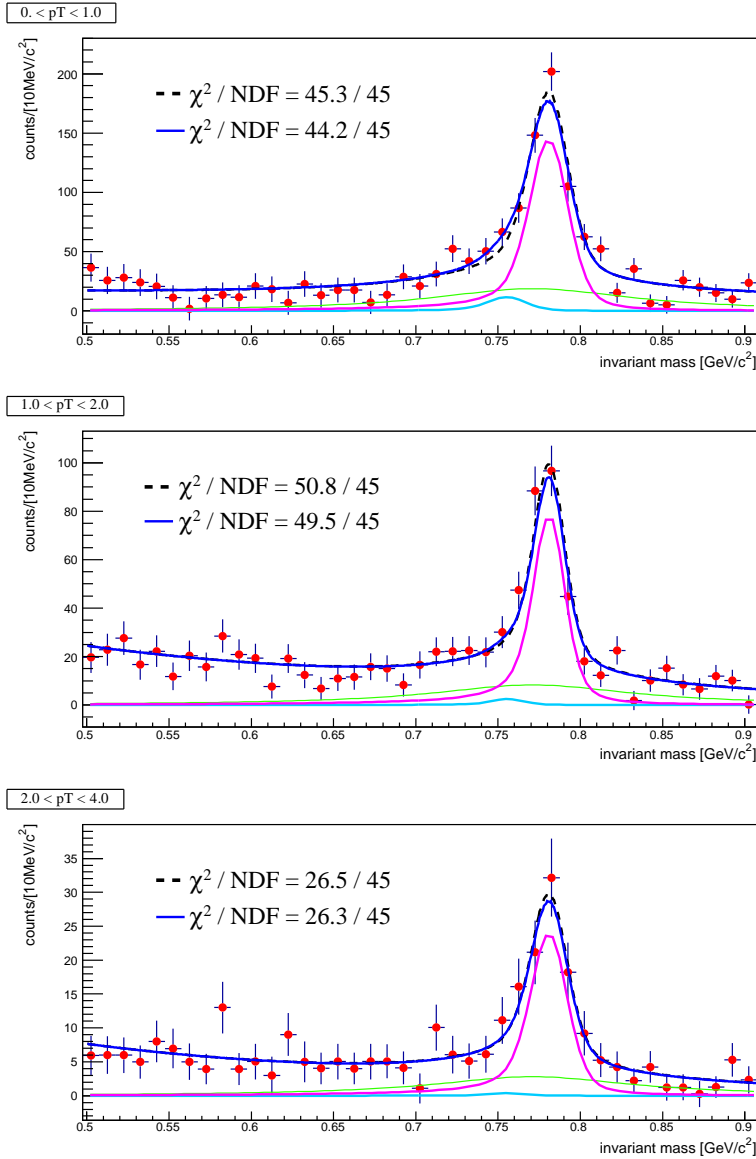


Figure 4.14: Invariant mass distribution with fitting results for ω mesons for three p_T bins corresponding to the weighted average of $\langle\beta\gamma\rangle = 1.01, 2.04, 4.85$. Blue line shows $F(m_{ee})$, magenta and light blue line correspond to f and f' , respectively. The dash line shows the fit result with $\Delta = 0$ and $R = 0$. The green line shows ρ meson contribution.

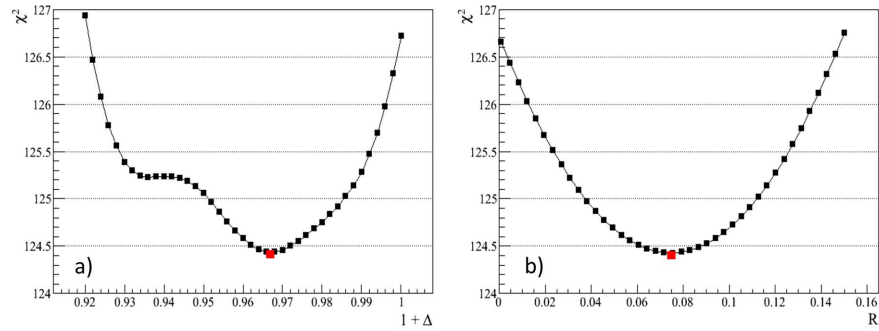


Figure 4.15: a) and b) show χ^2 distribution as a function of $(1+\Delta)$ and R for ω meson, respectively. The red points are best fit value.

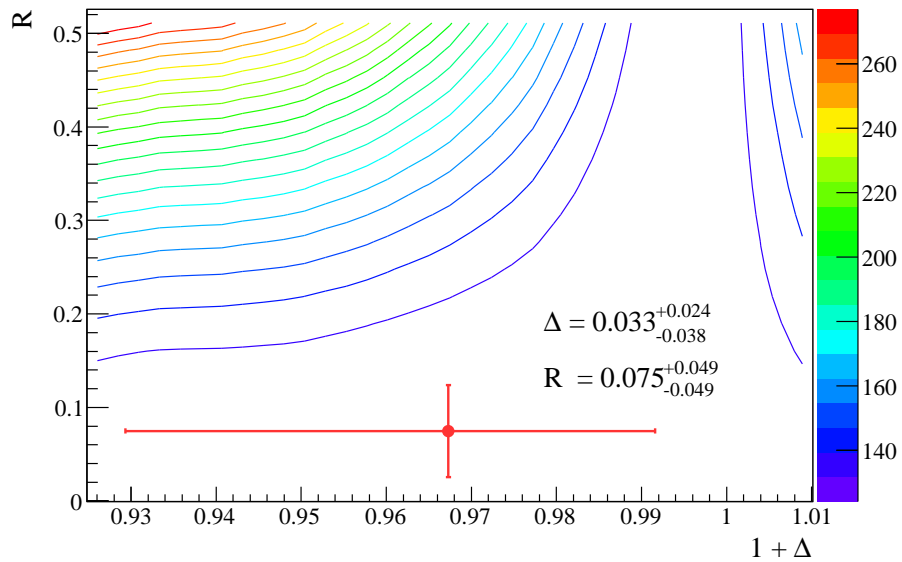


Figure 4.16: χ^2 distribution in 2-dimensional space for $(1 + \Delta)$ and R for ω meson. The red point is best fit value and the bars are statistical errors corresponding to $\Delta\chi^2 = +1$

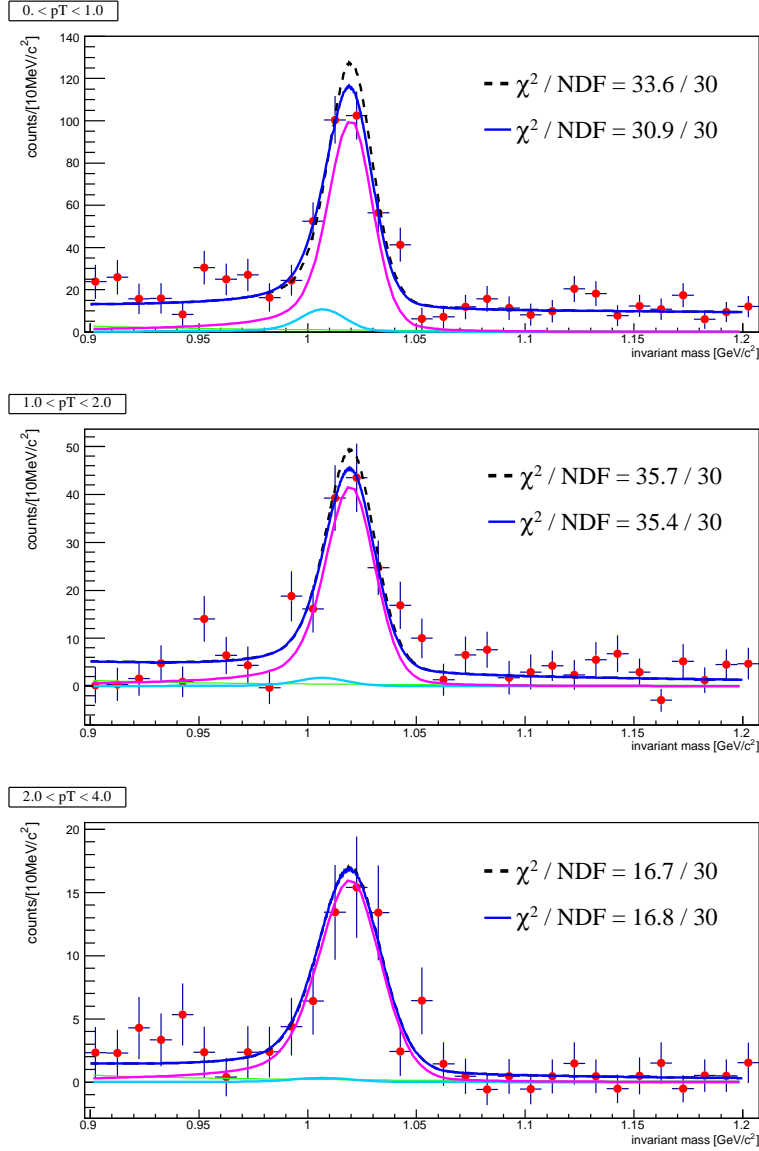


Figure 4.17: Invariant mass distribution with fitting results for ω mesons for three p_T bins corresponding to weighted average of $\langle\beta\gamma\rangle = 0.74, 1.82, 3.68$. Blue line shows $F(m_{ee})$, magenta and light blue line correspond to f and f' , respectively. The dash line shows the fit result with $\Delta = 0$ and $R = 0$. The green line shows ρ meson contribution.

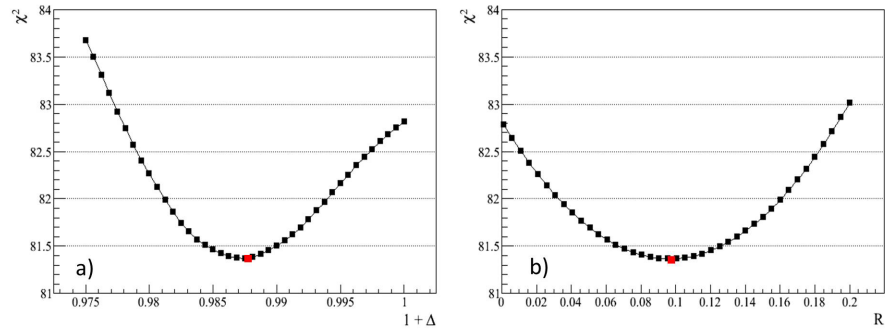


Figure 4.18: a) and b) show χ^2 distribution as a function of $(1 + \Delta)$ and R for ϕ meson, respectively. The red points are best fit value.

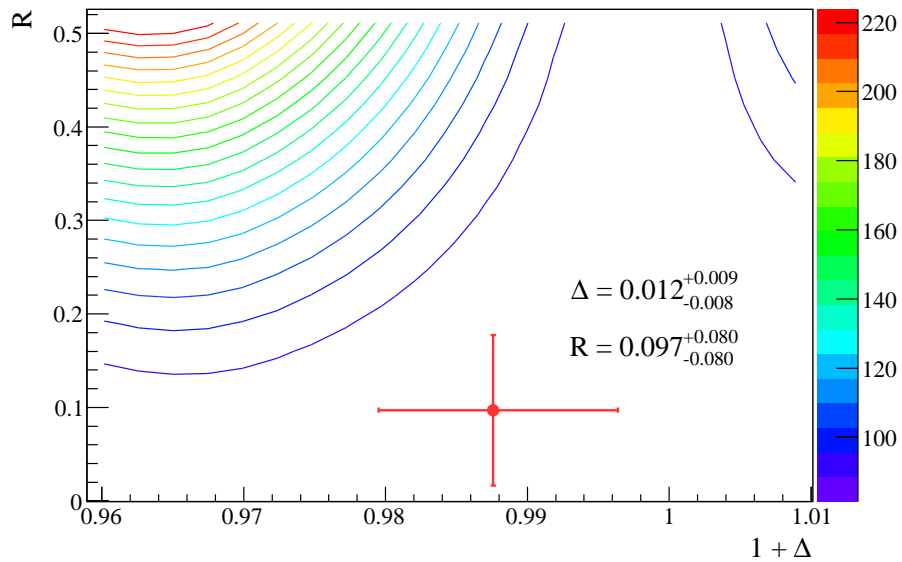


Figure 4.19: χ^2 distribution in 2-dimensional space for $(1 + \Delta)$ and R for ϕ meson. The red point is best fit value and the bars are statistical errors corresponding to $\Delta\chi^2 = +1$

Chapter 5

Summary and Conclusions

We have measured spectra of differential cross sections of ω and ϕ mesons as a function of transverse momentum in the range of $0 < p_T < 4$ GeV/ c . We analyzed data sample representing a total integrated luminosity of $3.8pb^{-1}$ accumulated by the PHENIX experiment in year 2004/2005 in $p+p$ collision at $\sqrt{s} = 200$ GeV.

The ω and ϕ were identified from invariant mass spectra reconstructed by electron and positron pairs identified from large background of hadrons. The yield of ω and ϕ were statistically subtracted from large amount of background which comes from combinatorial pairs mainly due to π^0 Dalitz decay, photon conversion and other hadron decay. After applying correction for geometrical acceptance of PHENIX detector, electron identification efficiency, trigger efficiency obtained by simulation based on GEANT, the cross section of ω and ϕ meson be obtained.

Measurements of ω and ϕ vis di-electron decay mode in $p+p$ collisions at $\sqrt{s} = 200GeV$ extend the p_T coverage to zero and allows direct calculation of the integrated cross section $d\sigma^\omega/dy = 4.19 \pm 0.33^{stat.} \pm 0.33^{sys.}$ mb and $d\sigma^\phi/dy = 0.431 \pm 0.031^{stat.} \pm 0.028^{sys.}$ mb.

The spectra of invariant cross sections of ω and ϕ were measured in wide p_T ranges, $0 < p_T < 13$ GeV/ c for ω and $0 < p_T < 7$ GeV/ c for ϕ utilizing both of di-electron and hadronic decay modes. The spectra measured in di-electron and hadronic decay modes are smoothly connected within overlap p_T range. There were described by the Tsallis distributions which represent an exponential shape at low p_T and power law shape at high p_T . The measured spectra is in a good agreement with results of an event generator PYTHIA based on perturbative Quantum Chromodynamics(pQCD) calculations.

The particle ratios ω/π and ϕ/π were constant in the high p_T region of $p_T > 3GeV/c$. The results of a fit to a constant are $\omega/\pi = 0.79 \pm 0.04^{stat.}$ and $\phi/\pi = 0.023 \pm 0.007^{stat.}$.

The Tsallis distribution with parameters of T and n described various meson spectra $(\pi^+ + \pi^-)/2$, π^0 , $(K^+ + K^-)/2$, K_s^0 , η , ω , ϕ and J/ψ measured by PHENIX for wide p_T range. Having same power n for all mesons implied that the fragmentation functions to the mesons were same and it is consistent picture with pQCD expectation. The m_T spectra of $(\pi^+ + \pi^-)/2$, π^0 , $(K^+ + K^-)/2$, K_s^0 , η , ω , ϕ and J/ψ were presented. The spectra shape for all particle species were similar for wide m_T region in spite of that its contained both production process of soft and hard. Thesis scaling results suggest a similar production mechanism of mesons in $p+p$ collisions at $\sqrt{s} = 200$ GeV. . By using the model of this analysis for evaluating mass modification, two parameters corresponding to the ratio of mass shift Δ and the fraction of modified meson yield R were estimated, and the best value were $\Delta = -3.3^{+2.4}_{-3.8}$ %, $R = 7.5^{+4.9}_{-4.9}$ % for ω meson and $\Delta = -1.2^{+0.9}_{-0.8}$ %, $R = 9.7^{+8.0}_{-8.0}$ % for ϕ meson. The results for ω and ϕ mesons are consistent with assumption that no mass shift was observed in $p+p$ collisions within 1.4σ , respectively. The baseline for study of mass modification in heavy ion interactions was provided by considering the procedure to evaluate measured mass spectra in $p+p$ collisions.

We conclude that the these results for ω and ϕ meson production in $p+p$ provided a crucial data as a solid baseline to understand physics of heavy ion interactions.

Acknowledgment

I would like to thank Prof. T. Sugitate for his continuous guidance, constructive comment and his work as the leader of our laboratory in Hiroshima University and PHENIX BBC subsystem group. I would like to express my sincere gratitude to my supervisor Prof. K. Shigaki for giving me an long-standing and continuous guidance, support and for all the opportunities he has provided for my studies. I could not have done this work without his support. I would like to appreciate Dr. K. Homma for providing interesting physics theme for not only high energy nuclear physics and his many thoughtful comments, suggestion and also his work for PHENIX BBC subsystem group.

I deeply acknowledge Dr. K. Ozawa and Prof. S. Esumi for their works on the financial supports of PHENIX-J. In addition, I wish to also thank Dr. K. Ozawa for his advice on research. I could not start the di-electron analysis without his help. I appreciate chief scientist Dr. H. En'yo for giving financial support to attend international conference.

I would like to acknowledge all PHENIX collaboration. I have had a lot of supports from PHENIX spokesperson, Prof. W. A. Zajc and Prof. B. V. Jacak and paper preparation group, Dr. A. Milov, Dr. Y. Riabov, Dr. V. Riabov, Dr. D. Ivanishchev, Dr. M. Naglis, Dr. A. Toia, Dr. D. Morrison. I am very thank to Prof. R. Seto and Dr. D. Sharma for providing the opportunity to discuss and their help for my analysis.

I would like to thank Mr. Y. Nakamiya, Ms. M. Ouchida, Mr. D. Watanabe, Mr. M. Nihashi for working together for the BBC operation and maintenance. With their help, I could face difficulties and enjoy working and discussion. In addition, I offer warm thanks to Yoshihide for his help and support with daily tasks, issues and in not only research as well. I also appreciate Dr. J. S. Haggerty, Dr. C. Y. Chi, Dr. S. Bathe, Dr. S. Stoll, Dr. M. Chiu for their cooperation of the BBC operation. We could not provide data by BBC without their help. I would like to express deep thank for Dr. Y. Akiba, Dr. T. Sakaguchi, Dr. K. Okada, Dr. I. Nakagawa. I would like to thanks to Dr. H. Torii, Dr. T. Horaguchi, Dr. T. Hachiya, Dr. M. Hachiya,

Dr. H. Masui Dr. A. Enokizono, Dr. M. Konno, Dr. T. Gunji, Dr. T. Isobe, Dr. M. Togawa, Dr. Y. Fukao, Dr. Y. Morino, Dr. K. Miki, Dr. Y. Yamaguchi, Dr. Y. Aramaki, Mr. Y. Ikeda, Mr. K. Watanabe, Mr. M. Sano, Mr. T. Todoroki. I had a very good time to discuss and to talk with them. I wish to thank Dr. K. Kondo, Dr. T. Kanetsue, Dr. K. Karatsu, Mr. K. Nakamura, Mr. K. Watanabe for the great time we spend together at BNL. I could really enjoy BNL life.

I would also like to thank all the member of quark physics laboratory at Hiroshima University, Dr. H. Harada, Mr. K. Haruna, Mr. H. Sakata, Mr. K. Hosokawa, Mr. K. Yamaura, Mr. K. Kubo, Mr. T. Narita, Mr. K. Kadowaki, Mr. K. Mizoguchi, Mr. Y. Iwanaga, Mr. Y. Okada, Mr. Y. Maruyama, Mr. F. Chuman, Ms. A. Hiei, Mr. Iwasaki, Mr. H. Sakaguchi, Mr. M. Saka, Ms. T. Yamamoto, Mr. J. Midori, Mr. H. Obayashi, Mr. T. Hiasa, Mr. S. Yano, Mr. T. Hoshino, Mr. S. Sakurai, Mr. K. Kume, Mr. D. Sato, Mr. T. Hasebe, Ms. A. Tuji, Mr. T. Okubo. I would like to acknowledge Dr. T. Nakamura and Mr. Y. Tsuchimoto. I could learn many techniques of the experiments and analysis from them and could enjoy the research with their discussion.

Many thanks to my friends, Mr. H. Fuji, Mr. G. Fujimoto, Ms. H. Kobara, Ms. M. Nakata, Ms. H. Okawachi, Ms. K. Shiraishi and my senior, Mr. H. Takahashi, Mr. Y. Ikagawa for their unfailing friendship and encouragement.

Finally, but the mostly I wish to express my deepest gratitude to my parents. Akira and Kinuyo, and my brother Sintaro, for their support and encouragements of continuing my work. I could not continue and finish this work without their understanding and supports. I would like to dedicate this thesis to my father.

Bibliography

- [1] C.Amsler *et al.* Phys.Lett.**B667**, (2008)37
- [2] D.J.Gross, F.Wilczek, Phys.Rev.**B8**, 3633 (1973)
- [3] H.L.Lai *et al.* (CTEQ Collaboration), Eur.Phys.J.**C12**, 375 (2000)
- [4] M.G. Albrow *et al.* (CHLM Collaboration) Nucle. Phys. **B56**, 333 (1973)
- [5] B.Alper *et al.* (British-Scandinavian Collaboration) Nucle. Phys. **B87**, 19 (1975)
- [6] B.Alper *et al.* (British-Scandinavian Collaboration) Nucle. Phys. **B100**, 237 (1975)
- [7] K.Guettler *et al.* (British-Scandinavian-MIT Collaboration) Nucle. Phys. **B116**, 77 (1976)
- [8] D.Antreasyan *et al.*, Phys.Rev. **D19**, 764 (1979)
- [9] D.E.Jaffe *et al.* (FNAL-E605 Collaboration) Phys.Rev.**D40**, 2777 (1989)
- [10] J.Adams *et al.* (STAR Collaboration), Phys.Lett. **B637**, 161 (2006)
- [11] B.Abelev *et al.* (STAR Collaboration), Phys.Rev. **C79**, 034909 (2009)
- [12] B.Abelev *et al.* (STAR Collaboration), Phys.Rev. **C75**, 064901 (2007)
- [13] B.Abelev *et al.* (STAR Collaboration), Phys.Rev. Lett. **97**, 132301 (2006)
- [14] B.Abelev *et al.* (STAR Collaboration), Phys.Lett. **B616**, 8 (2005)
- [15] D.Acosta *et al.* (CDF Collaboration) Phys.Rev.**D72**, 052001 (2005)
- [16] J.Schaffner-Bielich *et al.* nucl-th/0202054 (2002)
- [17] D.Buskulic *et al.* (ALEPH Collaboration), Z.Phys.**C73**, 409 (1997)

- [18] R.Barate *et al.* (ALEPH Collaboration), Phys.Rept, **249**, 1 (1998)
- [19] G.Alexander *et al.* (OPAL Collaboration), Z.Phys.C**72**, 191 (1996)
- [20] K.Ackerstaff *et al.* (OPAL Collaboration), Z.Phys.C**75**, 193 (1997)
- [21] G.Abbiendi *et al.* (OPAL Collaboration), Eur.Phys.J.C**16**, 185 (2000)
[hep-ex/0002012]
- [22] G.Abbiendi *et al.* (OPAL Collaboration), Eur.Phys.J.C**27**, 467 (2003)
[hep-ex/0209048]
- [23] P.Abreu *et al.* (DELPHI Collaboration), Eur.Phys.J.C**6**, 19 (1999)
- [24] B.Adeva *et al.* (L3 Collaboration), Phys.Lett.B**259**, 199 (1991)
- [25] D.Bender *et al.*, Phys.Rev.D**31**, 1 (1985)
- [26] A.Petersen *et al.*, Phys.Rev.D**37**, 1 (1988)
- [27] G.S.Abrams *et al.*, Phys.Rev.Lett.**64**, 1334 (1990)
- [28] H.Aihara *et al.* (TPC/Two Gamma Collaboration), Phys.Rev.Lett.**61**,
1263 (1988)
- [29] R.Brandelik *et al.* (TASSO Collaboration), Phys.Lett.B**114**, 65 (1982)
- [30] W.Braunschweig *et al.* (TASSO Collaboration), Z.Phys.C**47**, 187 (1990)
- [31] Y.K.Li *et al.* (AMY Collaboration), Phys.Rev.D**41**, 2675 (1990)
- [32] Y.Hatta and T.Ikeda, Phys.Rev.D**67**, 014028(2003)
- [33] A.Andronic,P.Braun-Munzinger,J.Stachel. Nucl.Phys.A**722**, 167-
199(2006)
- [34] K.Rajagopal, Nucl.Phys.A**661**, 150 (1999)
- [35] F. Karsch, J. Phys. G**31**, S633 (2005), hep-lat/0412038.
- [36] A. Adare *et al.* (PHENIX Collaboration), Phys. Rev. Lett. **101**, 232301
(2008)
- [37] S.S.Adler *et al.* (PHENIX Collaboration), Phys. Rev. Lett. **91**, 072301
(2003)
- [38] S.S.Adler *et al.* (PHENIX Collaboration), Phys. Rev. C **69**, 034910
(2004)

- [39] K.Adcox *et al.* (PHENIX Collaboration), Phys. Rev. Lett. **88** 022301 (2001)
- [40] A.Adare *et al.* (PHENIX Collaboration), Phys. Rev. **C82**, 011902(R) (2010)
- [41] A.Adare *et al.* (PHENIX Collaboration), Phys. Rev. C **84** 044902 (2011)
- [42] A.Adare *et al.* (PHENIX Collaboration), Phys. Rev. **C83**, 024909 (2011)
- [43] A.Adare *et al.* (PHENIX Collaboration), Phys. Rev. Lett. **98**, 232301 (2007)
- [44] J. W. Cronin *et al.*, Phys. Rev. **D11**, 3105 (1975)
- [45] D.Kharzeev and K.Tuchin, Nucl. Phys. **A770**, 40 (2006)
- [46] J.L.Nagle *et al.*, Phys.Rev. **C84**, 044911 (2011)
- [47] K.Hagiwara, *et al.* Review of Particle Physics. *Phys.Rev.D*, 66:010001, 2002.
- [48] K.Nakamura *et al.* *The Review of Particle Physics* J.Phys.**G37**,075021(2010)
- [49] Y.Nambu and G.Jona-Lasinio, Phys. Rev. **122**, 345 (1961)
- [50] Y.Nambu and G.Jona-Lasinio, Phys. Rev. **124**, 246 (1961)
- [51] K.Yagi, T.Hatsuda and Y.Miake, "Quark-Gluon-Plasma: From Big Bang to Little Bang", Cambridge, Univ. Pr. (2005)
- [52] W.Weise, Nucl. Phys. **A553**, 59c-72c (1993)
- [53] A.Baldis *et al.* (NA51 Collaboration), Phys.Lett.**B322**,244(1994)
- [54] E.A.Hawker *et al.* (FNAL E866/NuSea Collaboration), Phys.Rev.Lett.**80**,3715(1998)
- [55] H.Fukaya, *et al.* Phys.Rev.Lett.**98**, 172001(2007)
- [56] P.M.Stevenson, Phys.Rev.**D23**,2916 (1981)
- [57] T.Hatsuda and S.H.Lee, Phys.Rev.**C46** R34 (1992)
- [58] G. Agakichiev *et al.*, Eur. Phys. J. C **4**, 231 (1998)

- [59] J. P. Wessels *et al.*, Nucl. Phys. A**715**, 262 (2003)
- [60] R. Araldi *et al.* (NA60 Collaboration), Phys.Rev.Lett. **96**, 162302 (2006)
- [61] M. Naruki *et al.* (KEK-PS E325 Collaboration), Phys. Rev. Lett **96**, 092301 (2006)
- [62] R. Muto *et al.* (KEK-PS E325 Collaboration), Phys. Rev. Lett **98**, 042501 (2007)
- [63] F. Sakuma *et al.* (KEK-PS E325 Collaboration), Phys. Rev. Lett **98**, 152302 (2007)
- [64] K. Ozawa *et al.* (KEK-PS E325 Collaboration), Phys. Rev. Lett **86**, 5019 (2001)
- [65] M.H. Wood *et al.* (CLAS Collaboration), Phys. Rev. C **78**, 015201 (2008)
- [66] M. Nanova *et al.* (CBELSA/TAPS Collaboration), Eur. Phys. J. A**47**, 16 (2011)
- [67] Brown, G.E and M. Rho, Phys.Rep.**363**,85(2002)
- [68] Rapp, R. and J. Wambach, Adv.Nucl.Phys.**25**,1(2000)
- [69] Nuclear Instruments and Methods A **499**(2003) 235-244
- [70] M. Harrison, *et al.* Annu.Rev.Nucl.Part.Sci. **52**(2002) 425-469
- [71] Nuclear Instruments and Methods A **499**(2003) 423-432
- [72] Nuclear Instruments and Methods A **499**(2003) 549-559
- [73] T. Nakamura
<http://www.phenix.bnl.gov/WWW/run/03/focus/talks/bbc/focus/bbc.ppt>
- [74] Nuclear Instruments and Methods A **499**(2003) 433-436
- [75] Nuclear Instruments and Methods A **499**(2003) 480-488
- [76] K. Adcox *et al.* Nucl. Instr. and Meth., **A497**, 263 (2003)
- [77] K. Adcox *et al.* (PHENIX Collaboration), Nuclear Instruments and Methods **A499**, 489 (2003)
- [78] J.T. Mitchell *et al.* Nuclear Instruments and Methods **A482**, 491 (2002)

- [79] A.Chikanian *et al.* Nuclear Instruments and Methods **A371**, 480 (1996)
- [80] M. Ohlsson *et al.*, Comp. Phys. Commun. **71**, 77 (1992)
- [81] S.S.Adler *et al.* (PHENIX Collaboration), Phys.Rev.C**69**, 034910 (2004)
- [82] Nuclear Instruments and Methods A **499**(2003) 508-520
- [83] Nuclear Instruments and Methods A **433**(1999) 143-148
- [84] Nuclear Instruments and Methods A **499**(2003) 521-536
- [85] Nuclear Instruments and Methods A **499**(2003) 537-548
- [86] Nuclear Instruments and Methods A **499**(2003) 560-592
- [87] Nuclear Instruments and Methods A **499**(2003) 593-602
- [88] website of the PHENIX experiment:
<http://www.phenix.bnl.gov/WWW/run/drawing/>
- [89] A.Adare *et al.* (PHENIX Collaboration), Phys. Rev. C**81**, 034911 (2010)
- [90] T.A.Armstrong, *et al.* (E760 Collaboration) Phys.Rev.D **54**(1996) 7067-7070
- [91] A.Spiridonov hep-ex/ **0510076**
- [92] S.S.Adler *et al.* (PHENIX Collaboration), Phys.Rev.Lett.**91**, 241803, (2003).
- [93] S.S.Adler *et al.* (PHENIX Collaboration), Phys.Rev.C**104**, 051902(R), (2007).
- [94] A.Adare *et al.* (PHENIX Collaboration), Phys. Rev. D**83**, 052004 (2011)
- [95] S.S.Adler *et al.* (PHENIX Collaboration), Phys.Rev.C**74**, 024904, (2006).
- [96] A.Adare *et al.* (PHENIX Collaboration), Phys.Rev.Lett., **104**, 132301, (2010).
- [97] J.Adams *et al.* (STAR Collaboration) Phys.Lett.B**612**, 181, (2005).
- [98] C.Tsallis, J.Stat.Phys**52**, 479, (1988).
- [99] G.Wilk and Z.Wlodarczyk, Phys.Rev.Lett.**84**, 2770-2773, (2000).

- [100] B.Alper *et al.* Nucl.Phys.**B87**, 19, (1975).
- [101] J.Schaffner-Bielich *et al.* nucl-th.**020254** (2002).
- [102] S.S.Adler *et al.* (PHENIX Collaboration) Phys.Rev.**D76**, 051106, (2007).
- [103] S.S.Adler *et al.* (PHENIX Collaboration) Phys.Rev.**C75**, 024909, (2007).
- [104] A.Adare *et al.* (PHENIX Collaboration) Phys.Rev.Lett.**98**, 232002, (2007).
- [105] A.Adare *et al.* (PHENIX Collaboration) Phys.Rev.**D82**, 012001, (2010).
- [106] A.Adare *et al.* (PHENIX Collaboration) Phys.Rev.**C83**, 064903, (2011).
- [107] C.Tsallis, J.Stat.Phys.**52**,479(1998)
- [108] T.Sjostrand and M.v.Zijl, Phys.Rev. **D36**, 2019 (1987)
- [109] B.Andersson *et al.* Phys. Rept. **97**, 31-145 (1983)
- [110] T.Sjostrand, Nucl.Phys.**B248**, 469 (1984)
- [111] R.Hagedorn, Riv. Nuovo Cimento Soc. Ital. Fis. **6N10**, 1 (1983)
- [112] G.Arnison *et al.* Phy.lett.**B118**, 167 (1982)
- [113] M.Biyajima *et al.* (UA1 Collaboration) Eur.Phys. J. **C48**, 597 (2006)

公表論文

- (1) Measurement of neutral mesons in $p+p$ collisions at $\sqrt{s} = 200\text{GeV}$ and scaling properties of hadron production
A.Adare, K.M.Kijima *et al.*, (別紙、共著者リスト 1 参照)
Physical Review C83, 052004 (2011).

Letter of Acceptance

This letter is to state that Mr. Kotaro M. Kijima has my approval to preferentially apply the following article as part of his doctoral dissertation at Hiroshima University.

Article: PHYSICAL REVIEW D 83, 052004 (2011)

Title: Measurement of neutral mesons in p + p collisions at $\sqrt{s} = 200$ GeV and scaling properties of hadron production

Spokesperson of the PHENIX Collaboration:

Barbara V. Jacak

Professor of Physics and Astronomy at SUNY Stony Brook University

Date: January 10, 2012

Signature:

A handwritten signature in black ink, appearing to read "Barbara V. Jacak", written in a cursive style.

参考論文

- (1) Nuclear modification factors of ϕ mesons in $d+Au$, $Cu+Cu$ and $Au+Au$ collisions at $\sqrt{s_{NN}} = 200\text{GeV}$
A.Adare, K.M.Kijima *et al.*, (別紙、共著者リスト 2 参照)
Physical Review C83, 024909 (2011).
- (2) Identified charged hadron production in $p+p$ collisions at $\sqrt{s} = 200$ and 62.4GeV
A.Adare, K.M.Kijima *et al.*, (別紙、共著者リスト 3 参照)
Physical Review C83, 064903 (2011).